

AD-A179 673

ACTA AERONAUTICA ET ASTRONAUTICA SINICA(U) FOREIGN  
TECHNOLOGY DIV WRIGHT-PATTERSON AFB OH 07 APR 87

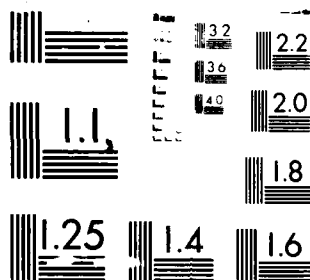
1/3

UNCLASSIFIED

FTD-ID(RS)T-1246-85

F/G 13/8

NL



MICROCOPY RESOLUTION TEST CHART  
NATIONAL BUREAU OF STANDARDS-1963-A

DTIC FILE COPY

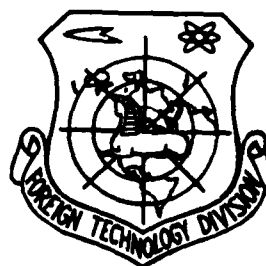
FTD-ID(RS)T-1246-85

AD-A179 673

FOREIGN TECHNOLOGY DIVISION



ACTA AERONAUTICA ET ASTRONAUTICA SINICA



APR 28 1987

Approved for public release;  
Distribution unlimited.



4 28 115

## HUMAN TRANSLATION

FTD-ID(RS)T-1246-85

7 April 1987

MICROFICHE NR: FTD-87-C-000275

ACTA AERONAUTICA ET ASTRONAUTICA SINICA

English pages: 224

Source: Hang Kong Xuebao, Vol. 6, Nr. 3, 1985,  
pp. 201-300

Country of origin: China

Translated by: SCITRAN

F33657-84-D-0165

Requester: FTD/TQTA

Approved for public release; Distribution unlimited.

THIS TRANSLATION IS A RENDITION OF THE ORIGINAL FOREIGN TEXT WITHOUT ANY ANALYTICAL OR EDITORIAL COMMENT. STATEMENTS OR THEORIES ADVOCATED OR IMPLIED ARE THOSE OF THE SOURCE AND DO NOT NECESSARILY REFLECT THE POSITION OR OPINION OF THE FOREIGN TECHNOLOGY DIVISION.

PREPARED BY:

TRANSLATION DIVISION  
FOREIGN TECHNOLOGY DIVISION  
WPAFB, OHIO



AI

## TABLE OF CONTENTS

Graphics Disclaimer .....	iii
The Current Situation and Prospects of Cast Turbine Blades, by Yung Ke .....	1
Mechanisms of Fatigue-Crack Propagation and Their Engineering Application to Some Structural Materials, by Yan Minggao .....	20
The Approaches to the Development of Composite Materials for Aeronautical Industry in China, by Fan Tang .....	60
Investigation on Temper Brittleness of Granular Bainite in 15CrMoVA Steel, by Liu Zhengtang, Kang Mokuang, and Yang Zheng .....	81
Directionally Solidified Blade Superalloy DZ-22, by Wang Luobao, Chen Rongzhang, Wang Yuping .....	95
Plastic Deformation Anisotropy of LC4-Aluminum-Alloy Plates, by Li Huanxi and Chen Changqi .....	112
Relationship Between Shot Peening Surface Strain Layer and Fatigue Strength of High-Strength Aluminum Alloys, by WANG Renzhi LI Xiangbin .....	129
Distribution and Effect of Silicon in Al-Si Coatings, by CAI Yulin, ZHENG Yunrong, MO Longsheng, and YANG Zhonglin .....	143
Correlation Between Interface Reaction and Properties of Carbon and Graphite Fiber Reinforced Aluminum Composites, by ZHAO Chang cheng .....	159
Precipitation Characteristics of Metastable Phase in Titanium Alloy TB2, by YAO Jin sheng and WANG Shi hong .....	172
Effect of Refining Elements on Dendrite Arm Spacing of Al-5.0Cu-0.8 Mn Alloys, by CHU Yanhe and XU Cailu .....	184
An Investigation of Ion Implantation in Copper Alloys for Improving Their Wear Resistance, by WANG Yi hua, WEN Meng quan, WANG Zheng xiang, and JIANG Ji feng .....	194

Fabrication of Boron/Aluminum Shapes, by YU Kun, XU Hong qing, SUN Chang yi, YAO Zhi ping, and DAI Nan rong .....	207
An Approximate Analysis of Net Section Normal Stress in a Laminate Strip with a Circular Hole, by ZHAO Jian hua and LIU Run tong .....	216

GRAPHICS DISCLAIMER

All figures, graphics, tables, equations, etc. merged into this translation were extracted from the best quality copy available.

# THE CURRENT SITUATION AND PROSPECTS OF CAST TURBINE BLADES

Yung Ke

(Chinese Aeronautic Establishment)

## ABSTRACT

This paper reviews the current situation and the history of development of cast turbine blades of Chinese aircraft engines for nearly three decades since 1956. and sums up the cast high-temperature alloys and casting methods which were provided by the materials and casting scientific and technical personnel during this period which have met the demands of aircraft engines.

Remarkable successes have been made in many fields such as cast rotor blades, ceramic cores for hollow blades, research into dispersion-strengthened alloys, and computer-based quality control, etc.

With a view to future development of high performance engines this paper proposes research on ceramic and refractory materials to meet the following requirement:

1. increased operating temperatures;
2. enhanced surface stability;
3. superior mechanical properties.

---

This paper was received August 20, 1984.



However, in addition to developing the above-mentioned materials, it must be kept in mind that high-temperature alloys will still be used in engine structural components operating at 550 to 1100°C, for the foreseeable future.

Therefore, generalized computer applications must be studied. Improvement in refractory metal molds and vacuum die cast blade processes, will improve blade quality control and will replace the traditional investment casting processes.

## INTRODUCTION

One of the key problems in designing and manufacturing new generation aircraft engines with high thrust to weight ratio is the requirement to develop turbine blade materials which can work at turbine inlet temperature of up to 1800 ~ 2100 K and under complicated stress conditions. In order to achieve this goal, we must consider the situation of the research and production of China and organize well to solve the key technical problems step by step.

## THE CURRENT SITUATION

In this section we first review the history and the current situation of the development of cast turbine blades for aircraft engines in China. In the past more than thirty

years, the aeronautic industry of China has gone from imitation to independent research and development. In order to meet the technical requirements of new aircraft, research in the area of aviation materials and processes are also catching up with the advanced world levels. Since the 60s, the Chinese Academy of Science, the Ministry of Metallurgical Industry, and the Ministry of Aeronautic Industry have cooperated to solve problems in casting high-temperature alloy turbine blades. A whole series of work has been developed and many difficult problems have been solved. This work has caused the attitude of engine designers toward the quality of cast blades to go from doubt to wait-and-see and finally to having trust in the use of several types of blades. Today many agree with applying the cast high-temperature alloy blades in several types of engines, and the testing operations were successful. This is a very long period of development. As a brief summary, the major results in this period are as follows.

1. Imitated and developed more than 10 types of Ni-base high-temperature alloys, which were consistent with the production and resources of China, and met the requirements on the physical and mechanical properties by hot components of the aircraft under development, to supply the Chinese aeronautic industry to manufacture new types of aircraft. According to the properties, applications, and order of

research and development, Ni-base alloys (including some Ni-Fe-base high-temperature alloys) were standardized as K1-K24 material series. Rather detailed investigation have already been done on the structure and properties of these alloys. Furthermore, the components made by using these alloys were tested in the use of aircraft products for long time periods. Currently, turbine blades and guiding blades, made by using Ni-base high-temperature alloys (including cast and deformable alloys) can work stably and continuously at 1173 ~ 1223 K for a long period.

2. In order to meet the requirement of increasing the temperature  $T_3^*$  before the turbine, based on the use of Ni-base high-temperature alloys, we have designed and manufactured casting hollow turbine blades with enforced air cooling. Therefore, the working temperature of some types of engine was increased from 1180 K to 1288 K. The air flux of cooling is 1.5 ~ 2.0% of the total air flux of the engine. After many times of improvement by measures of design and processing, the temperature after enforced cooling was reduced stably down to 100 ~ 150 K. Therefore, the thrust of the engines was obviously increased. After more than ten years of real testing of production and flying, the components are reliable and stable either in the aspect of design, or in processing and materials, etc. It is especially worth pointing out that the success of

investment processing method of hollow blades has played a key role in the application of the hollow channel blades.

3. In order to meet the requirements of new types of aircraft, the Ni-base high temperature alloys which can work at higher levels of working temperature have been investigated in the following five aspects, hoping to find out an optimized method for increasing the working temperature of turbine blades to the level of 1273 ~ 1373 K.

(1) Use the principle of the dispersion strengthening of metals to develop oxide-strengthened deformative Ni-base high-temperature alloys (ODS). The United States has developed Ni-base high-temperature alloys MA956, MA754, and MA6000, which are dispersively strengthened with rare earth metal oxides. These alloys still have higher strength at 1473 K or lower ( $\sigma_b=84\text{MPa}$ ). They also have good oxidation resistance and anti-carbon-diffusion properties [1]. By considering this fact, if we can develop dispersion-strengthened high-temperature cast alloys, because it can be directly casted into the designed shape, the shortage of the difficulties met in the deformative process can be overcome. Therefore it will help the further development and applications of this type of material.

(2) Develop Ni-base high-temperature alloys strengthened by high concentrations of high-melting-temperature metals, such as casting alloy K19 which has 10%

W and 2% Mo.

(3) Develop single crystalline turbine blades to increase the working temperature to 1403 ~ 1423 K.

The above new turbine blade materials and their process methods are not yet used in the production of any type of engine. Furthermore, some technical problems also need to be solved. But these research results will play important roles in future development and production of new types of engines.

(4) Some progress was obtained in materials for precise casting. In order to meet the requirements of the future precise casting of hollow blades with complicated surfaces, we investigated the key problems of increasing the working temperature of ceramic cores, keeping the stability of the core and preventing high-temperature deformation, etc. Some experience was accumulated and technical preparation was made for use of the ceramic core in production.

(5) We have begun to use computers to study the crystallization process and guide the production of cast components. Some results have already been obtained. For example, starting from solving the thermal equilibrium equations of the cooling process of solidification of cast components, we can determine an optimized method of placing cold iron pieces and ventilation outlets for achieving ordered crystallization. Therefore the quality of the cast

components was improved [2]. Besides, starting from exploring the optimized processing parameters for the control of the directional crystalization, we can use the correct cooling conditions to obtain the best structure and properties of cast components. Recently, the directional crystalization method has been used in the production of turbine blades of different sizes; and these blades are planned to be installed in engines for testing operation and testing flying. Because of this measure, the concept of increasing the working temperature for 50 ~ 100 K is becoming a reality gradually.

#### THE PROSPECTS OF FUTURE DEVELOPMENT

(203)

After many years of development, we have made more progress in the materials for turbine blades and their processing methods. But we still have a big gap with the world advanced levels and still can not meet the requirements for further development and production of aircraft engines. For example, the working temperature before turbine (the temperature  $T_3^*$ ) of the British Spey engines has reached 1440 K, and the working temperature before turbine of our own engines has also reached 1410 K. With such requirements for engine design, in the situation that the working temperature of turbine blade materials

reaches 1173 ~ 1223 K, an adequate cooling technology must be developed to reduce surface temperature of blades by 200 ~ 250 K. Then the air flux used for this cooling is about 4% of the total air flux. Besides, the United States is developing the CFM56 jet engine which has a working temperature ( $T_3^*$ ) of 1780 K before turbine. Under this situation, even if advanced single crystalline Ni-base high-temperature alloys are used, it is still necessary to reduce the surface temperature by 300 ~ 350 K. But as we have mentioned above, the current cooling technology can only reduce the surface temperature by about 100 K. Obviously it requires further cooperation, between the personnel of engine design, material research, and processing research, to develop better methods for achieving the temperature reduction of 300 ~ 350 K.

According to the above situation, we know that the material for the turbine blades is still one of the key problems in developing high thrust to weight ratio aircraft engines. In the author's opinion, solving the following problems might open a new stage for the research and development of new type engines in China.

1. Investigate the possibility of changing fuel types of engines.

The most-high temperature alloys used in aircraft engines are Ni-, Co-, and Fe-base alloys. The melting

temperature of these materials is about 1800 K and the maximum working temperature is possible about 1500 K. Even with the most advanced cooling technology in the United States for reducing the surface temperature of the blades, the maximum reduction of the temperature achievable is about 350 ~ 400 K. That is: the maximum temperature before the turbine can only be 1800 ~ 1900 K. Obviously, further developing high-thrust-weight-ratio aircraft engines will be limited, and the technical requirements can not be met. In order to break through this limitation, the body materials of turbine blades should be changed. Nb- or Mo-base alloys which have higher heat resistance can be used to replace the high temperature alloys with transition metals Fe, Ni, or Co as base materials. The melting temperatures of Nb and Mo are all above 2500 K, they have large potential for being used above 1800 K. At 1800 K, the mechanical properties of Nb and Mo are obviously better than Ni-, Co-, and Fe-base alloys. But the problem is that in the temperature region of 773 ~ 973 K these two metals will react with oxygen to form evaporative oxides ( $\text{Nb}_2\text{O}_5$ ,  $\text{MoO}_3$ , etc.), therefore losing their protective functions and even disappearing themselves totally. The research of the surface protective layers of Nb and Mo has not yet greatly progressed abroad. Obviously, such evaporative oxides can be formed only in an oxygen environment. If we can change the fuel composition to



avoid the hydrocarbon which forms in an oxidation environment and widely use liquid hydrogen fuel to form a reductive environment, then turbine blades made with the high melting temperature metals Nb and Mo will not be oxidized and evaporated in this reactive environment and can still keep the good mechanical properties <sup>(at 1500-1900K.)</sup>. Obviously, this is an attractive project. Currently, China has already built several production plants of Nb and Mo and also has abundant mineral resources. China also has a certain experience in the research, development, and production of Nb and Mo. There are also foreign research reports about the fabrication of testing blades of high-melting-temperature metals. It is worthwhile for us to develop these high melting temperature super alloys for making turbine blades.

During the "energy crisis" several years ago, in order to save aircraft fuel, the United States had considered to use methane or hydrogen as aircraft fuels [3]. With the support by NACA, Boeing, Lockheed, Pratt-Whitney, etc., are developing metal hydrogen for a replacement of petroleum fuels. Besides, West Germany, the United States, Japan, and Australia are developing metal hydrides to replace petroleum fuels [4], and the testing results in inner combustion engines were very good and it has already been used in the prototype models of spacecraft. In order to meet the needs of development, using liquid and even metal hydrides

as aircraft fuels is adequate from both the technical and economical viewpoints.

(204

China has special favorable conditions for the development of high temperature super alloys. The deposit of W and Mo is among the largest in the world. For many years W-base alloys were used in military products and electrical products as high specific weight and high plastic materials [5]. All the experience can be borrowed.

Even before the problem of changing the aircraft fuels is solved, the high-melting-temperature metals will be useful. We can use the special high-temperature properties to strengthen Ni- and Co-base high-temperature alloys. For example, we can develop composite materials in which high-melting-temperature metal fibers are used to strengthen the base alloys. The United States and Canada have developed a W-fiber-strengthened high-temperature composite material which use 40% volume of 0.5 mm-diameter W fibers fabricated by a high-temperature-alloy powder-melting method. On the surfaces of W fibers, a 3 ~ 4  $\mu\text{m}$  hafnium nitride is covered on the surface of the W fibers to prevent recrystallization caused by the penetration of Ni into W. The powder of the base material MAR-M200 with a particle size of 140 grade is produced by a Ar-fog method. The powder is sintered under a constant pressure for shape formation. The two-hour strength at 1323 K of this material can reach 103 MPa [6].

2. Develop ceramic material to replace Ni- and Co-base high-temperature alloys.

Ceramic materials were the earliest materials mankind ever used. China was famous for its ceramic production and was in the leading position for several thousand years, and had exported a large quantity of ceramic products to foreign countries all over the world. Ceramic had become a symbol of China. The traditional ceramic materials have a very high temperature resistance and heat stability but are too fragile. Therefore it is difficult to use them for structural materials. Recently, the United States has used ceramic materials to cover Ni-base alloys as a material for artificial teeth and this technology was introduced in Peking Air Force General Hospital. Based on this concept, we can experiment making turbine blade bodies and tenon teeth with high-melting-temperature metals, such as Nb, Mo, etc., or alloys. The whole blades can be welded by electronic-beam welding and be covered with a ceramic protective layer. Thus it is possible to obtain turbine blades with a working temperature as high as about 1900 K. We have already begun to investigate the composition of the base metal materials and ceramic materials, plating processing, quality testing, etc. This is a meaningful project.

Recently, the research is not only limited in ceramic surface protective layers, and some foreign countries are

already investigating all-ceramic blades. TRW company of the United States in California has fabricated turbine blades with silicon nitride. There were no abnormal effects after 500 hours of testing operation. It is necessary to make structural changes of air compressors and turbine rotors; that is: the vibration frequencies need to be adjusted for reducing the vibration, therefore preventing the cracking of the fragile ceramic materials. In 1982, Japan used fully mixed silicon nitride and polystyrene powder to make blade bodies under a 250 ton die casting machine. Then the blade bodies were baked and the plastic powder was burned and evaporated, leaving many small holes in the blade bodies. Metal powder was then penetrated into these holes under heat and constant pressure and thus the blades were turned into metal-ceramic ones which had lower fragility. The details of the processing method of silicon-nitride metal-ceramic turbine blades need further exploration.

The United States has developed  $\alpha$ -SiC which has good strength and durability at 1473 ~ 1573 K [7]. The polycrystalline TiC, which is melted under a  $10^{-1}$  torr vacuum or 35 KPa Ar-atmosphere and is put under a 34 ~ 59 MPa heat constant pressure at 1973 ~ 2020 K for 0.5 ~ 1 hour, has a crystalline diameter of 25  $\mu\text{m}$ , and at the grain boundary the concentrations of the impurities such as Fe,

Co, and Si, were depressed obviously. Thus the high temperature properties were improved and the transition temperature was also decreased to 1800 K [8].

Recently, Japan and Britain are cooperating to make fiber-strengthened aluminium blades. In 1980, cooperating with Dow Corning Company of the United States, Japan made a ceramic composite material which uses silicon carbide fibers as strengthening body and can be used at 1473 K or above. This material was already used for the testing at the AGT (Automotive Gas Turbine)-100 turbine engine made by Pratt & Whitney company [9]. According to the plan of applying ceramic materials in turbine engines (CATE), the Allison Engine Division of Detroit Engines, of General Motor Company Company is investigating the optimized processing parameters of turbine blades [10]. This company is making systematic experimental studies on problems of design, manufacture, testing, ect.

The main advantages of using ceramic turbine blades in AGT-100 engine testing are [11]:

(1) The equipment cost for ceramic blades is much lower than the equipment cost for metal blades. Therefore the cost of the blades can be greatly reduced.

(2) After Working at above 1700 K for more than 3500 hours the ceramic blades still can meet the requirements by aerodynamics. It is far superior than all other materials.

(205

(3) The shape can be formed arbitrarily; therefore the outside shapes can meet the requirements by aerodynamics even better. This can not be matched by other materials.

Therefore ceramic materials will be the new turbine blade materials to be used.

3. Improve the traditional investment casting method of making turbine blades.

Using of Mo-base alloy mold to replace the traditional investment precise casting is a direction of development. Because investment casting method is complicated, and it consumes costly mould and shaping materials, and also wastes a large quantity of energy; therefore this traditional method for making turbine blades will be improved sooner or later. Manufacturing turbine blades in vacuum by using metal mold has obvious advantages. With the help of the Ministry of Metallurgy Industry, we have made Mo-base alloy molds. The model rod made by using Mo-base alloy mold in vacuum has the same surface smoothness as the investment casting method. If metal penetration and surface protective layer are applied to these Mo-base alloy molds, it is possible to use this method in manufacturing of directional solidification and single crystalline blades.

Fast solidification is also a direction of development. In the manufacture of Ni-Al-Mo series high temperature blades. Fine crystalline structure was obtained by liquid-

nitrogen fast-cooling technique (RST); thus the working temperature was increased by 150 K. Fast solidification can also improve the plasticity of fragile metal-ceramic materials. Taub [12] had investigated the strength and plasticity of boron-added Ni<sub>3</sub>Al and founded that when the speed of solidification was increased, the crystalline size of Ni<sub>3</sub>Al with 0.5 ~ 1.0% boron was reduced and the plasticity at room temperature ( $\epsilon_f$ ) was increased from 0 to 10%. If the cooling speed can be further increased to obtain a non-crystalline structure, the properties can be further improved. The yielding strength of metal glass Fe<sub>80</sub>B<sub>20</sub> can reach 3600 MPa, whereas the maximum strength of high-strength steel is below 2800 MPa [13]. Metal glass might also be used in strengthened fiber composite materials.

Vacuum ferrous-metal die casting technology is also a processing technology for shaping of turbine blades. In vacuum and under a high pressure, same precision as in vacuum metal mold casting technology can be obtained; at the same time the impurity and compactness are depressed. Vacuum pressure casting also can reduce the consumption of energy and materials; therefore the production cost can be cut down for several times. Although China has just begun to investigate vacuum die casting, the many-year experiences of ferrous metal casting under normal pressure will offer assistance. Vacuum die casting will play an important role

in replacing the traditional investment casting technology.

Heat constant-pressure technology has positive results in powder metallurgy products. Recently, aluminium alloy casting components were put in an 0.103 MPa pressure and in inert gas environment for two hours at 738 K. The compactness of the casting components was increased obviously and the pulling resistance at room temperature and the anti-fatigue property were improved [14]. The application of the heat constant-pressure technology in high temperature casting alloys will have good results.

#### 4. Use computer technology more widely.

Starting from the individual areas of quality control of cast components and selection of processing parameters by the calculations of thermal equilibrium in solidification process, gradually develop more completed mathematical models to achieve real-time control of processing parameters and automatic quality testing of casting products, etc., which are technologies based on the overall applications of computers, to improve the situation of turbine blade production [15].

## CONCLUSIONS



Facing the project of the development of high-thrust-weight-ratio and high efficiency aircraft engines, we must offer correspondent new materials and new processing methods to support the smooth production of new aeronautic products. Based on the success achieved before, we should summarize the former experience of successes and failures. Starting from the continuous improvement of the current Ni-based high temperature alloys, we should gradually develop metal-ceramic and ceramic materials. We should also gradually introduce processing methods for making high precision hollow blades, and introduce and improve new processing methods such as directional crystalization, single crystalline, fast solidification, metal mold, vacuum pressure casting, etc. With the close cooperation between technical personnel of aircraft engines, metallurgy, material, characterization of mechanical properties and non-destructive testing, the turbine blades will be developed more quickly. (206

#### REFERENCES

- [1] Sadananda, K. and Shahinian, P., Met. Trans. A, V.15A, March (1984), pp. 527-539.
- [2] Yi Chiuping, Zhou Shiaohe, Chinese J. of Aeronautics, Vol. 5, No.3, (1984).
- [3] NACA-CP-1146.

- [4] Bradhurst, D. H., Metal Forum, Vol.6, No.3, (1983), pp. 139-148.
- [5] Woodward, R. L., Yellup, J. M., and deMorton, M. E., Metal Forum, Vol.6, No.3, (1983), pp. 175-179.
- [6] Kandeil, A. Y., Immarigeon, J-P. A. , Wallace, W. and deMalherbe, M. C., Met. Trans. A. Vol. 15A, March (1984), pp. 501-510.
- [7] Govila, R. K., J. Mater. Sci., Vol. 18, (1983), pp. 1967-1976.
- [8] Katz, A. P., Lipsitt, H. A., Mah, T. and Mendiratta, M. G., J. Matter., Vol. 18, (1983), pp. 1983-1992.
- [9] Jane's Defence Weekly, (1982), 2.4, pp. 168.
- [10] Storm, R. S., and Lashway, R. W., AIAA-82-1211, (1982).
- [11] Byrd, J. A. and Helms, H. E., AIAA-82-1168, NASA CR-159865, (1982).
- [12] Taub, A. I., Huang, S. C. and Chang, K. M., Met. Trans. A, Vol. 15A, Feb. (1984), pp. 399-402.
- [13] Stewart, A. M., Metal Forum. Vol.6, No.2, (1983), pp. 122-131.
- [14] Rooy, E. L., Modern Casting, Dec. (1983), pp. 18-20.
- [15] Pehlke, R. D., Casting Engineering and Foundry World, Vol.15, No.1, Spring (1983), pp.42-52.

MECHANISMS OF FATIGUE-CRACK PROPAGATION AND THEIR  
ENGINEERING APPLICATION TO SOME STRUCTURAL MATERIALS

YAN MINGGAO

(Beijing Institute of Aeronautical Materials)

ABSTRACT

This paper reviews briefly the mechanisms of fatigue-crack propagation behavior and their applications to some aircraft Al-alloys, Ti-alloys, and high-strength steels. A general analytical expression for predicting threshold values of fatigue-crack propagation is proposed. The ability of each of four current retardation models for predicting fatigue lifetime and retardation effect of Ti-6Al-4V alloy under tensile overloading is evaluated. Some modifications of the Willenborg and Maarse models are made and their applications to the lifetime prediction of Al- and Ti-alloys are investigated. The modified Maarse model improves obviously the precision of the lifetime prediction under tensile overloading and spectrum loadings. The effects of microstructures, stress ratios, surface conditions and environment on fatigue-crack propagation behavior are also discussed in this paper.

-----

This paper was received Sep. 12, 1984.

## INTRODUCTION

The study on the microscopic morphology and mechanisms of fatigue crack propagation behaviors is a very actively investigated subject in the fields of material science and technology. Recently the design of aircraft structure has already been developed into the stages of safety lifetime and damage tolerance. It is required to obtain the characteristics of cracking, the criteria of evaluating the lifetimes of materials, and the models of mechanics. Although some mechanical behaviors, physical properties, and microscopic mechanisms about the processes of material fatigue cracking, under the conditions of applications, were known, further understanding the quantitative analysis of material fatigue cracking under the conditions of applications and its engineering applications are needed.

## THE CHARACTERISTICS OF FATIGUE-CRACK PROPAGATION AND THEIR MECHANISMS

### 1. Fractograph of fatigue crack under propagation.

Usually we consider that fatigue crack propagation undergoes three stages, and can be described approximately by using a S-like curve. In different stages, they have different mechanisms of fatigue cracking [1].

As a result of combined effects of different interior

structures and different exterior conditions (such as ways of loading, stress condition, and environment), the fractographs of fatigue cracks under propagation are usually different. Based on a large quantity of investigation on machine components and specimens, we can summarize eight fractographs and all these can be basically explained by the mechanism of "alternative shearing deformation" and "alternative tearing cracking" [2]. Recently by a careful observation and study of matched fractographs of fatigue specimens of Al, Cu, Ti, Fe-Ni and Ni alloys, it was found that the microscopic morphology of two matched fractographs are asymmetric and quite different (Fig. 1). The results have shown that the fatigue crack propagation in a machine component or a specimen is a process of uneven and alternatively shearing cracking. Fig. 2 is a schematic illustration of the mechanism of fatigue crack propagation [3].

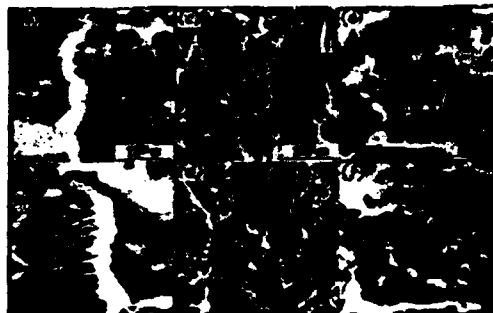


Fig. 1 Matched fractographs of fatigue specimens: (a), (b) LY12 Al alloys; (c), (d) GH36 Ni alloys; (e), (f) Ti-6Al-4V [3].

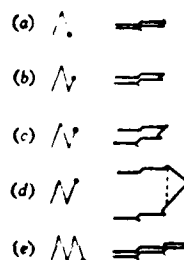
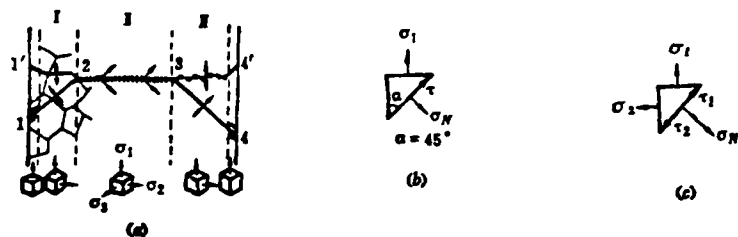


Fig. 2 Schematic illustration of mechanism of fatigue crack propagation [3].

Because of the combined influence of second phase, impurities, stress condition, and environment, etc., in the

real engineering materials, the macroscopic morphology of fatigue crack in engineering materials has many forms.

Fig. 3 schematically illustrates the macroscopic orientations of the fatigue-crack propagation and the status of the corresponding normal stresses when a specimen of metal is loaded in simple uniaxial circulating tension. If the specimen is made of a pure metal or a simple alloy, the orientation of the fatigue-crack propagation will be along the route 1-2-3-4, that is, the shearing-normal-shearing mode cracking. But when an engineering material contains second phase and impurities, the orientation of the third-stage fatigue-crack propagation will be along the route 3-4', that is, the shearing-normal-normal mode cracking. When the specimen exists in corrosive mediums, the orientation of the first-stage fatigue-crack propagation will be along the route 1'-2, that is, the all-normal mode cracking [2].



$$\sigma_v = \sigma_1 \sin^2 \alpha + \sigma_2 \cos^2 \alpha$$

$$\tau = 1/2 \sin 2\alpha (\sigma_1 - \sigma_2)$$

Fig. 3 Schematic diagram of mechanism of fatigue crack propagation:

(a) fracture features and stress state; (b) uniaxial tension; (c) biaxial tension [2].

2. Microscopic mechanisms of fatigue crack-propagation of the initial stage.

During the past twenty years, people have already experimented and done research about the fatigue-crack propagation of the second stage and understood much about it. The fatigue-crack propagation of the third stage is very fast, then it has little influence on the fatigue lifetime of a machine component. Therefore people began to pay more attention to the fatigue crack propagation of the first stage, which is more sensitive to structure stress ratio and environment. Some microscopic mechanisms and mechanics models have been proposed [4,5].

Hertzberg and Mills [6] observed many fractographs of Al, Cu, Ti, Ni-base alloys, and stainless steel, in their every stage of fatigue-crack propagation, and found that crystalline facets and river-like fractographs occur when fatigue-cracking speed is very low. Beevers [7] listed facet orientations of more than ten alloys and pointed out that these facets are usually close to close-packed crystalline facets, that is, {111} and {100} of F.C.C. and {110} and {100} of B.C.C. and {0001} of close-packed hexagonal metals. But he did not make any explanation for that the facets appear in both types of crystalline planes for cubic metals.

(210



Table 1 Facet orientation of some metal and alloys [2]

晶 格 (1)	合 金 (2)	SFE	滑移类型 (3)	小平方位向 (4)
FCC	Al合金 (5)	高 (6)	波状 (7)	{001}
	Ni合金 (8)	低 (9)	平面 (10)	{111}
	不锈钢 (11)	低 (12)	平面 (13)	{111}
BCC	Fe-3%Si (13)	高 (14)	波状 (15)	{001}
	β 黄铜 (16)	低 (17)	平面 (18)	{110} ± 10°
HCP	Ti合金 (19)	高 (20)	波状 (21)	{0001} ± 5°

1-crystal lattices; 2-alloys; 3-slip types; 4-facet orientation; 5-alloy; 6-high; 7-wave pattern; 8-alloy; 9-low; 10-plane; 11-stainless steel; 12-low; 13-plane; 14-high; 15-wave pattern; 16-brass; 17-low; 18-plane; 19-alloy; 20-high; 21-wave pattern.

From Table 1 we can know that for high slip-misfitting energy (SFE), and wave-like-slipped cubic metals, because of the intersected slipping, the cracking along the cubic surface is easy to happen. Cottrell [8] and Lynch [9] had some explanations for the {001} cracking in cubic metals. Besides, by analyzing the morphology of the broken cross sections and the stress status at the different stages of fatigue cracks of metals, we think that during the initial stage of crack propagation the stress is planar (see figure 4-c). Obviously, when the sample is pulled in opposite

directions, the shearing stresses in the slipping plane cancel each other whereas the normal stresses add each other. This helps to produce small plane cracking [2].

3. Predication of the threshold of fatigue-crack propagation.

Recently, a large quantity of literature on the study and measurement of the threshold values of crack propagation of structural materials have been done [1]. But until now most of the calculation and predication of the threshold values are experiential equations. The constants or coefficients in the equations are determined by some specially designed experiments. Therefore since the beginning of the 80's we began to explore general formulas to calculate the threshold values of metal fatigues [10].

According to the formulas of plasticity size of the crack tips by Rice [11] and the strain distribution of the crack tip by Antolovich, et al. [12], we can obtain:

$$\epsilon = 2\epsilon_r \left[ \frac{\Delta K^2}{8\pi\sigma_y^2(x+\rho)} \right]^{-\frac{1}{n+1}} \quad (1)$$

At the beginning of the expansion of the crack,  $x=0$ ,  $\epsilon=\epsilon_r$ , that is the real strain, and  $\Delta K=\Delta K_{th0}$ . the above formula can be written as:

$$\Delta K_{th} = 2\sigma_s \left( \frac{E \varepsilon_f}{2\sigma_s} \right)^{\frac{1+n}{2}} \sqrt{2\pi \rho} \quad (2)$$

With reference to [13],  $n$  can be assumed as 1 at the beginning of the expansion of the cracks. Then formula (2) can be simplified as:

$$\Delta K_{th} = E \varepsilon_f \sqrt{2\pi \rho_{min}} \quad (3)$$

where  $\rho_{min}$  is the critical radius of the Crack tip,  $\varepsilon_f$  is the real strain,  $\varepsilon_f = \ln(1/(1-\psi))$ ,  $\psi$  is the attraction coefficient of the Fracture cross-section [10].

Assume the crack is propagating according to the blunting model, and the critical radius  $\rho_{min}$  is equal to one inter-atomic distance; that is, the absolute value of the Bragg vector ( $|B|$ ) as shown in figure 4. for FCC, BCC, and HCP metals, the critical radii  $\rho_{min}$  are equal to  $(a/\sqrt{2})$ ,  $(\sqrt{3} a/2)$ , and  $(a)$ ; here  $a$  is the corresponding lattice constant [14].

(211

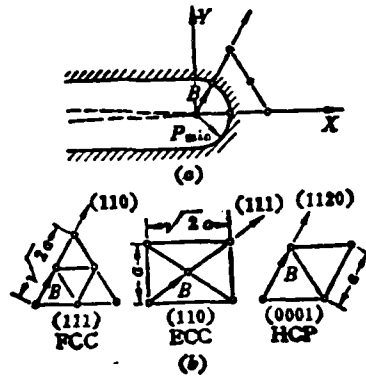


Fig. 4. (a) The blunted critical radii of the tip of fatigue crack. (b) The Burger's vectors of different lattices [10].

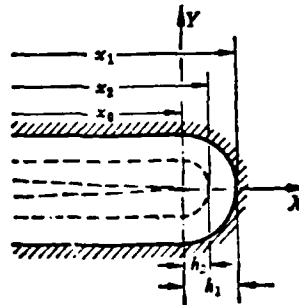


Fig.5. A sketch of the blunting behavior of the fatigue crack under different stress ratios [14].

When the testing sample is applied a cycle load with different stress ratios  $R$  (see Fig. 5), if we consider the relative energy consumption at the plastic blunting, the threshold values for a certain  $R$  and  $R=0$  have the following relation [14]:

$$\frac{\Delta K_{th}}{\Delta K_{th_0}} = \frac{(h_1^2 - h_2^2)/2}{h_1^2/2} = 1 - (h_2/h_1)^2 \quad (4)$$

According to Fig. 5,  $h_1$  and  $h_2$  are the radii of the crack ends for  $R=0$  and certain value  $R$ . Assume  $h_2$  changes linearly with  $R$ , that is:  $h_2 = Rh_1$ , then:

$$\Delta K_{th} = \Delta K_{th_0} (1 - R^2) \quad (5)$$

Substitute formula (5) into (3), a general formula for the threshold value is obtained:

$$\Delta K_{th} = E\epsilon_1 \sqrt{2\pi\rho_{min}} (1 - R^2) \quad (6)$$

材 料 (1)	$E(10^9 \text{ MNm}^{-2})$	$\epsilon_f$	$\rho_{min}$ ( $10^{-10} \text{ m}$ )	$R$	$\Delta K_{th}(\text{MNm}^{-3/2})$	
					计 算 值 (6)	文 献 [15] (7)
低合金钢 (2)	206	0.78	2.84	0 0.33 0.50 0.64 0.75	6.35 5.65 4.76 3.75 2.79	6.6 5.1 4.4 3.3 2.5
18/8不锈钢 (3)	206	0.78	2.58	0 0.33 0.62 0.74	6.46 5.75 4.01 2.91	6.0 5.9 4.6 4.1
Al	69	0.69	2.86	0 0.33 0.53	2.01 1.79 1.45	1.7 1.4 1.2
4.5Cu-Al合金 (4)	71	0.78	2.86	0 0.33 0.50 0.67	2.35 2.09 1.76 1.29	2.1 1.7 1.5 1.2

材 料 (1)	$E(10^5 \text{ MNm}^{-2})$	$\epsilon_f$	$\rho_{min}$ ( $10^{-10} \text{ m}$ )	$R$	$\Delta K_{th}(\text{MNm}^{-3/2})$	
					计 算 值 (6)	文 献 [15] (7)
Cu	98	0.69	2.56	0 0.33 0.58 0.69 0.80	2.72 2.42 1.88 1.41 0.98	2.5 1.8 1.5 1.4 1.3
60/40黄铜 (5)	98	0.92	2.55	0 0.33 0.51 0.76	3.61 3.21 2.67 1.52	3.5 3.1 2.6 2.6
Ni	196	1.05	2.49	0 0.33 0.57 0.71	8.16 7.26 5.47 4.08	7.9 6.5 5.2 3.6
Monel合金 (4)	177	0.92	2.51	0 0.33 0.50 0.67	6.74 5.76 4.85 3.56	7.0 6.5 5.2 3.6
Inconel合金 (4)	206	0.92	2.50	0 0.57 0.71	7.51 4.81 3.76	7.1 4.7 4.0
Ti	107	0.92	2.95	0 0.60	4.24 2.71	— 2.2

Table 2. A comparison of the calculated and experimental results [14].

1-material; 2-low alloy steel; 3-stainless steel; 4-alloy;  
5-brass; 6-calculated value; 7-literature.

Table 2 lists a comparison of the calculated values of  $\Delta K_{th}$  by using formula (6) and the experimental results by Pook [15]. It can be seen that the two values fit well. It should be pointed out that for some complicated multi-phase alloys the calculated values by using the above formulas will have some deviations from the experimental values and the individual contribution of each phase should be considered.

#### PROPAGATION BEHAVIORS OF CRACKS UNDER ALTERNATING LOADS AND AN ESTIMATION OF LIFETIMES

The real lifetimes of parts and components of aircraft are usually quite different from the results of a constant-amplitude experiment. The magnitude, order, and times of overloading, and the history of loading have obviously influences on the lifetimes of components.

1. An evaluation of the effect of retardation effect of overloading and the correspondent models.

Fig. 6 shows the propagation behavior of a LY-12CZ aluminium alloy under different overloading conditions [2]. We can see the retardation effects of single- and multi-compression overloadings ( $D_1$ ,  $D_2$ ) are not obvious; the single- and multi-tension overloadings (B, C) and compression-tension overloading (F) have the most obvious retardation effects; and the tension-compression overloading

(E) has a medium effect.

The research results of the propagation of fatigue cracking of a annealed Ti-6Al-4V alloy under different overloading ratios ( $Q_{OL}=p_{OL}/p_{ca}$ ) have shown that when the overloading ratio was lower than 1.3, no obvious retardation effect was observed; when the overloading ratio was 2.8, the expansion of the fatigue cracking was almost totally stopped. Fig. 7 shows the propagation effects of this alloy under tensile overloading with  $Q_{OL}=2$ . According to the experimental results actually measured, this expansion process can be divided into five stages as the following [16]: The accelerated expansion of the cracking, the retardation effect, the maximum retardation stage, the recovery stage, and the gradual disappearance of the delay effect.

(213

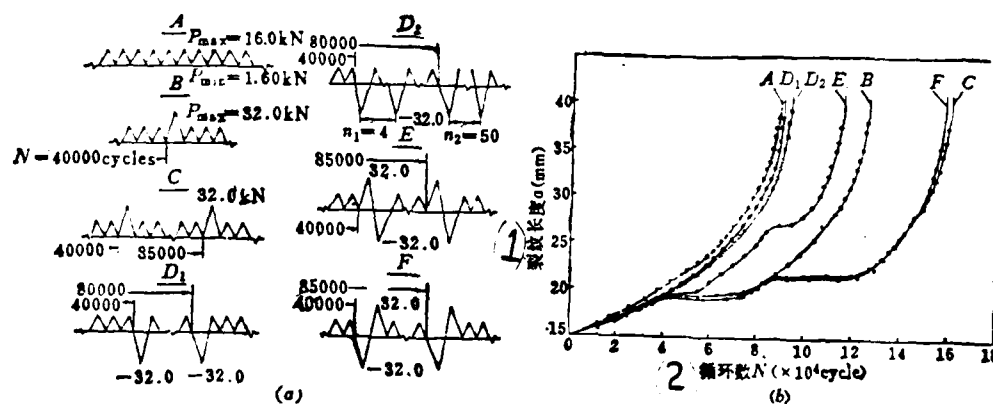


Fig. 6. (a) Various loading conditions and (b)  $a$ - $N$  curves for a LY12CZ Al alloy [3].

1-crack length; 2-cycle number.





In order to compare the precision of the estimated lifetimes by different models, we chose the Wheeler [17] and Willenborg [18] models which are based on residual compress stress and the Maarse [19] and Matsuoka [20] models which consider the closing effect of the cracking. Fig. 7 shows the calculated curves of the Wheeler and Matsuoka models which only consider the residual stress and have larger deviations from the experimental results. But the Maarse and Matsuoka models describe the whole retardation process quite well, and the calculated results of the Matsuoka model is closest to the experimental curve.

Fig. 8 is a comparison of the experimental result ( $N_e$ ) and the calculated results ( $N_{CAL}$ ) by the four models of the lifetimes under the conditions of  $Q_{OL}=1.8$  and  $a=11-35 \frac{mm}{mm}$ . The relative error of the Wheeler model under the adjustment of the retardation coefficient  $m$  ( $m=1.62$ ) is -1.46%. The relative errors of Matsuoka and Maarse models are -1.40% and -10.25%, respectively. The errors of the Willenborg model are +27.98% and -4.19%, according to the different stress conditions (planar stress or planar strain).

2. The improvement of the overloading models and an estimation of the lifetimes of materials.

(214

As described above, among the four models, the Maarse and Willenborg models have larger relative errors and

therefore they need some corrections and improvements.

(1) Corrections of the Willenborg and Maarse models.

The size of the overloading plastic region is an important factor to control the retardation effect. The size  $r_p$  of the plastic region is:

$$r_p = \frac{1}{\alpha\pi} \left( \frac{K}{\sigma_p} \right)^2 \quad (7)$$

Here  $\alpha=2$  for planar stress and  $\alpha=6$  for planar strain.

Considering that the status of the stress and strain varies with  $\Delta K$  and the crack length  $a$ , and usually change gradually from planar strain to planar stress, the coefficient  $\alpha$  in formula (7) can be expressed as the formula (8).

$$\alpha = \frac{6}{1+2S} \quad S = \frac{\Delta K - \Delta K_{th}}{(1-R)K_{Ic}} \quad (8)$$

Here the parameter  $S$  is assumed to be the fraction of the planar stress region in the whole fracture cross section [21].

The propagation rate of the Maarse model which is based on the closing effect is:

$$\frac{da}{dN} = C^*(\Delta K_{eff})^{m^*} = C^*(K_{max} - K_{op})^{m^*} \quad (9)$$

Here  $K_{Op}$  is the stress-strength factor under the crack-expansion loading ( $P_{Op}$ ) and  $C^*$  and  $n^*$  are the experimental coefficients.

Assuming the ratio  $C_f$  of the crack-closing effect is equal to:  $C_f = P_{Op}/P_{max} = K_{Op}/K_{max}$ , then the above formula can be rewritten as:

$$\frac{da}{dN} = C^* [K_{max}(1 - C_f)] \quad (10)$$

According to the experimental results of Bell and Greager [22], the slopes of  $da/dN - \Delta K$  curves of different stress ratios ( $R$ ) are basically parallel to each other. This means that the variation of the experimental index  $n^*$  is small for different values of  $R$ . Therefore we can assume approximately that [21]:

$$n = n^* \\ C^* = C \left( \frac{1-R}{1-C_f} \right)^{n^*} = C \left[ \frac{1-R}{1 - \left( \frac{P_{Op}}{P_{max}} \right)} \right] \quad (11)$$

Considering the continuous change of the stress and strain status at the cracking cross-section, the ellipse formula in the Maarse model is changed as

$$\left( \frac{X - \frac{1}{2a}}{\frac{1}{2a}} \right)^2 + \left( \frac{Y}{0.234} \right)^2 = 1 \quad (12)$$

Here  $\alpha = 6/(1-2S)$  [21].

(2) An estimation of lifetimes under overloading condition with the improved models.

The calculated results with the original and improved Willenborg and Maarse models, and the experimental results of a-N curves under a series of tensile overloading of a Ti-6Al-4V alloy are shown in Fig. 9 It can be seen that the relative errors of lifetimes estimated with the improved Maarse and Willenborg models are reduced to -2.06% and 3.99%, respectively. Therefore the precisions of the estimation are obviously increased.

(3) An estimation of the lifetimes under different loading spectra with the improved models.

(215

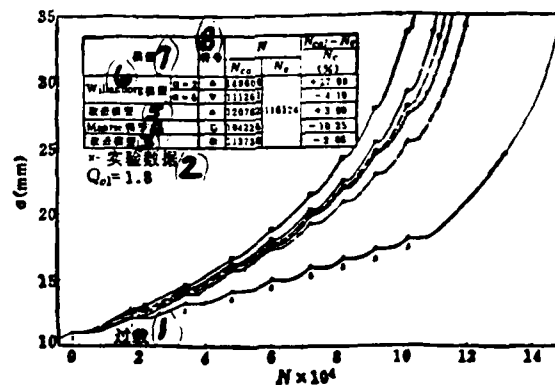


Fig. 9. A comparison of testing and calculated a-N curves by two models and their modified models under tensile overload for a Ti-6Al-4V alloy[21].

1-overloading; 2-experimental data; 3-improved model; 4-model; 5-improved model; 6-model; 7-model; 8-symbol.

The results of the tests and the experimental data for the obtained test-loading spectra are listed in Table 3 [23].

Table 3. A comparison of testing results and calculated data for lifetime predication under spectrum loading [23].

	$S_{max}$ (MPa)	$C_1-C_2$ (mm)	$N_e$ (cycle)	$N_{est}$ (cycle)	$\frac{N_{est}-N_e}{N_e}$ (%)	方 法
1 变平均值法	221	5.0~8.0	17475	12700 13823 18196	-27.33 -20.87 +4.13	LAM Matsuoka 改进法 (4)
2 双波法	238	4.8~9.0	15263	13353 13679 16387	-12.51 -10.38 +7.36	LAM Matsuoka 改进法 (4)

1-varied average value method; 2-double wave method; 3-linear-accumulation method; 4-improved method.

According to Table 3, it can be known that the calculated result of the linear-accumulation method (LAM) has larger errors compared with the experimental result. This is because that this method does not consider the retardation effect under overloading. The result of the Matsuoka model is also not good enough, whereas the lifetime prediction of the improved Maarse model fits well with the experimental result. The material constants of the improved models can be obtained from the constant-amplitude-loading testing. The calculation program is also quite simple and

thus it has good application values in engineering design.

Recently, by using a similar method we also improved the precision of the Willenborg-Chang model [24].

3. The microscopic mechanisms of the expansion of cracking under overloading.

In order to further understand the physical nature and the microscopic mechanisms of the retardation effect under overloading, we have made optical microscope, interferometer, transmission electron microscope, and stress-strain analyses on the fracture cross sections and the tips of LY-12 and Ti-6Al-4V alloys [25, 26].

Fig. 10 (a) and (b) show the changes in the cracking ends and the nearby plastic regions under different overloading modes of a LY-12 aluminium alloy. The changes of the strain ( $\epsilon_3$ ) along the thickness direction in the plastic regions of cracking tips, before and after different overloading modes, are shown in figure 10 (c). In these figures,  $\epsilon_3$  is calculated according to the following formulas [25]:

$$\epsilon_3 = \frac{\Delta Z}{2} = \frac{n\lambda}{2} \quad (13)$$

$$\epsilon_3 = -(\epsilon_1 + \epsilon_2) \quad (14)$$

Here  $\epsilon_1$ ,  $\epsilon_2$ , and  $\epsilon_3$  are the plastic strain in x, y, and z direction, respectively; Z and  $\Delta Z$  are the sample thickness and its increment; n and  $\lambda$  are the order of the interference pattern and the wavelength of the light source.

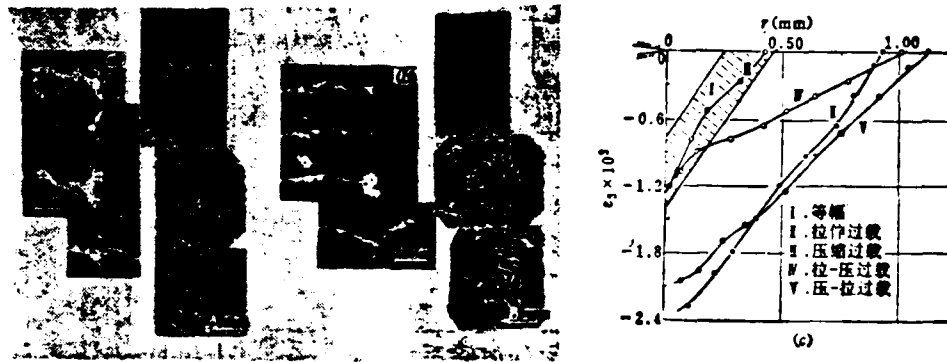


Figure 10. Variation of configuration of crack tips and PZS before and after various overloadings.

(a) tension-compression, (b) compression-tension, (c) variation of  $r_p$  and  $\epsilon_3$  at crack tip under various overloading [25].

I. Stasis; II- Tensile Overloading; III. Compression Overloading; IV. Tension-Compressing Overloading; V. Compression-Tension Overloading.

It can be seen from Fig. 10 that the plastic region and the strain before the overloading are very small; both have increased obviously after the tension and compression-tension overloading; whereas both are almost unchanged after the compression overloading; and after the tension-



compression overloading, although the size  $r_p$  of the plastic region is still unchanged, but the strain  $\epsilon_3$  has decreased obviously and the interference pattern has become less dense. The rear closing length of the crack tip increases with the increase of  $Q_{OL}$ . When  $Q_{OL}=2.4$ , about 1/5 of the crack is in the closed status (see figure 11).



Fig. 11. The crack closure behavior at plastic zone under a tensile overload ( $Q_{OL}=2.4$ ).

(a) macrophotograph; (b) interference pattern [26].

The plastic region within 0.3 mm from the crack tip was investigated with transmissive thin films. The changes of the dislocations in Ti-6Al-4V, in the original and various ratios of overloading conditions, are shown in Figure 12. In the original annealed testing samples, only a small amount

of dislocation lines can be observed (Figure 12(a)); but after the constant-amplitude loading, the dislocations are concentrated in some regions to form belt-like shapes (Figure 12(b)). With the increase of the ratio of overloading, dislocations change from the flake-like network (Figure 12(c)) to some primitive dislocation cells (Figure 12(d)). Finally, the full-cell structures are formed (Figure 12(e)), and the density of dislocations is also increased correspondently.

(217



Fig. 12. The dislocation morphology at 0.3 mm from the crack tip in the plastic zone.

(a) original state, (b)  $Q_{OL}=1.0$ , (c)  $Q_{OL}=1.5$ , (d)  $Q_{OL}=2.0$ , (e)  $Q_{OL}=2.8$  [26].

According to the above observations, the retardation effect of the crack expansion after overloading is mainly

due to the following three factors [26]:

(1) The closing stress behind the crack tips, which prevents the opening of the cracks.

(2) The residual stress in the plastic zone of the crack tips, which prevents the extension of the cracks.

(3) The change and increase of the density of the defects of the crystalline in the plastic zone of the crack tips will further prevent the extension of the cracks.

The tendency of the changes of the overloading plastic zone  $r_p$ , the plastic strain  $\epsilon_3$ , and the circulation number of retardation  $N_D$ , as functions of the ratio of overloading  $Q_{OL}$ , are shown in Fig. 13. The maximum plastic strain  $\epsilon_{3max}$  and the size of the super plastic zone  $r_p$  have the following relation [26]:

$$\epsilon_{3max} = kr_p \quad (15)$$

Here  $k$  is the material coefficient. Under our testing conditions,  $k = -4 \times 10^{-3} \text{ mm}^{-1}$ .

From Fig. 13 we can see that the circulation number  $N_D$  and the ratio of overloading  $Q_{OL}$  also have the following relation [26]:

$$N_D = N_0 \exp(mQ_{OL}^2) \quad (16)$$

Here  $N_0$  and  $m$  are experimental coefficients.

During the experiments, the effects of blunting, the generation of second cracking, the directional switching of crack expansion, and the roughing effect will also influence the retardation effects in various degrees.

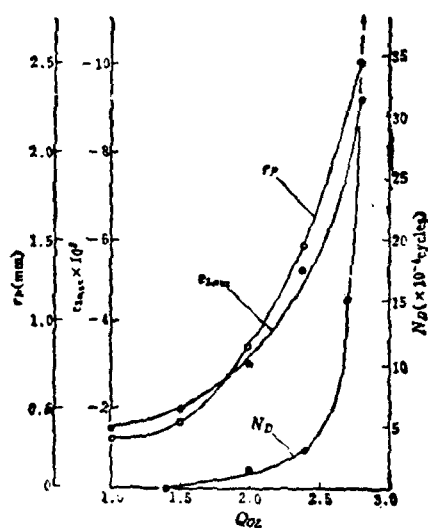


Fig. 13. The effect of overload ratio on  $r_p$ ,  $\epsilon_{3max}$ , and  $N_p$ .

## THE FACTORS WHICH INFLUENCE THE PROPAGATION OF THE CRACKING

### 1. The influence of the microstructure.

The author has made some comments on the influence of (218)  
the material structure to the fatigue characteristics [5, 27]. There was an argument about the influence of the crystalline sizes. For example, the fatigue thresholds of low-carbon and Ti-steel are proportional to the crystalline size  $d^{1/2}$ , but for some high carbon steel  $\Delta K_{th}$  is inversely proportional to  $d^{1/2}$  [28]. This difference is considered due to the relative distance between the constituent units inside crystalline grains and the size of the inverse-type plastic zone before the cracks. When the size of the plastic zone reaches the structural size of the constituent units inside the crystalline grains, the propagation of the crack will transfer from the structural-insensitive type to the structural-sensitive type, therefore making the influence of the grain boundary the second important factor. The decrease of the microscopic size (or the distance) leads to the decrease of the average free distance of the propagation of cracks and therefore the propagation speed is reduced [27].

For some multiple-phase alloys, the fatigue thresholds are also related to the relative concentrations of the constituents. Masounave and Bailon [29] have studied the propagation behaviors of carbon steels with different

concentrations of ferrite ( $\alpha$ ) and pearlite (P), and reported the following relation:

$$\Delta K_{th} = f_{\alpha} \phi_{\alpha} + (1 - f_{\alpha}) \phi_P \quad (17)$$

Here  $f_{\alpha}$  is the the volume fraction of the material and  $\phi_{\alpha}$  and  $\phi_P$  are the formulas representing the influence of  $\alpha$  and P to  $\Delta K_{th}$ .

We have measured the fatigue thresholds of high-strength steels with different isothermal treatments [30]. The relative concentrations of the constituents after three different treatments are shown in Table 4.

Table 4. Microstructures and vol. % of various constituents after different isothermal treatments in high strength steels [30].

组 织 组 成 物 (1)		残余奥氏体 $f_A$ (2)	贝氏体 $f_B$ (3)	马氏体 $f_M$ (4)
状 态 (5)	1	8	25	67
	2	13	50	37
	3	8	36	56

1-constituents; 2-residual austenite  $f_A$ ; 3-residual bainite  $f_B$ ; 4-residual martensite  $f_M$ ; 5-status.

The relation of  $\Delta K_{th}$  and the concentrations of the

constituents can be expressed as the following experiential formula:

$$\Delta K_{th} = 1.95f_M + 7.53f_B + 14.1f_A \quad (18)$$

Here  $f_M$ ,  $f_B$ , and  $f_A$  are the volume percent of the annealed martensite, bainite, and austenite. The contributions of these three constituents to  $\Delta K_{th}$  of high-strength steels are different; that is: M:B:A is about equal to 1:4:7. The above results are consistent with the results reported by Schwalbe [31] on the contribution by 10% residual austenite to the deformation work of plastic deformation of a 4340 steel.

## 2. The influence of stress ratio.

The experimental results have shown that the stress ratio or the average stress has an obvious influence on the behaviors of the fatigue crack expansion at the initial stage. Schmidt and Paris [32] suggested that the influence of the stress ratio to the threshold values can be explained by the crack closing effect. Assuming the material has a fixed threshold values  $\Delta K_0$  and a constant closing strength factor  $K_{cl}$ , when the stress ratio  $R$  is less than  $R_{cl}$ ,

$$K_{th} = K_{cl} + K_0 = \text{constant} \quad (19)$$

$$\Delta K_{th} = (K_{cl} + K_0)(1 - R) \quad (20)$$

When the stress ratio  $R$  is larger than  $R_{cl}$ ,

$$\Delta K_{th} = \Delta K_0 = \text{常数} \quad (21)$$

$$K_{th} = \frac{\Delta K_{th}}{1-R} = \frac{\Delta K_0}{1-R} \quad (22)$$

As shown in Figure 14, such tendency fits with the experimental results of the high strength steel 30CrMnSiNi2A. When the stress ratio is larger than 0.3,  $\Delta K_{th}$  has no obvious changes with  $R$ ; when  $R$  is less than 0.3,  $K_{thMax}$  is close to a constant; when  $R=0.1$ , the fracture cross section in the threshold zone has obvious corrosion trace, whereas such trace was not observed under a high stress ratio. This phenomenon might be due to that under the smaller opening displacement the oxide-induced closing mechanism will take the leading role [33].

(219)

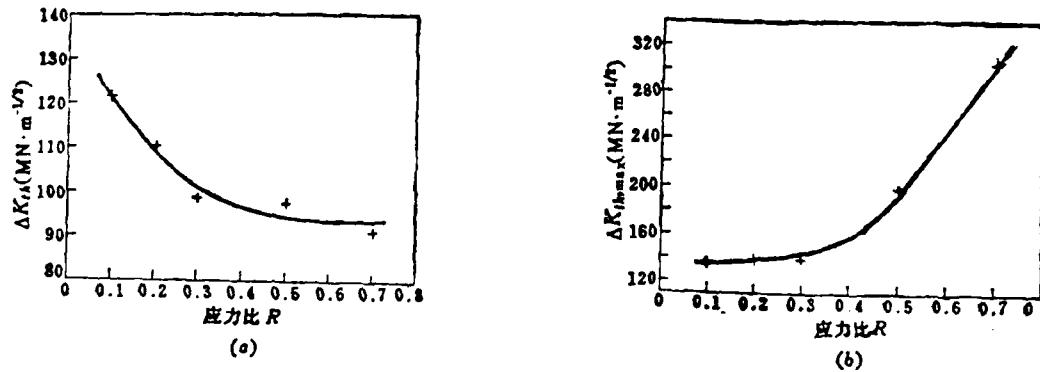


Fig. 14. Effect of stress ratios on (a)  $\Delta K_{th}$  and (b)  $K_{thMax}$  for a 30CrMnSiNi2A steel [33].



The stress ratio has more influence on the threshold values of medium strength steels and aluminium alloys than on that of high strength steels. For example, in LY-12CZ aluminium alloy when  $R$  is large than 0.7,  $\Delta K_{th}$  still has a tendency of further decreasing. This phenomenon might be related to the different closing effects of different materials [34].

### 3. The influence of surface conditions.

Because the fatigue cracking usually begins on inside of the surface layer, the conditions of the surface of testing sample has obvious influence on the fatigue characteristics.

#### (1) Shot-Peening strengthening.

After the material is treated with shot-peening processing, the microscopic structure and the residual compress stress will change and the anti-fatigue capability of the material will be improved [35]. Figure 15 shows the crystalline lattice deformation ( $\Delta a/a$ ), integrated strength ( $\beta$ ), hardness (HV), and the distribution of the residual stress ( $\sigma_r$ ) as functions of the depth ( $d$ ) of surface layer of a 30CrMnSiNi2A steel after shot-peening process [31].

In the recent years, our experimental results of different materials have shown that materials exhibit "circulated hardening" (for annealed metals) and "circulated softening + hardening" (for hardened metals) in the process of shot-peening. Figure 15 shows the changes of the  $\beta$ -d curve along with increase in shot-peening strength  $f$  during the process of the shot-peening of a hardened steel. The existence of these softened zones can explain that the fatigue cracks were produced in sub-surface layer [36].

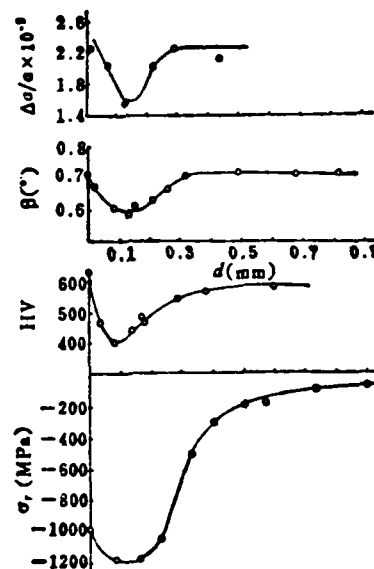


Fig. 15. The variation of structures, hardness, and residual stress at surface layer after shot-peening process in a 30CrMnSiNi2A steel [30]

Furthermore, because the surface residual stress can be as high as 1000 MPa, such high compression stress will cause an anchoring effect on the crack tip and therefore depress the propagation speed of the cracking. This anchoring effect was confirmed by the observation of the fracture cross-section [30].

(220

(2) Expansion hardening.

A great quantity of fatigue analyses have shown that the generation and propagation of fatigue cracks at the edges of connecting holes of a component under stress are the major forms of fatigue failure. Therefore the processing of cold-expansion-hardened connecting holes is widely applied and good results have been obtained. The results of a comparative test of the ratios of 50% survival lifetimes

$(N_x = [N_{ee}] \text{ extruded} / [N_{ee}] \text{ not extruded})$  of four cold-expansion-hardened aircraft structural materials are listed in Table 5 [37].

Table 5. A comparison of fatigue life before and after cold-expansion hardening for four aircraft materials [37].

	$\sigma_{max}$ (MPa)	$N_R = \frac{[N_{80}]_{\#1}}{[N_{80}]_{\#2}}$	备 注(3)
LC4CS	156.9	4.05~7.27	R = 0.1 $\alpha = 5\%$ C = 95%
LY12CZ	191.0	1.85~2.65	
30CrMnSiNi2A	840.6 700.5	1.22~2.66 1.68~5.78	
40CrMnSiMoVA	700.5	1.84~4.25	

1-after cold-expansion hardening; 2-before cold-expansion hardening; 3-notes.

Fig. 16 shows the distribution of residual stress in the strengthened layers of four structural materials, after cold-expansion hardening process. The residual stress in the inside surface of the hole obviously cancels part of the enforced stress, and therefore the ability to resist the expansion of the cracking is increased. Recently, by analysing the residual stress and the effective stress strength factor  $K_{eff}$ , the precision of the predicated life of the crack propagation was improved obviously [37].

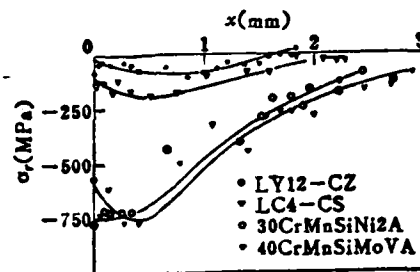
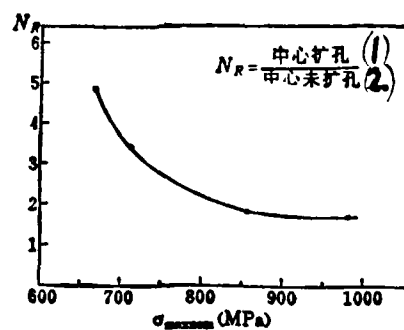


Fig. 16. The distribution of residual stress at cold-expansion-hardened layer for four aircraft materials [37].



- 1 - Center Expanded Hole
- 2 - Center Hole Before Expansion

Fig. 17. The ratios of 50% lifetimes ( $N_R$ ) [37] at different stress levels for a 30CrMnSiNi2A steel [37].

It should be pointed out that the effects of expansion hardening there are different at various levels of stress  $\sigma_{\text{Max}}$ . Figure 17 shows the changes of the life ratio  $N_R$  at various stress levels of 30CrMnSiNi2A steel. It can be seen that at low stress level the effect of the cold-expansion hardening is more obvious, and this is due to the different degrees of the release and re-balance of the residual stress (221 at different stress levels [37]).

#### CONCLUSIONS

Under the conditions of applications, materials are not only influenced by the exterior factors such as the stress state, environment, surface status, geometric size, etc., but also influenced by the interior structures and the fatigue damages produced in manufacture and application. Until now, although some models regarding the microscopic mechanisms, mechanical equations, and design criteria were suggested, the fatigue-crack propagation process of engineering materials, especially the combined effects on the fatigue-cracking process, such as the short crack, threshold value, environment, and other factors, and their engineering applications need further investigation.

In the design of the experimental methods, we should carry out fundamental and applied engineering studies by

considering real conditions of application, such as loading status, environment medium, size effect, etc., combining the macroscopic and microscopic viewpoints, and combining materials with the processing design and machine design, to find out methods of improving the anti-fatigue capability of materials and components for serving the product design, production, and application more effectively.

The author would like to thank Liu Zaimu, Gu Mingda, O Yangji, Su Shaoyei, and Yuan Gaoming for their help in the organization of this paper.

#### REFERENCES

- [1] Ritchie, R. O., Proc. 1st Intern. Conf. Fat. Threshold, Stockholm, Vol. 1, (1981), 503.
- [2] Yan Minggao, Wang Zhongguang, Proc. 1st China-USA Bilateral Metall. Conf., Beijing, (1981), 354.
- [3] Ouyang Jie, Yan Minggao, Proc. Intern. Sym. Fat., ASTM, Dallas, (1984).
- [4] Blom, A. F., Chines Journal of Aeronautical Materials (Special Edition), Vol. 2, No. 1, (1982).
- [5] Yan Minggao, Chine Journal of Aeronautics, Vol. 4, No. 2, (1983), 13.
- [6] Hertzberg, R. W., Mills, W. J., ASTM STP600, (1976), 220.

- [7] Beevers, C. J., Metals Sci. Aug/ Sept., (1977), 362.
- [8] Cottrell, A. H., Trans. AIME, 44, (1936), 192.
- [9] Lynch, S. P., ASTM STP675, (1979), 174.
- [10] Yu Chonghua, Yan Minggao, Fat. Engng. Mat. Struct., 3, (1980), 189.
- [11] Rice, J. R., ASTM STP415, (1966), 247.
- [12] Antolovich, S. D., Saxena, A., Engng. Frac. Mech., 7, (1975), 649.
- [13] Weiss, V., Lal, D. N., Metall. Trans, 5, (1974), 1946.
- [14] Yan Minggao, Yu Chonghua, RES Mech., 10, (1984), 153.
- [15] Pook, L. P., ASTM STP513, (1971), 106.
- [16] Gu Mingda, Zhang Yongkui, Yan Minggao, Fat. Engng. Mat. Struct., 5, (1982), 167.
- [17] Wheeler, O. E., Trans. J. Bas. Engng., 97, (1972), 181.
- [18] Willenborg, J. D., Engle, R. M., Wood, H. A., AFFDL TM 71-LFBR, (1971).
- [19] Maarse, J., Fracture, ICF-3, Vol. 4, (1977), 1025.
- [20] Matsuoka, S., Tanaka, K., Engng. Frac. Mech., 10, (1978), 515.
- [21] Zhang Yongkui, Gu Mingda, Yan Minggao, Chinese



- Journal of Aeronautics, Vol. 3, No. 2, (1982), 91.
- [22] Bell, P. D., Greager, M., AFFDL TR 74-129,  
(1974).
  - [23] Zhang Yongkui, Gu Mingda, Yan Minggao, Proc.  
Intern. Sym. Frac. Mech., ICF, Beijing, (1983), 863.
  - [24] Chang, J. B., Engle, R. M., Szamassi, M.,  
Fracture, ICF, 5, (1981), 2615.
  - [25] Ouyang Jie, Yan Minggao, Chinese Journal of Metals,  
Vol. 18, No.1, (1982), 38.
  - [26] Ouyang Jie, Yan Minggao, Song Deye, Proc. Intern.  
Sym. Frac. Mech., ICF, Beijing, (1983), 769.
  - [27] Gu Minggao, Papers Collection of the First  
Conference of Cracking Mechanics and Cracking Physics.  
(1978), 179.
  - [28] Gerberich, W. W., Moody, N. R., ASTM STP675,  
(1979), 292.
  - [29] Masounave, J., Bailon, J. P., Proc. ICM-2,  
Boston, (1976), 636.
  - [30] Yan Minggao, Gu mingda, Liu Caimu, Proc. 1st  
Inter Conf. Fat. Thresholds, Stockholm, Vol.2, (1981),  
615.
  - [31] Schwalbe, K. H., Engng. Frac. Mech., 9, (1977),  
796.
  - [32] Schmidt, R. A., Paris, P. C., ASTM STP536,  
(1973), 79.

(222

- [33] Zhao Wei, Ding Zhuanfu, Gu Mingda, Yan Minggao,  
Chinese Journal of the Aeronautical Materials  
(Special Edition), Vol. 3, No. 1, (1983), 39.
- [34] Studies on the Fatigue Thresholds of LY12 CZ Aluminum  
Alloy, Technical Reports of the Aeronautical Materials  
Institute, (1984).
- [35] Wang Renzhi, Fat. Engng. Mat. Struct., 2, (1979), 413.
- [36] Wan Renzhi, Liu Xiangbin, Tan Yonggui, Yan  
Minggao, Proc. 1st Intern. Sym. Shot-peening, France,  
(1981).
- [37] Su Xiaoye, Master Thesis in Aeronautical  
Materials Institute. (1984).

Fan Tang

Beijing Institute of Aeronautical Materials

Since the introduction of composite materials in astronautical and aeronautical industries, their advantages are more and more understood by people. Composite materials have high strength to weight ratios, high rigidity to weight ratios, and good anti-fatigue properties. They have excellent design properties and can be formed into integrated components; therefore they can reduce the weight of aircraft, save fuel, improve the performance of aircraft, and reduce the time of manufacturing and the cost of maintenance. All these will not only bring technical benefits but also economical benefits for the aeronautical industry. Therefore composite materials have a large potential of applications in aeronautical industry. It was predicted that in the 90s composite materials will make up 40~50% of the weight of military aircraft, 60% of civil aircraft, and 80% of helicopters.

Recently the application of composite materials in the

---

Received November 23, 1984.

aeronautical industry of China is at a transition stage from research to production. The types of reinforcement materials and resins, which can be used, are few; prepreg materials are not commercially available; the processing methods are still under development; the application in aircraft is still limited to the parts which have small loads or are non-major parts. There is no production capability for processing equipment. Quality control is not perfect. Design personnel lack design criteria and manuals. All these are problems facing us, and we have to solve them. We should properly use successful experiences of foreign countries and can even import some necessary technology and equipment. But we must combine them with the real situation of China and avoid to simply copy every thing. We should not only pay attention to the technical effect but also the economic effect. It is not permitted to carry out some projects for reaching the world's advanced level without considering the cost. In order to steadily develop the composite materials for aeronautical industry of China, we should pay attention to the following three aspects at the same time:

1. Begin to manufacture some non-major-loading parts for building production capability, train technical personnel, and accumulating experience in applications.

2. Develop some parts, which are under load and are

difficult to develop, to improve the processing and design, and prepare the conditions for more applications.

3. Carry out some basic applied research to explore new approaches in materials, new processing methods, and new structural design, etc.

Following are the author's opinions on some of the technical problems in developing composite materials for the aeronautical industry of China.

#### STANDARDIZATION OF INTERMEDIATE MATERIALS

Prepreg materials are the main intermediate materials for the manufacture of composite materials. The next important materials are core materials for different types of layers. The properties of the composite materials depend mainly on the properties of these intermediate materials. Different structures, loading levels, and needs will require different types and specifications for intermediate materials. Therefore in the development of composite materials for aeronautical industry we should first develop different types of prepreg and core materials which are made of different base materials.

##### 1. Reinforcement materials.

Reinforcement material used in large quantity in foreign aeronautical industry are carbon fibers, acyl-base

fibers (e.g. the Kevlar-49 fiber developed by Du Pont Company), and fiber glass. Carbon fibers are mainly high-strength carbon fibers made from primitive acrylic fibers (the tensile strength is 2.5~3.5 GPa, the Young's modulus is 150~300 GPa, the extension rate at break point is 1.1~1.5%). A few are high modulus carbon fibers (tensile strength is (224 1.5~2.5 GPa, Young's modulus is 300~450 GPa, extension rate at break point is 0.5%). In order to improve the durability under shock load, it is required that the carbon fibers should have higher extension rate at breaking point (2.0%). This requirement is achieved currently by maintaining a high modulus and increasing the strength of fibers; the so-called super-high-strength or super-strain fibers. Although the modulus of asphalt-base carbon fibers is high, its strength and extension rate at breaking point are too low. Therefore these materials are not used as structural components except carbon/carbon-composite brake materials [1], [2]. The domestic carbon fibers should be improved in the following aspects:

(1) Stabilizing the quality of high-strength carbon fibers (strength, modulus, and weight per unit length should be less than 8%, 4%, and 3%, respectively, and the length of the fibers should be increased).

(2) Developing surface treatment methods for fibers to

improve the bonding between fibers and resins.

(3) Developing thick-branch fibers to reduce production cost (the fiber branch used widely abroad consists of 6000 fibers).

(4) Developing high-strength (high-strain) fibers.

(5) Developing super-high-modulus fibers.

The quality of carbon fibers is not only influenced by processing methods of carbonization but also, in a large degree, by the quality of raw fibers, therefore we should investigate improving the quality of raw fiber materials at the same time.

Acyl-base fibers have high specific strength, but they easily absorb water and their compressibilities are poor. They are only used in airplane components which are less loaded in foreign countries. We should try to finish pilot production testing and build production capability as soon as possible.

The production bases of fiber glass are already built in China. We should standardize the products of high-strength fibers with reference to international standards and reduce production cost.

## 2. Base materials.

Resin-base materials play the role of bonding fibers and transferring forces, and also influencing the properties of environmental resistance. Most of base materials used in

production are thermal-shaped under low pressure.

According to the requirement of applications, epoxy resins are used for working temperatures less than 130°C, and poly-acyl resins are used for working temperatures higher than 175°C. The recent research effort should be concentrated in resin base materials which solidify at 120~130°C. The research topics in future should be: increasing the storage period at room temperature, improving tenacity, increasing working temperature, reducing solidification pressure (less than 1 atm), and reducing water absorption.

Recently, some foreign countries are developing thermal plastic composite materials. The advantages of this type of materials are high shock strength, low water absorption, simple shaping processing, no storage period limitation, and some can be applied in press processing. Among them the PEEK of British I.C.I. company and PPS of the U.S.A Phillips company are rather mature ones. They have a promising future in the aeronautical industry and we should develop these materials with great efforts.

### 3. Core materials.

Most of light components of aircraft use sandwich structures such as honey-comb of cellulose paper, honey-comb or acyl-fiber paper (e.g. the Nomex paper of Du Pont Company), foamed plastic, aluminium honey comb, micro-ball,



and cork, as core materials. We should solve the technical problems in the production of acyl-fiber paper and honey-comb cores.

#### 4. Prepreg materials.

Both the single-orientation-fiber and fabric prepreg materials are used abroad. Usually civil aircraft use fabric materials to reduce production cost. These materials are convenient for multi-layer fabrication. Military aircraft use single-orientation prepreg materials to optimize design and reduce weight. The strength of carbon fibers will decrease during the fabrication of carbon cloth; therefore carbon fibers are usually fabricated into single-orientation prepreg materials. But most acyl-base fibers and fiber glasses are usually fabricated into fabrics and some are fabricated into spiral wrapped fibers. Recently multi-fiber composite materials are being developed. Besides the different compositions from layer to layer, multi-materials inside the layer are being tested by using fabrics with different materials for latitudinal and longitudinal fibers. We should solve the problems of continuous production of single-orientation carbon-fiber prepreg materials; according to the special requirements, develop different carbon cloth, including three-dimensional carbon cloth and the correspondent prepreg material.

In some foreign countries, the processing method of

materials has been changed from wet methods (solvent methods) into dry methods (thermal-melting or glue-mold method) to reduce the pollution and cost. Furthermore, the content of resin is easier to control. The future tendency is to develop low-resin prepreg materials, which have the same concentrations of resins as composite materials; therefore no glue absorbers are required during solidification [3].

All these experiences are valuable for our reference. I suggest that different composite material, prepreg materials, and core materials should be produced by specialized plants. A national standard of products should be established. (225

#### COMMAND OF PROCESSING METHODS

The processing of composite material components include shaping and solidification, mechanical processing, installation, and defect repairing.

##### 1. Shaping and Solidification.

The shaping and solidification of composite materials include mainly the fabrication of wet layers, by using pulling and squeezing, spiral wrapping, pressure mold, thermal pressing, vacuum bag, and expansion mold [4]. The wet-layer method is not good for the control of the

concentration of resin; therefore it is only limited in the common composite components of fiber glass. The pulling and squeezing method is suitable for large-scale production of shaped materials. Both of these two methods are not very useful in aeronautical industry. The spiral-wrapping method is suitable for the fabrication of spiral bodies such as pressure vessels, tube-like components, and supporting poles. The pressure-mold method has a higher shaping pressure and thus the quality can be guaranteed, but the cost of molds is high. Therefore it is suitable for large-scale production. We already have certain experience in this field. Recently, the major method for aeronautical composite-material components is the thermal-pressing method. The important research topics are: (1) improving the solidification process to obtain less holes, no layer separation, no curving, and less thermal strain; (2) developing co-solidification processing to achieve single solidification of whole components and to reduce the number of parts; (3) developing shape-processing methods of multi-layers; (4) developing automatic processing equipment for cutting and adding layers.

The expansional-mold method uses thermal expansion of rubber or aluminium to produce pressure inside the mold cavity and is a newly-developed technology which can achieve

thermal solidification without using thermal pressing and can be used for solidification of complicated components. But when the limiting diaphragm is used, the pressure is difficult to control and a precise mold is required; therefore the application is limited. But we can use thermal pressing to replace the limiting diaphragm for transferring pressure. This will be suitable for single-time solidification of complicated components and has a promising future. We should pay attention to this method.

The vacuum-bag method was already used in the fabrication of low-pressure-shaped components of composite materials of poly-acyl-base fiber glass. If prepreg materials, which solidify at 1 atm, can be obtained, this method will be a direction of development and no thermal pressured vessel will be required any more.

Many auxiliary materials are required for using the above methods; therefore the supply of these auxiliary materials should not be neglected.

## 2. Mechanical processing and installation.

Composite material components should be fabricated into integrated structures, as many as possible, for reducing the number of components, the amount of mechanical processing, and installation work. Carbon fiber composite material has high hardness and acyl-base fiber material has high tenacity; therefore it is difficult to perform mechanical

processing on these materials. Inadequate mechanical processing might cause the separation of layers and degrade the parts; therefore attention should be paid to these problems. Carbon-fiber composite material can be processed with high-speed steel, hard alloy, or diamond sand tools; but the lifetimes of tools will be shortened. Recently, high-pressure water cutting was developed and good results were obtained. This method is especially suitable for acyl-base fiber composite material [5]. In order to avoid electric corrosion, Ti-alloy connecting parts are used in joints of carbon fiber composite materials. We should organize domestic supply of these parts. In some foreign countries composite materials are being used as connecting parts. The completed components should be painted for protection, and the surface facing the wind should be coated with grinding-resistant layer to avoid sand and water erosion.

### 3. Repairing.

Defects can not be totally avoided in use; therefore some repair work is always required. We should develop repair technology for on-site repair service. We have already certain experience in repairing of fiber-glass composite material components and further experiences should be accumulated.

## GOOD STRUCTURAL DESIGNS

Structural design of components using composite materials will not only influence the technical effects but also the economic effects. After the material and processing problems are solved, design will become the most essential technical problem for developing composite materials.

(226

### 1. Procedures of development.

The application of composite materials in aircraft can be divided into three stages. At the first stage they should be applied to components which are only under light load, such as lids, cabin doors, flow regulating plates, etc. At the second stage, they should be applied to components which are non-major loading parts, such as decelerating plates, second wings, edge wings, tails, etc. At the third stage, they should be applied to components which are major-loading components, such as the main wings and body. China is now at the second stage of development. We should carry out studies for transferring to the third stage in structural design work.

### 2. Material selection.

In order to obtain the maximum effects of using composite materials, it is important to select the right materials. The intermediate materials should be selected according to loading and working environment. The tendency

of only considering carbon-fiber materials as composite materials without considering cost should be avoided. In this aspect, foreign experience should be referenced. Either for military aircraft, civil aircraft, or helicopters, multi-type materials are being used and multi-fiber composite materials are being developed.

### 3. Optimization of design.

Besides the high specific strength and high specific rigidity, another distinct advantage of composite material is its excellent design property, and that it can be shaped into integrated bodys. We should fully use these advantages during design. At the initial stage of development, because we lack experiences, equal-substitution method was usually used and only higher specific strength and higher specific rigidity can result. For example, about 20% weight can be reduced if carbon-fiber composite materials are used. We should gradually switch into structural and layer-fabrication design work according to the properties of the composite materials selected. Not only loading situation but also the feasibility of processing should be considered. Pneumatic cutting technology should be developed gradually by considering the loading spectrum and fully using the anisotropic properties of composite materials. Thus we can further reduce the weight from about 20% to 40-50%, and can

even achieve the design of new type aircraft by replacing the forward wing with a downward wing.

Special attention should be paid to the joint design of composite materials. An inadequate joint design will lead to early joint damage and then will reduce the benefit of using composite materials. China has accumulated certain experiences in the design of fiber glass, and this can be referenced for designing carbon-fiber and acyl-base-fiber composite materials.

#### 4. Testing, reference manuals, and standards.

Composite material is a very new material and experiences is lacking worldwide. Although foreign experience can be referenced for structural design, we must consider the properties of domestic materials in designing layer fabrication and joint forms. The design plan should be made via necessary component testings; and static and fatigue testings should also be carried out under real environment if necessary. Material departments should offer mechanical, physical, and chemical properties of all composite materials and typical sandwich-layer structures. Data base should be built and material reference manuals should be edited. Design departments should accumulate testing data of all typical layer fabrications and structural components by combining strength calculation to establish design criteria. This is a fundamental task for developing



composite materials and should be well organized to avoid repeated work. Mature experiences of foreign countries should be referenced as much as possible in preparing these manuals and criteria.

#### BUILDING QUALITY CONTROL SYSTEM

The ultimate goal of developing composite materials is to put these materials into production. After the technical problems of materials, processing, and structural design are solved, plant buildings, equipment, technical training of production personnel, and measures for stability of product quality should be solved. Here we discuss the quality stability problem.

##### 1. Testing when materials are shipped to plants.

Fibers, fabrics, resins, prepreg materials, core materials, and other raw and intermediate materials must be tested according to the regulations before production. Special attention should be paid to the diversity and changes of properties of fibers and prepreg materials. Each batch of materials should be tested rigorously; even auxiliary materials are required certain simple property testing. Infrared spectrum and high-pressure liquid-chromatography testing should be listed as the technical requirements of materials.

(227

## 2. Control of processing.

During the processing of composite materials, small molecules are synthesized into large molecules. Therefore the quality control during material processing is especially important. The solidification conditions of each product should be decided according to the results of thermal analysis and shape of the product. On-line control should be used if necessary. The testing samples for each batch of materials must represent the true properties of the products. Processing record card is required for each product to record batch numbers and processing parameters. These cards must be signed by operating and testing personnel. In case material failures are found, the causes can be traced by using these cards.

## 3. Testing of final products.

The final products of composite material components must undergo size, outside appearance, and non-destructive testing. Recently, non-destructive testing is developing very fast such as supersonic C-scanning, micro-waves, turbulent, laser holography, acoustic emission, etc. Each of these techniques has special features and is suitable for testing certain material defects such as holes, layer separation, deviation of concentration of resins and fibers, etc. We should select suitable ones according to component

structure, loading status, and processing method [6]. Standard samples and defect tolerances for each method should be established. The development of these standards should be based on the results accumulated in everyday testing. The analysis of damaged samples during testing is the best basis for building these standards. These testing standards can be revised continuously in practice. Furthermore, some foreign countries are building automatic testing equipment according to the needs of production.

#### 4. Standardization.

The whole procedures of fabrication of composite materials, from the delivery of raw materials to shipping of final products, must follow certain regulations. Any testing item should have a standard. Correspondent supervising measures must be built. Testing instruments and processing equipment must be checked periodically. Temperature, humidity, and cleanliness should be controled in workshops of cutting and layer fabrication. Operating personnel must be specially trained and pass examinations, etc. All these measures form an integrated quality control system. China lacks a rigorous system of this kind. We should start from technical and administrative viewpoints to improve the quality control system for guaranteeing the quality of products.

## CARRYING OUT APPROPRIATE FUNDAMENTAL APPLIED RESEARCH

In developing the applications of composite materials in aeronautical industry of China, many problems that need to be solved are specific technical problems. We can use the available scientific theories and successful foreign experience to accelerate the speed of development. At the same time, according to the needs, we should carry out some fundamental applied research work to guide the future development work. Following are some examples:

(1) The study of solidification system and process of resins for solving the problems such as increasing the heat resistance, extending the storage period of prepreg materials, reducing solidification temperature and pressure, shortening solidification period, preventing generation of holes, reducing thermal stress of products, etc. All these will give new directions for developing new solidification systems and new processing methods.

(2) The study of interfaces, mechanisms of strengthening and damage. This will give directions for improving the mechanical properties of composite materials from the viewpoints of processing and materials.

(3) The study of the influence of the environment (including temperature, humidity, and time) on the properties of composite materials. This will help us to

obtain properties of different composite materials in different environments.

(4) The study of material mechanics of multi-fiber composite materials. This will solve the problems of strength calculation and design optimization.

(5) The study of damage mechanics, and fatigue and cracking characteristics. This will offer a theoretical basis for safety design and working lifetime prediction.

(6) The study of the reliability of property testing.

#### CONTINUING THE PRE-RESEARCH OF METAL-BASE COMPOSITE MATERIALS

(228

Compared with resin-base composite materials, metal-base composite materials have the advantages of higher working temperature, better transversal mechanical properties, higher inter-layer shearing strength, higher heat conductivity, higher electrical conductivity, higher anti-grinding resistance, non-aging, stable size, etc. The United States has carried out research in this field for about 20 years. Recently, B-Al composite material has been used in turbine engines for fan blades and air-compressor blades for testing. This material has also been used in cabin frames, checking doors of engine components, and frames of space shuttles. Directional-solidified high-temperature alloys and W-reinforced high-temperature alloys

were tested in turbine blades and satisfactory results were obtained [7]. Recently, progress was obtained in C-Al composite materials. But the cost of metal-based composite materials is high, and the technical problems of processing and property control are difficult; therefore only few were at the stage of production. China began to explore this field since the 70s. Because of the high cost and slow progress, it was not given appropriate attention. From now on, this work should be organized by government and pre-studies should be made. When the conditions become mature, this new material can be applied to the development of new type aircraft types and therefore we can avoid losing time and missing opportunities. Besides the research work on the technical problems of processing, certain fundamental research work, such as the reactions at the fiber-metal interface, principles of mechanics, and structural design, etc, can be carried out to a certain degree.

## CONCLUSIONS

Composite materials are the products of the development of material science and is one of the important fields of the new technological revolution of the world. The production of composite materials is also a result of cooperation between fiber, large-molecule material,

mechanical, and aeronautical industries. Recently, China is facing the challenge of this new technological revolution. Our task is to use this chance to organize forces of all related fields to enlarge the applications of composite materials in aeronautical and astronautical industry.

#### REFERENCES

- [1] Discussion of Carbon Fibers, Strengthened Material - Carbon Fibers (a Japanese Journal), Vol. 29, No. 3, 1983.
- [2] Fitzer, E., Technical Status and Future Prospects of Carbon Fibers, Papers presented at the Conference on Applications of Carbon Fibers, Brazil, Dec., 1983.
- [3] Molyneux, M., Prepreg, Tape and Fabric Technology for Advanced Composites, April, 1983.
- [4] Hayes, B.J., Review of Fabrication Processes for High Performance Carbon Composites with Special Emphasis on the Technology of Prepregs, Papers presented at the Conference on Applications of Carbon Fibers, Brazil, Dec., 1983.
- [5] Brunsch, K., Fabrication of CFRP structures, MBB GmbH.
- [6] Teagle, P.R., The Quality Control and Non-destructive Evaluation of Composites Aerospace Components, Composites, April, 1983.
- [7] Kinner, W.K., Metal Matrix Composites, Material Engineering, Vol.91, No.1, 1980.

INVESTIGATION ON TEMPER BRITTLINESS OF  
GRANULAR BAINITE IN 15CrMoVA STEEL

Liu Zhengtang, Kang Mokuang, and Yang Zheng

Northwestern Polytechnical University

ABSTRACT

The investigation shows that the granular bainite structure has an obvious non-reversible temper brittleness.

INTRODUCTION

Bainite structure is usually obtained in low concentration structural alloys after constant isothermal and continuous cooling treatment. This type structure has many advantages in processing and mechanical properties for steel and therefore attention was paid both in China and foreign countries. The structural characteristics and transformation mechanism were studied [1-4]. Granular bainite was usually used after a temper treatment, but the changes of structural and mechanical properties during temper treatment were not fully studied, and the temper brittleness was even rarely investigated. This situation

---

Received June 5, 1984.



prevents further understanding and control of the bainite structure and full use of its property advantages. Therefore the study of temper brittleness is important in both theory and practice. -

This paper reports the structure changes, during temper, of granular bainite obtained in 15CrMoVA steel after air cooling and discusses the mechanism of the temper brittleness of granular bainite of this steel; therefore it provides a theoretical basis for selecting the proper tempering temperature.

#### METHOD OF TESTING

Material tested is a 15CrMoVA (15CDV6) hot pressed steel plate 5mm thick. The chemical contents (weight-%) are as follows:

C	Cr	Mo	V	Mn	Si	P	S
0.156	1.36	1.03	0.34	0.89	0.13	0.013	0.009

All samples were cut along the direction of rolling. The parameters of heat treatment are: a 40-minutes austenite transformation at 975°C, then an air-cooling treatment, then an 1-hour temper treatment at 200~700°C followed by another air-cooling treatment.

The room-temperature impact toughness after different temper temperatures was measured by a single-impact test using a V-type opening.

The analysis of stress-rupture cross-sections was carried out with a scanning electronic microscope. Structural observation and electron diffraction were carried out at an EM-400, a JEM-200CX, and a DXA4-10 transmission electronic microscopes and the samples were metallic thin films, secondary replica, and extraction replica.

The quantity of decomposition during the temper treatment and the quantity of transformation during the cooling treatment, of the retained austenite, were determined by a 3500-Gauss thermal-magnet meter. Heating and temperature keeping were obtained in a Pb-Sn bath furnace and magnetic field strength was recorded by an X-Y recorder.

(231

## RESULTS OF TESTING AND DISCUSSION

### 1. The temper brittleness of the granular bainite.

The structure of the air-cooled 15CrMoVA steel is ferrite with an island-like granular bainite distribution as shown in Fig. 1 (a). Results of electron diffraction show that this island-like structure is usually a martensite-austenite (M/A) mixture; some are single martensite or austenite. When this island-like structure is the M/A

mixture, the austenite usually distributes in the outer region (Fig. (b) and (c)). The results obtained by a Leitz image analyzer show that the volume ratio of martensite to austenite is 20.5%. The residual volume of austenite is 10.5% by magnetic method.

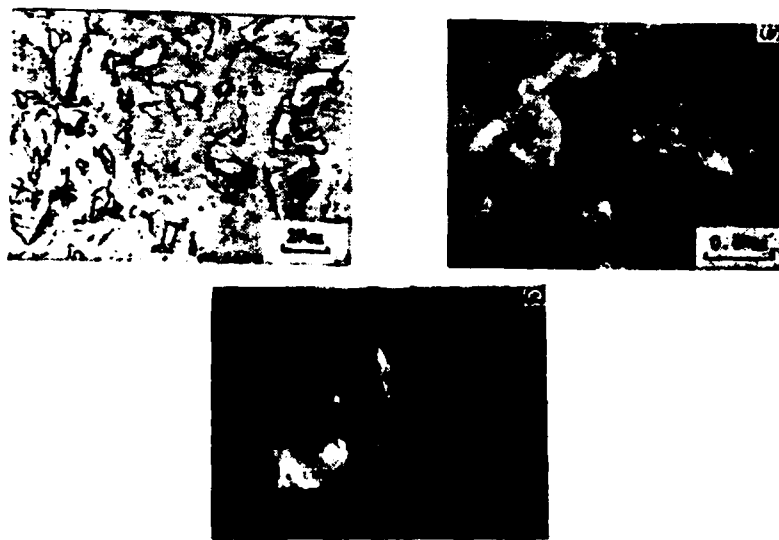


Fig. 1. The electronic microscopic images of the material structures after an air-cooling treatment. (a) Second replica, (b) TEM bright field image, (c) Dark field image of retained austenite.

Figure 2 shows the changes of mechanical properties of granular bainite in 15CrMoVA steel after a series of temper treatments. Room temperature toughness ( $\alpha_k$ ) increases along with the initial increase of temper temperature, achieves peak value at 250°C, decreases abruptly at 300°C, and begins to improve at 400°C. The results show that the granular bainite structure in 15CrMoVA steel has an obviously temper brittleness and the temperature range of this brittleness is very wide. Under the testing conditions of our experiments, the brittleness at higher temper temperature is non-reversible; even a fast cooling process after the tempering cannot eliminate this brittleness phenomenon. In this paper we define such brittleness of the granular bainite structure in steel after a temper treatment as granular-bainite temper brittleness.

The analysis of stress-ruptured cross-sections shows that the single-impact stress-ruptured cross sections are mainly tenacity holes for the air-cooled and low-temperature-temper-treated samples; whereas the breaking cross-sections in the temper brittleness range are typical parabolic fracture fractures as shown in figure 3. No evidences are found across the crystalline grain bound.

2. The decomposition of the island structures during the temper treatment.

Electronic microscopy observation shows that no obvious changes of the ferrite in the bainite of 15CrMoVA steel can be observed during the temper treatment under 450°C, and some carbide decomposition can be observed when the temperature is above 500°C. (232

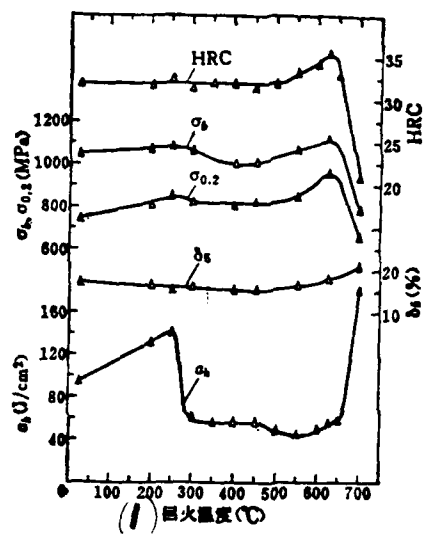


Fig. 2. Mechanical properties vs tempering temperature.  
1-tempering temperature.



Fig. 3. SEM Fractograph after tempering at 625°C.

The decomposition of the island-like structure at the tempering temperature should be the combination of the decomposition of both austenite and retained martensite. Figure 4 is the quantities of residual austenite ( $A_{rd}$ ), quantity of transformation ( $A_{rt}$ ) vs tempering temperature, measured by a thermal-magnetic meter. It can be seen that austenite has relatively higher stability during the tempering under 250°C, whereas a large quantity of austenite is decomposed during tempering at 300~400°C. The products of the decomposition are ferrite and carbides. When the samples are tempered above 400°C, part or most of the retained austenite decomposed will transform into martensite during the cooling. We define such product of transformation as untempered martensite. The transformation of retained martensite during the temper cooling is due to the partial decomposition during the tempering and the reduction of carbon concentration, and also due to the catalysis effect (anti-stabilization effect) [5] which reduces the stability of the retained austenite.

Fig. 5 is the structure pattern after a 300°C temper treatment. Non-uniform flake-like carbides exist at the former island-like structures. By a large amount of observations on the structures, we found that most of these

carbides exist in the vicinity of the former island-like structure. According to the features of the distribution of the retained austenite in the island-like structure, we found that these carbides are formed by the decomposition of the retained austenite. The diffraction of thin metallic film and extraction replica show that these flake-like carbides are carbonized. It should be mentioned that the carbides produced by the decomposition of the M/A island-like structures after a 625°C tempering are most flake-like (Fig. 6) and the structure is still carbonized. The structure after a 550°C-temper treatment is shown in figure 7, and both dark field and electron diffraction have confirmed the existence of the untempered martensites.

(233

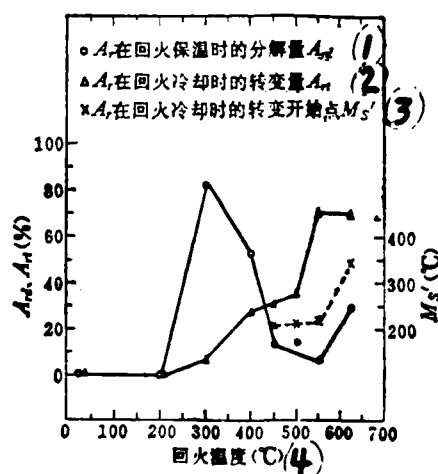


Fig. 1. Relationship between austenite transformation and transformation vs tempering temperature in the retained austenite. (The amount of the retained austenite is normalized to 100%.)

(1)-amount of decomposition of retained austenite during constant temperature stage of tempering; (2)-amount of decomposition of retained austenite during cooling stage of tempering; (3)-starting points of transformation of retained austenite during the cooling stage of tempering; (4)-tempering temperature.

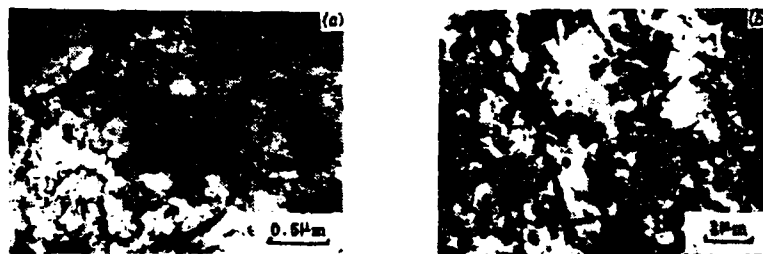


Fig. 5. Microstructure after tempering at 300 °C.

(a) Soil, (b) Extraction replica.

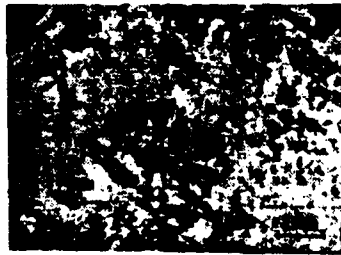


Fig. 6. Microstructure after tempering at 625 °C.

(Extraction replica).



3. The mechanism of the tempering brittleness of the granular bainite.

According to the results of the above testing, during the brittleness process of the granular bainites, the mechanism of stress-rupture changes from the micro-hole gathering type into quasi-cleavage fracture type. At the same time, a large amount of retained austenite decomposes forms non-uniformed flake-like carbonized structures. The results show that the phenomenon of quasi-cleavage fractures is correlated with the existence of the flake-like carbonized structures. This is because under the influence of stress, the movement of dislocations in the matrix will be blocked by the flake-like carbonized structures to form an accumulation of dislocations, and eventually to form a cracking at the interface of ferrite and carbon diffusers. Meanwhile, the flake-like carbonized structures are a brittle phase which is less plastic and have a stronger binding with the base matrix. Under impact loading, they will crack when the stress is concentrated to a certain degree. Either the cracking formed at the boundaries between ferrites and carbonized structure or the cracking of the carbonized structure itself will become the cracking sources for the subsequent quasi-cleavage [6-8].

The analysis of structures shows that the carbonized structures formed after the decomposition of the M/A island-like structures will still retain the flake-like structures and have a non-uniform distribution, after a tempering up to 650°C. According to the above discussion, such flake-like structure and non-uniform distribution are the major causes of the brittleness of steel even after a higher temperature tempering. If we consider the concentrations of alloy elements in the steel, we can estimate carbon concentration in untempered martensite after a 625°C tempering is 0.3%, and 0.6% after a 450~550°C tempering, by using the experiential formula of  $M_s$  and the measured point  $M'$ s (figure 4). Although such calculation is not very accurate, at least it can show that the carbon concentration of untempered martensite is quite high. The toughness of these untempered martensites is very low and therefore they are the source of cracking [9]. Therefore, the wide temperature range of tempering brittleness of granular bainites is also correlated to these untempered martensites.

4. Selection of tempering temperature for the granular bainites.

The results of our study show that the tempering brittleness is caused by the decomposition of the M/A island-like structures during the tempering. For the

AD-A179 673

ACTA AERONAUTICA ET ASTRONAUTICA SINICA(U) FOREIGN  
TECHNOLOGY DIV WRIGHT-PATTERSON AFB OH 07 APR 87

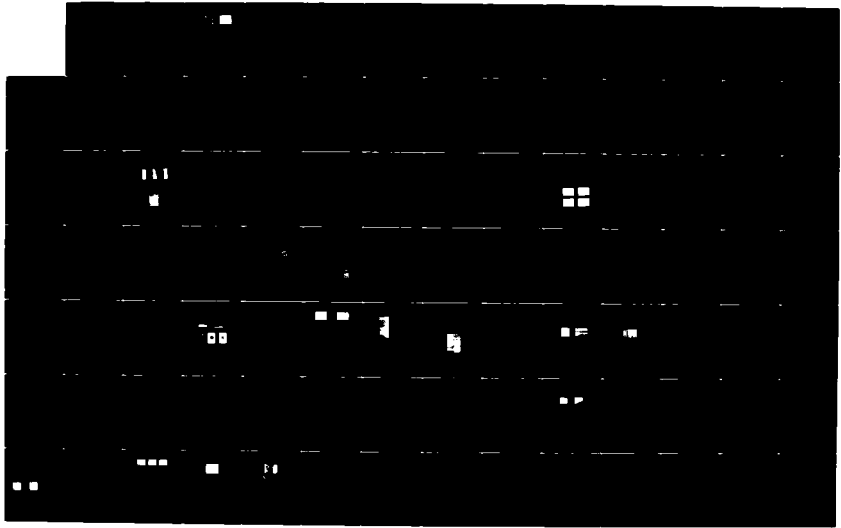
2/3

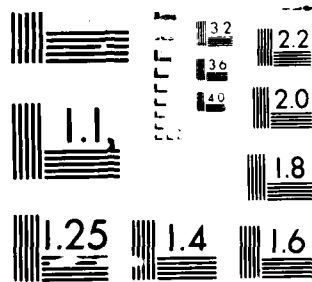
UNCLASSIFIED

FTD-ID(RS)T-1246-85

F/G 13/8

NL





MICROCOPY RESOLUTION TEST CHART  
NATIONAL BUREAU OF STANDARDS-1963-A

bainites which have no obvious decomposition of the island-like structures, because of the existence of the retained austenites which have a high toughness, the breaking resistance will be improved. Furthermore, because of the existence of the flake-like carbonized structures which are not brittle, the chance of the cracking nucleation is rare and thus the toughness of the steel becomes higher. Therefore, under the prerequisite of satisfying the requirement of strength, the tempering temperature should be selected within a proper range to guarantee no obvious decomposition of the island-like structures and thus achieve a good toughness.

After a 200~250°C tempering of an air-cooled 15CrMoVA steel, because no obvious decomposition of the island-like structures is observed, very high toughness is obtained. At the same time the strength and impact durability are quite high. Therefore, we suggest that, for 15CrMoVA structure steel to be used at normal temperature, if the structures are mainly granular bainites, the tempering temperature range should be 200~250°C.

#### CONCLUSIONS

1. The main structure of air-cooled 15CrMoVA steel is granular bainite. The M/A island-like structure will



Fig. 7 TEM microstructure after tempering at 550°C  
(a) Bright field image (b) Dark field image of martensite

decompose in some degree when the temperature is above 250°C.

2. The granular bainite of 15CrMoVA steel has an obvious non-reversible brittleness with wide temperature ranges. Such brittleness is due to the decomposition of the M/A island-like structure.

3. The temperature range of the tempering of granular bainite should be selected in the range in which no obvious decomposition of the island-like structure will be caused.

#### ACKNOWLEDGEMENT

Changhe Mechanical Plant offered the testing materials for this study, and the testing work was helped by Lu Juliang, Fong Yieping, of Peking General Research Institute of Steel and Iron, Yang Meihua, of Xian Research Institute of Coal and Geology, Wang Lijin, of Xian Research Institute of Thermal Engineering, and colleges of Teaching and Research Section of Xian University of Polytechnology. The authors would like to thank them for their help.

#### REFERENCES

- [1] Kang Nukuang, et al, M-A Structure in Low Concentration Structure Alloys, Physical Section, Physical and Chemical Testing, 1979, 5, p. 1.

- [2] Fang Hongsheng, et al, The structure and Strengthen-  
Tanicity of Granular Bainite in Low Carbon Fe-Mn-B  
Steel, Materials of Mechanical Engineering, Vol. 6,  
1981, 1, p 5.
- [3] Bush, M. E. and Kelly, P. M., Acta Met. Vol. 19, 1971,  
p 1363.
- [4] Honeycombe, R. W. K. and Pickering, F. B., Met. Trans.  
Vol. 3, 1972, p 1099.
- [5] Xu Zuyao, The Martensite and Its Transformation, Science  
Press of China, 1980, p 462.
- [6] Lindley, T. C. et al, Effect of Second-Phase Particles  
on the Mechanical Properties of Steel, ISI, 1971, p 54.
- [7] McMachon, Jr. C. J. and Cohen, M., Initiation of  
Cleavage in Polycrystalline Iron, Acta Met. Vol.  
13, 1965, p 591.
- [8] Xiao Jimei, The Toughness and Tenacilization of Metals,  
Shanghai Science and Technology Press, 1980, p 254.
- [9] Marder, A. R. and Krass, G., The Morphology of Martensite  
in Iron-Carbon alloy, Trans. ASM, Vol. 60, 1967, p 651.



## DIRECTIONALLY SOLIDIFIED BLADE SUPERALLOY DZ-22

Wang Luobao, Chen Rongzhang, Wang Yuping

Beijing Institute of Aeronautical Materials

### ABSTRACT

(236

The directional-solidified (DS) high-temperature DZ-22 possesses rather excellent mechanical properties at both intermediate and high temperatures. Its properties are comparable with the DS alloy PWA1422. Therefore, it is applicable to turbine blades for advanced aircraft engines. The DZ-22 is based on the composition of PWA1422 alloy, but the content ranges of hafnium and carbon have been readjusted according to the experimental results. The drawn rate of shell mold during the DS process obviously affects the orientations of columnar crystals. An enhancement of solution temperature during heat treatment can improve stress-rupture lifetime at high temperatures, while the elongation decreases slightly. A pre-treatment at 1150°C prior to the solution treatment can raise the incipient melt temperature.

Since the 70s, high-temperature alloys and components manufactured by using directional-solidification technology

were transferred from laboratories to production. Several directional-solidified alloys with excellent combined properties, such as PWA1422, ЖС6KH, DSMAR-M002, DSR80H, etc., have been put into wide applications. These materials have promoted effectively the development of aircraft engines. Among them, DZ-22 alloy is one of the directional-solidified alloys with excellent properties. Its high stress-rupture properties is equivalent to the foreign directional-solidified alloy PWA1422 and has excellent casting and hot impact properties.

#### METHOD OF TESTING

The base alloy was made in a vacuum induction furnace. The solidified sample-plates and components were made in an ISP2/III-DS directional furnace by using a drawing-shell mold. The sample plate has a size of 240X80X15 mm. The casting mold is an aluminium-oxide-shell type.

The samples for mechanical property testing are cut from the plate or the component. Testing sample was heat-treated before mechanical processing followed by a 2-hr-1205°C air cooling and a 32-hr-870°C air cooling.

The mechanical properties were tested in atmosphere according to the HB (the Aeronautical Industry Ministry Standard of China) standard.

Microscopic structures and micro-regional chemical content analyses were carried out by using the conventional metallograph, transmission electronic microscope, scanning electronic microscope, electron probe, chemical phase analysis, etc. The deviations of crystal orientations were determined by using the scanning X-ray-diffraction method (the  $\omega$ /X scanning) [7].

## RESULTS AND DISCUSSION

### 1. Determination of chemical content of alloys.

The content of DZ-22 alloy is based on the content of PWA1422 alloy [1,2], with certain adjustment of Hf- and C-content through testing.

Literature [3,4] had proved that adding Hf in directional-solidified Ni-base high-temperature alloy can improve medium-temperature properties; especially the transversal stress-rupture properties at medium temperature and casting properties of the alloy. Because Hf is an element which will strongly tend to exist between crystal branches, most of Hf enters  $\gamma'$ -phase; besides, some quantities of Hf-rich phases, such as  $(\text{Hf}_x\text{M})\text{C}$ ,  $\text{Ni}_3\text{Hf}_x(\text{Hf}_x\text{M})_2\text{SC}$ , etc., are formed,. This will reinforce  $\gamma'$ -phase and a large quantity of cocrystallized  $\gamma'$ -phase will be formed between the crystal boundaries and crystalline

(237

branches; therefore the status of grain boundaries and inter-crystalline branches will be improved. All these are good for improving medium-temperature properties of the materials. From Fig. 1 we can see that the stress-rupture properties at 760°C, especially the durability properties in transversal direction, are improved obviously. But the durability lifetime at 1040°C is decreased along with the increase of Hf concentration. This is caused by the harmful influence of the excess quantity of cocrystallized  $\gamma'$ -phase under the high temperature stress [4]. In order to balance the medium and high temperature properties, the concentration of Hf in DZ-22 alloy was set as 1.0-2.0 wt.%. The results of casting thin-wall inner-hollow blades (with a minimum wall thickness 0.7mm) have shown that this alloy has good casting properties.

A suitable concentration of C is a condition for the formation of carbides which have favorable high-temperature properties. Furthermore, it can adjust alloy contents and structures. When the concentration of C in DZ-22 alloy is below 0.10 wt.%, the 1040°C stress-rupture lifetime drops obviously (see figure 2). The carbides in the micro-structures decrease, the  $\text{Ni}_3\text{Hf}$ -phase increases, and the incipient melting temperature drops, obviously. For example, when concentration of C drops to 0.05 wt.%, the incipient

melting temperature of the alloy will drop from 1230°C to 1150°C. Furthermore, when the concentration of C is too low, the structural stability will be deteriorated and a tendency for  $\eta$ -phase separation is obvious. All these are the causes for the deterioration of high-temperature properties. Based on the above experimental results, the concentration of C in DZ-22 alloy was determined as 0.12-0.16 wt.%.

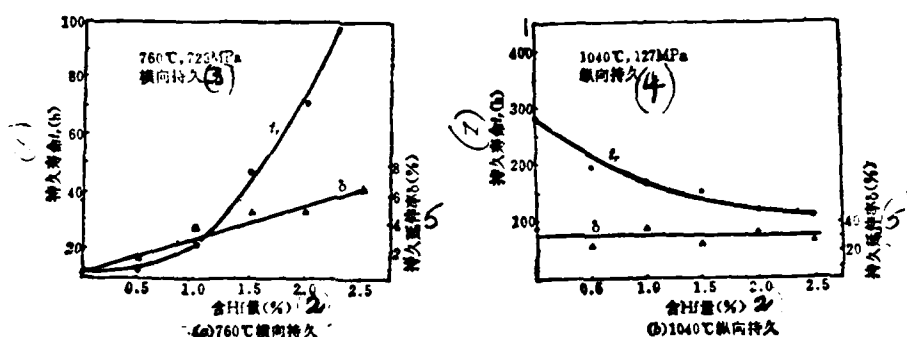


Fig. 1. Effect of hafnium on the stress-rupture properties of DZ-22 alloy.

(a) 760°C transverse stress-rupture, (b) 1040°C longitudinal stress-rupture.

1-stress-rupture lifetime (h); 2-concentration of Hf; 3-transverse stress-rupture; 4-longitudinal stress-rupture. 5-stress-rupture extension coefficient

In order to obtain good casting properties, no Zr, which is added into the conventional high-temperature

casting alloys, was added into the alloy. We do so because: literature [5] and [9] and another test of the author of this paper have proven that when the concentration of Zr is higher than 0.03%, the casting properties will be deteriorated (likely to form thermal cracking). In the test of this paper, a comparison of mechanical properties, with and without adding Zr, was made. The results show that the mechanical properties have no obvious difference.

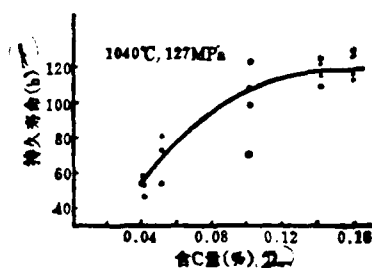


Fig. 2. The influence of C concentration to stress-rupture properties of DZ-22 alloy.

1-stress-rupture lifetime; 2-C-concentration.

In order to further determine the correctness of the content of DZ-22 alloy, we calculated the alloy contents according to the method of [8] and the results of calculation are listed in Table 1. We can see that: (1) the concentration of  $\gamma'$ -phase is higher than 60 wt.% (the actual

result of analysis is 60.3 wt %). This is an important condition for obtaining good alloy properties; (2) The misfitting between the  $\gamma'$ - and  $\gamma$ -phases is small and meets the requirement of comparability of these two phases, and the structure is stable; (3) the average emptiness of electrons is lower than the critical value 2.52 which is the condition for forming  $\sigma$ -phase; therefore, usually no  $\sigma$ -phase will be formed (no  $\sigma$ -phase was found after a 3000-hr treatment at 870°C). According to the above analysis we can conclude that the content determined for the alloy is correct.

(238

Table 1. Alloy design computation result for DZ-22 alloy.

$\gamma'$ 相 总 量		$\sigma_{\gamma'}$	$\sigma_{\gamma}$	$\epsilon$	$\bar{NV}$
wt. %	at. %	$\times 10^{-10} \text{ m}$	$\times 10^{-10} \text{ m}$	%	
61.4	62.7	3.587	3.585	0.05	2.22

1-Total quantity of  $\gamma'$ -phase.

2. Selection of the drawing speed of shell mold.

In the process of directional solidification, the speed of shell mold is an important parameter for control of alloy structure and productivity. The results of the testing

have shown that: under the equipment conditions of this test, when the shell mold moves in a range of 4-10 mm/min, there is large influence on the orientations of crystals but no obvious influence on the room-temperature tension and 760°C stress-rupture properties. As a general rule, at low speed, the continuity of columnar crystals will become worse and there is a tendency toward the center. According to the results of the  $\omega/x$ -scanning method [7], the orientation deviation of crystals can be as high as 20° at the top of the testing plate, and 15° at the bottom. At the medium speed, the parallel of columnar crystals is good at both top and bottom parts of the testing plate, and the orientation deviation is within 10°. At the high speed, the columnar crystals at the top part of the testing plate have a tendency toward the edges, and the orientations of crystals can be 20° at the bottom part and 15° at the top part.



Table 2. Effect of shell-mold withdrawn rate on the orientation of columnar crystals (according to the  $\omega/x$ -scanning technology [7]).

试样编号	取样部位	铸型移动速度	柱晶最大偏角 <sup>4</sup> (°)		
			$x$	板宽方向 <sup>5</sup>	板厚方向 <sup>6</sup>
102	下部 <sup>(7)</sup>	慢速 <sup>(9)</sup>	0	6.5	8
			5	8	7.5
			10	2.5	2
			15	2	5
104	上部 <sup>(8)</sup>	慢速 <sup>(9)</sup>	0	2.5	4
			5	9.5	10
			10	7	9
			15	6	2
			20	11	—
202	下部 <sup>(7)</sup>	中速 <sup>(10)</sup>	0	6.5	6.5
			5	4	6.5
			10	—	5
			15	—	—
204	上部 <sup>(8)</sup>	中速 <sup>(10)</sup>	0	7	9
			5	4.5	7
			10	—	—
			15	—	—
302	下部 <sup>(7)</sup>	快速 <sup>(11)</sup>	0	8	9
			5	9.5	6.5
			10	6	4
			15	6	4
			20	8.5	8.5
304	上部 <sup>(8)</sup>	快速 <sup>(11)</sup>	0	3	6
			5	6	5
			10	5.5	4.5
			15	—	—

1-sample number; 2-location of sampling; 3-speed of mold; 4-maximum deviation of crystals; 5-in the width direction of the plate; 6- in the thickness direction of plate; 7-bottom part; 8-top part; 9-low speed; 10-medium speed; 11-high speed.

(23)

The difference of the deviation of crystal orientation caused by different moving speeds of shell mold is related to the distribution of the temperature field at the

solidification boundaries of the alloy. When the shell mold moves at a suitable speed, the boundary of solidification will be close to the radiant plate and thus the transversal radiation will not form a large transversal temperature gradient. Therefore the temperature field at the solidification boundary is uniform and within a plane, and the orientation deviation of crystalline growth will be the minimum. Otherwise, when the speed of the mold is too high or too low, the position of the solidification boundary will be above or below the radiant plate. Therefore the temperature field will not be uniform due to the transversal radiation. Therefore, it will be in a form of divergence or convergence shape and the orientation deviation of crystal growth will become large.

### 3. The influence of heat treatment.

In the microscopic structures of DZ-22 alloy, there are 13 vol.% cocrystal  $\gamma'$ - and many large size new  $\gamma'$ -phases. There is a large quantity of crystal branches formed in the alloy.

During the solid solution treatment, because of the strong diffusion of alloy elements, these cocrystal  $\gamma'$ -phases and new formed  $\gamma'$ -phases dissolve gradually into the matrix and the formation of crystal branches is reduced. Along with the increase of temperature, the diffusion of elements

is accelerated and the dissolving process becomes rapid. According to the results of testing, the thick  $\gamma'$  phase by and large is completely remelted at 1240°C the co-crystal  $\gamma'$  phase dissolves fully at 1250°C. In the afterwards cooling process fine  $\gamma'$ -phase ( $<0.5 \mu\text{m}$ ) will be formed and will distribute non-uniformly in the matrix. The distribution of the alloy elements will be more uniform. All these will help to improve the high-temperature properties. As shown in Fig. 3, when the solid solution temperature is raised from 1205°C to 1220-1230°C, the stress-rupture lifetime will increased by 20-25% whereas the elongation will have a slight decrease.

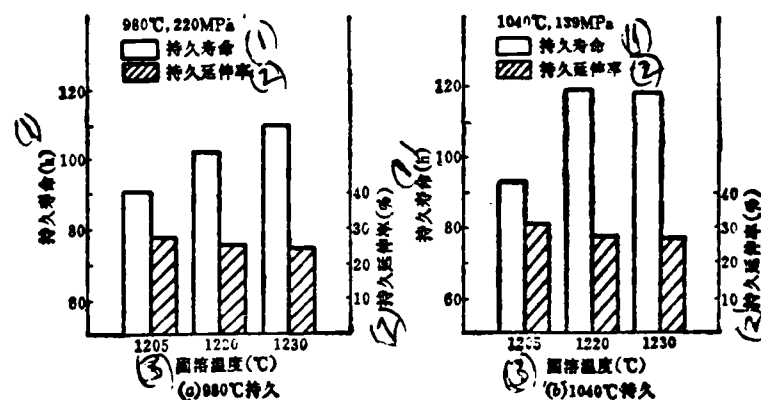


Fig. 3. Effect of solution treating temperature on the stress-rupture properties of DZ-22.

(a) 980°C stress-rupture lifetime; (b) 1040°C stress-rupture lifetime.

1-stress-rupture lifetime; 2-stress-rupture extension coefficient; 3-solid dissolving temperature.

Metallographic observation shows that after a 1205°C-solid-solution treatment, much of the  $\gamma'$ -phase does not follow its role. After a 1230°C solid solution treatment, the quantity of co-crystal  $\gamma'$ -phase decreases to about 8 vol.%; the coarse  $\gamma'$ -phase almost vanishes; and the fine  $\gamma'$ -phase greatly increases (about 40 vol.%). These lead to the improvement of stress-rupture properties. Therefore, in order to obtain good stress-rupture properties for DZ-22 alloy, the temperature of the solid-solution treatment can be increased to 1220-1230°C.

But further increasing the solid-solution temperatures will be limited by the incipient melting temperature. In the specified content region of DZ-22 alloy, the incipient melting temperature is about 1230-1240°C. The result of electron probing shows that the concentration of Hf in the incipient melting zone is about 9 times higher than in the zones between crystal branches, whereas the concentrations of Ni and W are low. These prove that the incipient melting is related to Hf in the alloy. Therefore, more than 0.5 vol.%  $\text{Ni}_3\text{Hf}$ -phase in DZ-22 alloy is the most important factor for the incipient melting.  $\text{Ni}_3\text{Hf}$  is a low-melting point phase, and its melting point measured by the Differential Thermal Analysis (DTA) is about 1135-1160°C [3]. This phase is formed due to the severe formation of

(24)

crystal branches at the end period of solidification and is mainly generated near the co-crystal  $\gamma'$ -phase or close to the co-crystal  $\gamma'$ -phase which is between the crystal branches. The incipient melting zone usually begins at these zones. Therefore, if the alloy is kept at a suitable temperature for some time until some  $\text{Ni}_3\text{Hf}$  dissolves, then the  $\text{Ni}_3\text{Hf}$ -phase will be reduced or even eliminated and the incipient melting temperature will be raised. The results of testing show that by using a 2-hr  $1150^\circ\text{C}$  followed by an 8-hr  $1220^\circ\text{C}$  pre-treatment, or by an 8-hr  $1150^\circ\text{C}$  pre-treatment according to [8], the initial melting temperature of the alloy can be raised to  $1260\text{--}1270^\circ\text{C}$ .

Table 3. Raised incipient melting temperature of alloy by pretreatment

处 理 制 度	初 始 情 况
$1240^\circ\text{C}$ 2h W.C	有 (3)
$1150^\circ\text{C}$ 2h + $1220^\circ\text{C}$ 8h + $1240^\circ\text{C}$ 2h W.C	无 (4)
$1150^\circ\text{C}$ 2h + $1220^\circ\text{C}$ 8h + $1250^\circ\text{C}$ 2h W.C	无 (4)
$1150^\circ\text{C}$ 2h + $1220^\circ\text{C}$ 8h + $1260^\circ\text{C}$ 2h W.C	很轻微 (5)

1-treatment method; 2-incipient melting; 3-yes; 4-no; 5-slightly.

#### 4. Stress-rupture and creep properties.

DZ-22 has good medium- and high-temperature properties. Its 760°C- and 1040°C-100-hr strengths are 804 MPa and 139 MPa respectively. Fig. 4 shows the Larson-Miller curve of this alloy. Table 4 lists a comparison of stress-rupture properties of DZ-22 and PWA1422 alloys. It can be seen that the transversal and longitudinal stress-rupture properties are about equal, but the lifetime of the longitudinal stress-rupture of DZ-22 is much high than PWA1422 alloy.

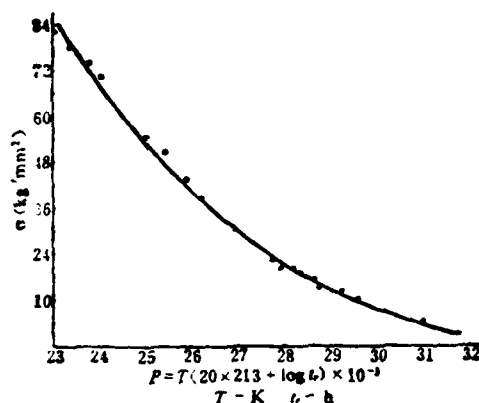


Fig. 4. Larson-Miller curve of DZ-22 alloy

Table 4. The stress-rupture properties of DZ-22 as compared with PWA1422 [3]

取 向	合金	760°C			850°C			980°C		
		$\sigma$ MPa	$\tau$ h	$\delta$ %	$\sigma$ MPa	$\tau$ h	$\delta$ %	$\sigma$ MPa	$\tau$ h	$\delta$ %
3 橫向	DZ-22	689	138~264	3.2~6.4	417	326~362	5.6~7.8	176	176~192	6.0~13.2
	PWA1422	689	170	5.3	(870°C) 412	120	9.8	163	125	7.6
4 纵向	DZ-22	689	1038~1245	18.6~18.8	529	104~134	17.6~23.6	220	73~93	20~26
	PWA1422	689	700	—	—	—	—	220	75	—

1-orientation of test; 2-alloy; 3-transverse; 4-longitude.

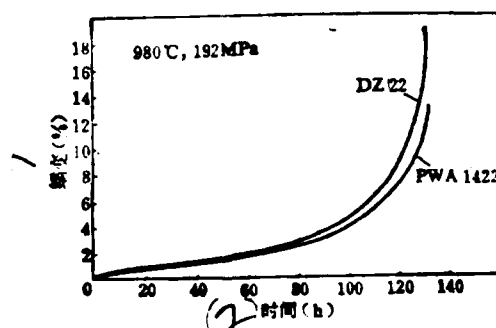


Fig. 5. A creep curve of DZ-22 alloy as compared with PWA1422 alloy [10]

1-creep; 2-time.

The creep at different temperatures and different stresses of DZ-22 alloy were measured. The creep strength; that is, the stress at a residual deformation of 0.2% in 100 hours, is 82 MPa at 980°C, and 534MPa at 760°C. Fig. 5 shows the creep curve of DZ-22 alloy at 980°C and is compared with the curve of PWA1422 alloy [10]. It can be seen that these two curves are very similar.

#### CONCLUSIONS

1. DZ-22 has good medium temperature and high temperature properties. It can be used as turbine blade material for aircraft engines.
2. Correct contents of Hf and C in DZ-22 alloy were determined by a series of testing, and it was determined that no Zr need be added for this alloy.
3. The drawing speed of shell mold has obvious influence on the crystal orientation. Under the equipment conditions of this study, a medium speed can lead to an optimization of the material structure and properties.
4. Increasing the temperature of solid solution can improve stress-rupture properties at 980°C and 1040°C. Before the treatment of solid dissolving, a 1150°C pretreatment can raise the initial melting temperature.



## ACKNOWLEDGEMENT

Mr Long Hongjian, Ying Kejin, and Sou Shenghong have involved in this work. We obtained assistance in testing by Zhang Gouhuan, Dong Yuzhou, Sun Shouzheng, Chen Shengzhe, Guan Wenpiao, and Liu Yirou. The authors would like to thank all of them for their help.

## REFERENCES

- [1] Duhl, D. N., USDP 3711337, Oct. (1973).
- [2] Pratt and Whitney Aircraft, TM Specification PWA1422F  
Nov. 1972.
- [3] Duhl, D. N., et al., J. Metals, July, (1971), P. 38.
- [4] Wang Luobao, Chen Rongzhang, Wang Yuping, The  
Production and application of Less Common Metals, Proc.  
Symp. 8-11 Nov. Hangzhou, China, Book II, Paper 41.
- [5] Lashko, N.F. Casting technology, 1972, No. 2, p. 35.
- [6] (In Japanese)
- [7] Zhang Guohuan and Wang Qinlei, Aeronautical materials  
(a Chinese journal), Vol. 3, 1983, No. 2, p. 47.
- [8] Zheng Yunrong, Cai Yuling, and Wang Luobao, Journal of  
Metals (a Chinese Journal), Vol. 19, 1983, P.A190.
- [9] Harris, K., EP0032812, July, 1981.
- [10] Stewart, D. C. , et al., AD-A077527, July, 1979.

PLASTIC DEFORMATION ANISOTROPY OF LC4-ALUMINUM-ALLOY  
PLATES

Li Huanxi and Chen Changqi

Beijing Institute of Aeronautics and Astronautics

(243)

ABSTRACT

Plastic deformation of thick LC4-aluminum-alloy (Al-Zn-Mg-Cu) plates has an obvious anisotropy. A method for expression this anisotropy, and its changes with the longitudinal strain and heat-treatment status, is proposed. Furthermore, observation was made on the fractures of the samples.

1. INTRODUCTION

The texture of plates makes mechanical characteristics of metals and alloys different in different directions, but we have not studied how thick plates of some industrial alloys, which are precipitating-hardened and thick, are plastically deformed in an anisotropy mode, and how heat treatment affects this anisotropy. In addition to that, as high-strength aluminum alloys usually can be cut off more

-----  
This paper was received Nov. 22, 1984.

easily by shearing forces, they manifest low stress-rupture toughnesses. Therefore it is necessary to study how heat treatment affects plastic deformation and how plastic deformation affects the mode of the final cracking.

In this paper we first suggest a method for expression and measurement of the plastic-deformation anisotropy; then the results of measurement and analysis of different types of LC4-aluminum-alloy plate are reported.

## 2. EXPRESSION AND MEASUREMENT OF PLASTIC DEFORMATION ANISOTROPY

According to the conventional concept, we define the direction of rolling, the direction of width, and the thickness, of a plate, as longitude, transverse, and short transverse; and they are represented by L, T, and S, respectively.

In this paper, an uniaxial-tensile specimen, which was cut along the longitudinal direction of a thick plate, was used. The true plastic strain along the longitudinal direction of the plate is defined as:

$$\epsilon_L = \ln(A_0/A) \quad (1)$$

where  $A_0$  and  $A$  denote the initial and instantaneous areas of the specimen's cross-section. The true plastic strains in the short-transversal and transversal directions are defined as:

$$\epsilon_s = \ln(d_0/d_s), \quad \epsilon_T = \ln(d_0/d_T) \quad (2)$$

where  $d_0$  denotes the initial diameter of the specimen and  $d_s$  and  $d_T$  denote the initial and instant diameters of the specimen, respectively. Therefore, the ratio of  $\epsilon_s$  to  $\epsilon_T$ ,

$$R_{s,T} = \epsilon_s / \epsilon_T \quad (3)$$

specifies the anisotropy of the plastic deformation in the short transverse and transverse directions of a thick plate. Obviously, for isotropy materials, because of

$$\epsilon_s = \epsilon_T = \frac{1}{2} \epsilon_L \quad (4)$$

Therefore,

$$R_{s,T} = 1 \quad (5)$$

but for anisotropy materials, (4) is no longer valid,

$$R_{s/T} \neq 1 \quad (6)$$

Therefore, the bigger the difference between  $R_{s/T}$  and 1, the more serious the plastic deformation anisotropy will be.

Now as long as we know the initial diameter and any instant  $d_s$  and  $d_T$  of the specimen rod, according to (1) and (2), we can calculate the corresponding value  $R_{s/T}$  at that time.

### 3. THE CONDITIONS AND RESULTS OF THE EXPERIMENT

In this study, we used hot-rolled LC4-aluminum-alloy plate of 20 mm thick. Its chemical composition is listed in Table 1. Its optical metallographic structure at the quenched condition is shown in Fig. 1. From Fig. 1, we can see that crystal grains at the rolling direction were pulled longer, and the doping distribution of the impurities was also obviously oriented.

Table 1. Chemical composition of LC4 alloy.

元素	Zn	Mg	Cu	Cr	Mn	Fe	Si
%(重量) 2	5.50	2.50	1.79	0.18	0.34	0.36	0.23

1 - element; 2 - weight.

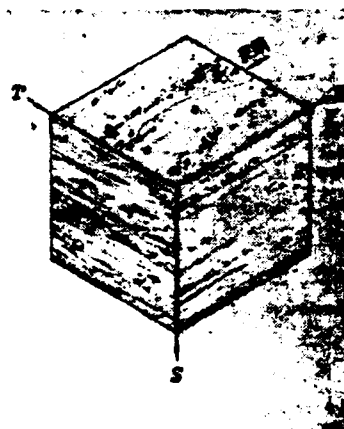


Fig. 1. Microstructure under optical microscope. (X 100)

An uniaxial-tensile rod with a diameter of 15.2 mm was used as the specimen. After it was heated by nitrate-solid

melting and water quenching, it was artificially aged to the status of under-peak aged, peak aged, and over-peak aged. The details are shown in Table 2. The tensile experiment was done in an INSTRON-1255 fluid-dynamic-feeding test machine and its clamping-head speed is 1 mm/min. By means of projection we can measure the initial and instant diameters of the cylinder with an error of 0.01 mm. After it was , loaded to a certain magnitude, the machine was shut down and then the load was released; then the corresponding  $d_s$  and  $d_T$  at that load were measured.

Table 3 is the room-temperature tensile properties of LC4 alloy at different conditions. Fig. 2 is the macroscopic fracture surfaces of the uniaxial tensile specimens at different conditions. Both of the underpeak-aged and peak-aged specimens look like they were fractured by a shearing cutting, and those overpeak-aged specimens have cup-cone-like fractures They are basically the same as those of other Al-Zn-Mg-Cu alloys [3,4]. The microscope feature of fractures of shearing cutting is "shearing-hole type", and they are still ductile fractures (Fig. 3). Fig. 4 shows the correlations between strain- and uniaxial-tension for specimens at different conditions. We can see that in all conditions the specimen's  $\epsilon_s$  is always larger than  $\epsilon_T$  during uniaxial tension.

Table 2. Processing of heat treatment.

状态 1	标号 2	固溶加热 3	淬火 4	时效 5
欠时效 (6)	U	470°C 30 分钟 (9)	室温水 (10)	120°C 2 小时 (11)
峰值时效 (7)	P			120°C 24 小时 (11)
过时效 (8)	O			120°C 24 小时 + 170°C 24 小时

1-Conditions; 2-Marks; 3-Solid-melting heating; 4-Quenching material; 5-Aging status; 6-underpeak aged; 7-peak aged; 8-overpeak aged; 9-minutes; 10-room-temperature water; 11-hours.

Table 3. Tensile properties of LC4 alloy.

状态 1	$\sigma_{0.2}$ , MPa	$\sigma_b$ , MPa	$\delta$ , %	$\sigma_f$ , MPa	$\epsilon_f$
U	426	556	19.2	674	0.19
P	532	612	18.3	730	0.18
O	383	490	14.8	605	0.33

1-conditions.



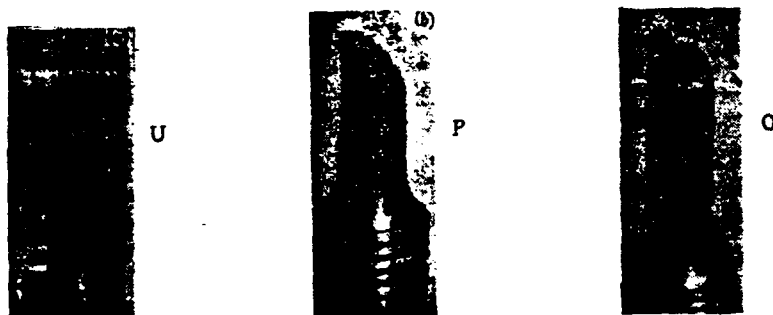


Fig. 2 Macroscopic fracture surfaces of uniaxial tensile specimens.



Fig. 3 Scanning electron micrograph of peak-aged specimen.

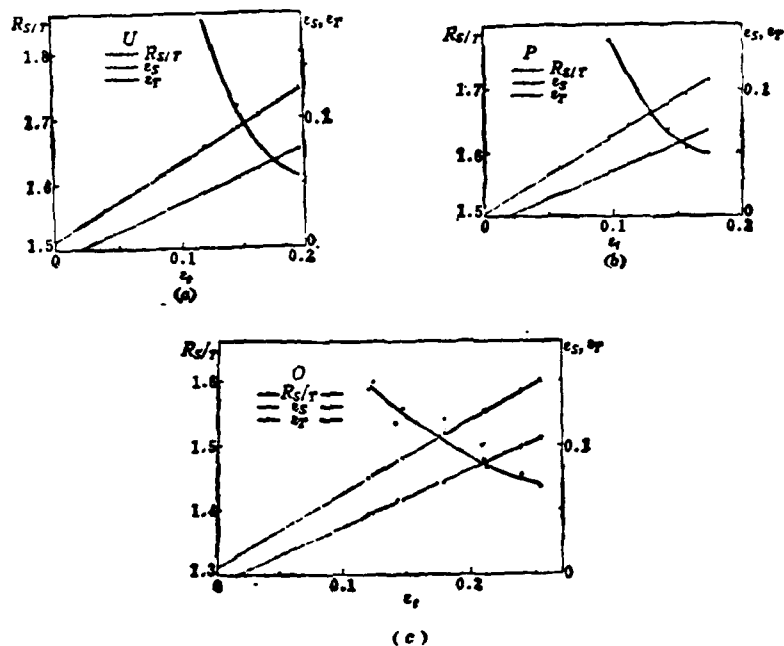


Fig. 4 Strain correlations of different heat-treated specimens

#### 4. DISCUSSION

(1) The correlations between the strains, and the plastic deformation anisotropy.

According to Fig. 4, we can see that the true strains in the transversal and short-transversal directions of tensile specimens are linearly increasing with the increase of the true strain in the longitudinal direction. The relations can be described as follows :

$$\varepsilon_s = k_s \varepsilon_L + b_s, \quad \varepsilon_T = k_T \varepsilon_L + b_T \quad (7)$$

where  $k_s$ ,  $b_s$ ,  $k_T$  and  $b_T$  are constants which can be measured by experiments. Table 4 is a list of all these constants measured in this experiment under different conditions. Obviously these constants satisfy the following formula:

$$k_s > k_T > 0, k_s + k_T = 1, b_s + b_T = 0 \quad (8)$$

The assumption of constant macroscopic volume under plastic deformation is still valid.

Table 4. Constants in strain correlations of LC4-alloy tensile specimens.

(1) 状 态	$k_s$	$b_s$	$k_T$	$b_T$	$ds/de_T$
$U$	0.59	0.01	0.41	-0.01	1.44
$P$	0.58	0.01	0.42	-0.01	1.38
$O$	0.56	0.01	0.44	-0.01	1.27

1-conditions.

In addition, we also can see that not only  $\epsilon_s$  and  $\epsilon_T$  increase when  $\epsilon_L$  increases, but also the speed of increasing is very different:  $k_s > 1/2$ ,  $k_T < 1/2$ . It follows that the

plate has an upward-preferred plastic deformation, with a magnitude of  $(\epsilon_s - \epsilon_T)$ , in the direction of short transverse. As shown in Fig. 5, solid lines indicate the LC4-alloy plates which are anisotropic, and the dashed lines indicates the materials which are isotropic. The shadow lines indicate  $(\epsilon_s - \epsilon_T)$ .

(247

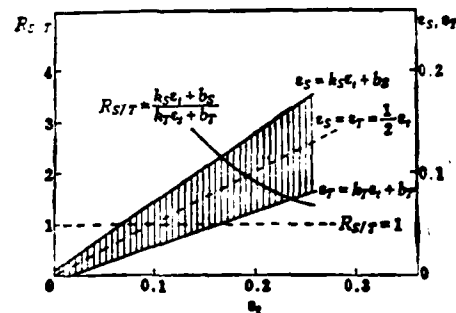


Fig. 5. Schematic diagrams of strain correlation.

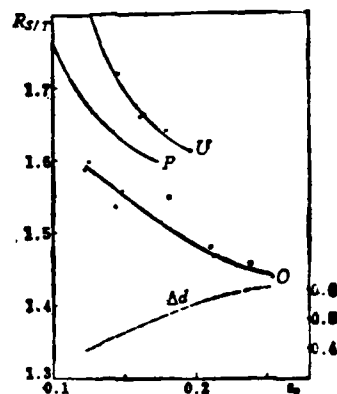


Fig. 6.  $R_s/T$  vs  $\epsilon_L$  relationship of different heat-treated specimens.

As mentioned before,  $R_{s/r}$  can describe the plastic deformation anisotropy of plates. But for LC4 alloys,  $\epsilon_s$  and  $\epsilon_T$  change linearly with  $\epsilon_L$ , therefore the ratio of increase of the two true strains

$$d\epsilon_s/d\epsilon_T = k_s/k_T = \text{常数} \quad (9)$$

describing the plastic deformation is more suitable. This is because:

$$R_{s/r} = (k_s\epsilon_L + b_s)/(k_T\epsilon_L + b_T) \quad (10)$$

decreases when  $\epsilon_L$  increases, while  $d\epsilon_s/d\epsilon_T$  does not

correlate with  $\varepsilon_L$ . Under certain conditions, the alloy has a special value of  $d\varepsilon_s/d\varepsilon_T$ . If  $d\varepsilon_s/d\varepsilon_T = 1$ , it indicates the deformation is isotropic; if  $d\varepsilon_s/d\varepsilon_T \neq 1$ , it indicates the deformation is anisotropic. But as for LC4-alloy plates, in all conditions,  $d\varepsilon_s/d\varepsilon_T$  is always larger than 1, therefore it shows an obvious plastic-deformation anisotropy under all three conditions.

(2) The anisotropy of plastic deformation is correlated to the condition of heat treatment

From Table 4, we know  $d\varepsilon_s/d\varepsilon_T$  reaches the maximum in under-peak-aged condition, medium in peak-aged condition, and the minimum in over-peak-aged condition. That is: the anisotropy of plastic deformation is the most obvious for under-peak-aged condition and the least obvious for the over-peak-aged condition. By comparing the  $R_s/T \sim \varepsilon_L$  curves of these three conditions (figure 6), we can also see this correlation. In Fig. 6, the dashed line is the  $\Delta d \sim \varepsilon_L$  curve of the over-peak-aged condition of the rod; with  $\Delta d = d_T - d_s$  and the unit is mm.

Thus we conclude that not only the crystal and the fibric structure of the plate material can lead to anisotropy of plastic deformation [5], but also the microstructure, decided by the property, size, orientation, and distribution, of the deposited particles, will influence

the anisotropic characteristics of thick plates of LC4 alloy. Because whether the material is in under-peak-, peak-, or over-peak-aged condition, the crystal structure and fibric structure are almost the same, and the main difference is that the micro-structure has undergone different heat treatments and therefore the strengthening mechanisms are different. Fig. 7 is the testing results of the crystal structure of a thick plate of LC4-alloy, by using the small-angle X-ray method. The results show that the thick plate of LC4 alloy after hot rolling has two type- $(110) [\bar{1}12]$  and  $(112) [\bar{1}\bar{1}1]$ -plate structures. The orientation preferences of these two types are very obvious for both. The aging process after quenching has almost no influence on both types of crystal structures.

(3) The manner of macroscopic fracture is correlated (248 with the plastic-deformation anisotropy.

The LC4-plate after under-peak aging and peak aging has larger plastic-deformation anisotropy, and finally it will be sheared off along the direction which is at  $45^\circ$  degrees with both the longitudinal and short transverse of the plate. But the over-peak-aged LC4-plate has very small plastic deformation anisotropy, and finally it will be partially fractured in a cup-cone shape, where the bottom looks like an ellipse and the short axis of the ellipse is just on the short-transversal direction of the plate. This

manifests that the manner of macroscopic fracture of a uniaxial- tensile specimen is correlated with the upward-preferred plastic deformation before fracturing, of the plate. Therefore, the larger the plastic deformation anisotropy, the easier the uniaxial tensile specimen will be sheared off.

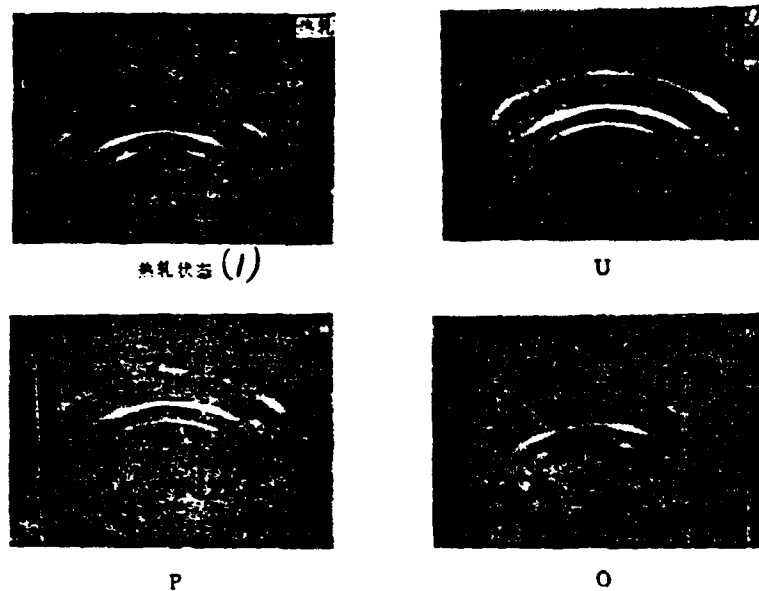


Fig. 7 X-ray photographs of different heat-treated LC4 aluminum alloy plates.

1 - hot-rolling condition.



## 5. CONCLUSIONS

The longitudinal-tensile cylinder specimens of thick LC4- aluminum-alloy plates are under quenched and aged conditions. Its true strain in the short-transversal direction is larger than that in the direction of transverse, but both of them are linearly increased with the positive strain in the longitudinal direction. Besides, the ratio of the increase can represent the plastic-deformation anisotropy. The reducing of aging degree will lead to more anisotropy and more sensitivity of uniaxial-tensile fracture.

## ACKNOWLEDGMENT

Thanks to Comrade Guo Taiji of Beijing Institute of Electric and Mechanical Engineering; thanks to Zhou Boqun and Zhen Yingyi of Department Seven of Beijing Institute of Aeronautics and Astronautics for their help with the experiment.

## REFERENCES

- [1] Chen, C. Q. and Knott, J. F. Effects of dispersoid particles on toughness of high strength aluminum alloy,

- Met. Sci. (1981), 15, 357.
- [2] King, J. E., You, C. P., and Knott, J. F., Serrated yielding and the localized shear failure mode in aluminum alloys, *Acta Metal.*, (1981), 29, 1553.
- [3] Chen, C. Q., On shear failure in round bar tensile tests of Al-Zn-Mg-Cu alloys, *Proc. ICP Int. Sym. on Fracture Mechanics (Beijing)*, (1983), Beijing, Science Press, 871.
- [4] Korbel, A., Raghunathan, V. S., Teirlinck, D., Spitzig, W., Richmond, O. and Embury, J. D., A structural study of the influence of pressure on shear band formation, *Acta Metall.*, (1984), 29, 241.
- [5] Dieter, Jr. George e., *Mechanical Metallurgy*, McGraw-Hill, New york, (1961), 269.

(249

RELATIONSHIP BETWEEN SHOT PEENING SURFACE  
STRAIN LAYER AND FATIGUE STRENGTH OF  
HIGH-STRENGTH ALUMINUM ALLOYS

WANG Renzhi LI Xiangbin

(Beijing Institute of Aeronautical Materials)

WU Hen

(Shenyang Electromechanical Academy)

ABSTRACT

The relation of the fatigue behaviour to the residual stress and plastically deformed microstructure in the surface strain layer of high-strength aluminium alloys is investigated. It is shown that the stress and microstructure strengthenings are two factors improving the fatigue behaviour, moreover, the microstructure strengthening factor plays a main role in the improvement of the fatigue behaviour in the high alternating stress region of S-N curve, but the main contribution to the fatigue behaviour near the fatigue limit is made by the stress strengthening factor. There exists an optimum residual stress field induced by shot peening for a high-strength aluminium alloy, and the maximum compressive residual stress in the field is  $(\sigma_r)_{op} \approx \sigma_s - \sigma_e$ .

## 1. Forward

The industrial technique of strengthening through shot peening is an effective technique which is used to increase the resistance of metal parts to fatigue and stress corrosion cracking. Because this technique has advantages which cannot be matched by other surface strengthening techniques in recent years, both inside and outside China, and, particularly in the aviation industry, it has been given rapid development (1-3).

Research on the relationship of shot peening to increase strength and the influence it has on fatigue strength in aluminum alloys (4-6) has pointed out that, although shot peening is capable of improving the fatigue strength of high stress areas of the S-N fatigue curve, it has, however, no clear effects near the fatigue strength limit. Besides this, in recent years, although there has been a good deal of research done on the machine processes of increasing strength through shot peening (7-9), there are, however, still many questions which are awaiting a more thorough discussion. This article considers the experimental research on the problems mentioned above, compressive 10 M, and presents optimum shot peening residual stress fields.

## 2. Materials and Experimental Methods

Making use of LC9(Al-Zn-Mg-Cu) series high strength aluminum alloy rods, we processed them into a 9mm diameter rotating curve fatigue sample. After these test samples have gone through quenching and aging processing, their mechanical properties are as follows: tensile strength  $\sigma_b = 490\text{MPa}$ , yield strength  $\sigma_{0.2} = 410\text{MPa}$ , elongation  $\delta = 11.5\%$ .

In order to study the textural structure and residual stress within the surface strain layer as well as the effect of surface finish on fatigue properties, we prepared specimens of five types of surface states. The layer depths of the plastic deformation structures on these surfaces as well as their residual compressive stresses are presented in Table 1.

Table 1 The surface state of different specimens

No	试样表面状态 (1)	表面塑性变形层深度 $\mu\text{m}$ (5)	表面残余应力 MPa (6)	残余应力分布深度 $\mu\text{m}$ (7)
A	(2) 磨加工 (G) + 电抛光 (EP)	0	0	0
B	G	$\sim 30$	-150	$\sim 20$
C	G + 喷丸 (SP) (3)	$\sim 80$	-158	$\sim 450$
D	G + SP + EP (去层 $\sim 50\mu\text{m}$ ) (4)	$\sim 45$	-250	$\sim 400$
E	G + SP + EP (去层 $\sim 80\mu\text{m}$ ) (4)	$\leq 10$	-220	$\sim 370$

Key: 1) Specimen Surface State; 2) Grinding (G) + Electro-polishing (EP; 3) Shot Peening; 4) Disposal Layer; 5) Depth of Surface Plastic Deformation Layer; 6) Residual Surface Stress; 7) Depth of Residual Stress Distribution.

In Model 2903 X-ray stress measurement instrument, we made use of Cr-K $\alpha$  radiation and from the (222) spectrum line measurements calculations were made of residual stresses and their distribution across layer depths. Specimens fatigue fractures and metallic thin membrane separations were observed on JSM-35 Model scanning electron microscope and JEM 200 A Model transmission electron microscope.

### 3. Experimental Results and Discussion

After shot peening, the aluminum alloy surface produces a cyclic strain layer (7), and within this layer appear the following two types of transformations: residual compressive formation stress and structurally occurring plastic deformation. Under certain conditions, these transformations are advantageous factors in improving the fatigue characteristics of materials. We will take them and call them respectively "stress strengthening" and "structural strengthening". However, in another aspect, shot peening causes surfaces to form pits, lowering the fatigue characteristics of materials. Below, we will discuss, in turn, the various types of factors which influence the fatigue characteristics of materials.

## 1. The Influence of Residual Stress on Fatigue Strength

The distribution of residual compressive stresses caused by shot peening and their distribution across layer depths are shown in Figure 1. Residual compressive stress layer depths are approximately  $450\mu\text{m}$ .

LC9 aluminum alloy system macrocrystalline materials only require the use of X-ray radiation in the periodic oscillation method (10), and it is possible to obtain continuous (222) spectrum line wave forms. However, when it comes to the plastic deformation structures of surface layers, if one uses fixed X-ray radiation techniques, it is possible to get even better continuous spectrum wave forms. On the basis of (222) spectra done at differing depths, there is a variation from continuity to discontinuity. As well as this, on the basis of observation of the appearance of slip bands within shot peen strain layers (Figure 2), it was consequently possible to accurately estimate the depth of the shot peening surface deformation structures to be  $80\mu\text{m}$ . In order to promote the functions of area organization and stress strengthening, we took the shop peening specimen and electrolytically removed  $80\mu\text{m}$  of the layer depth. On the foundation of the E group specimens obtained, it was possible to observe that there was only a single specimen in which there was stress strengthening. In D group specimens (surface deformation layer depths of approximately  $45\mu\text{m}$ ) besides those showing stress strengthening, there were also those which showed the results of partial organizational strengthening. Along with this, A group specimens showed a lack of both stress strengthening and organizational strengthening. The S-N rotary fatigue curves for the various groups of specimens are shown in Figure 3.

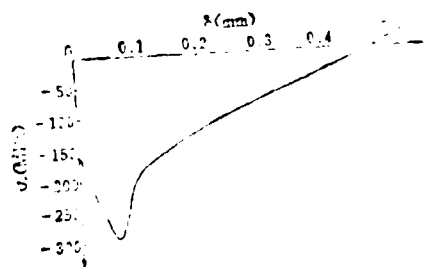


Fig 1 Residual stress distribution in the surface layer



Fig 2 Slip band in the surface strain layer  
500  $\mu$

Under the influence of the addition of alternating outside stresses, the surface layer residual stresses will produce some relaxation. It is possible to divide the overall relaxation into the two types: static loading relaxation and dynamic loading relaxation. Static loading relaxation is a form appearing within 1-3 cycles. In the aluminum alloy, it depends on the material's bending strength  $\sigma_s$  and its alternate loading compressive stress value  $\sigma_a$ . The results of measurements of stress distribution both before and after fatigue testing with shot peening specimens clearly show that there is, between the residual stress force after relaxation  $\sigma'_r$  and  $\sigma_r, \sigma_a$ , the relationship given below:

$$\sigma'_r = \sigma_r - \sigma_a$$

After the occurrence of static load relaxation, the distribution of the combined stresses along the layer depth  $\delta$  of D group specimens are separately shown in Figure 4 (E group specimens also possess /2 the same trends in changes as those shown in Figure 4). Surface layer compressive stresses follow increases in the externally applied  $\sigma_a$ , and then, gradually fall. Subsequently, the surface layer tensile strength level gradually increases. If one takes as a basis the A group specimen fatigue limits  $(\sigma_{-1})_A$  it is only when the stress value of the surface layer at any depth is higher than  $(\sigma_{-1})_A$ , that it is possible to see the rudimentary formation of fatigue cracks. Therefore, the area enclosed between any curve  $(\sigma_r - \sigma'_r) - \delta$  and  $(\sigma_{-1})_A$  level line (in reality, the volume enclosed between the curve and the plane), is the position of the nucleus of the formation of fatigue fractures in stress strengthened samples. If we assume here that the area enclosed between the point of maximum tensile strength M on the curve and the first intersection point P of the level line and the curve is the area with the greatest probability of fatigue formations, we can let F represent it (the slanted line segment in Figure 4). Following the increase in the value of  $\sigma_a$ , not only does the value of F increase, but the point P moves toward the surface. This shows that the nucleation of fatigue fractures moves gradually from secondary surfaces

toward the main surface. If, at the same time, we consider the values of the alternating stresses added when fatigue fractures start to nucleate on the surface, the positions of the P and M points of D and E group specimens for various values of  $\sigma_a$  are shown in Figure 5 and Figure 6. Original distances of fatigue from the surface as obtained from measurements of fatigue breaks in specimens are also shown in the figures, and the experimental points fall, for the most part, within the F values. When the compound stress  $(\sigma_1)_A$  on the surface of the specimen changes to a tensile stress, fractures increase their nucleation on the surface.

Because of this, the layer removal from group D specimens /253 was more shallow than the layer removal in group E specimens  $(\sigma_1 + \sigma'_1)$ , and, after layer removal, the surface still has in it pits of approximately 0.1mm in diameter and a depth of 0.01mm (Figure 7(a)). The group E surface was relatively smoother (Figure 7(b)). The concentration of stresses caused by surface pits causes D samples to have an even greater residual stress static loading relaxation than that found in E specimens. Therefore, the alternating stresses on the surface of D specimens at the beginning of the rudimentary appearance of fatigue fractures are lower than those found in E specimens (Figure 5 and Figure 6). The former was approximately  $\sigma_1 = 250 \text{ MPa}$ , and the later was approximately  $\sigma_1 = 300 \text{ MPa}$ .

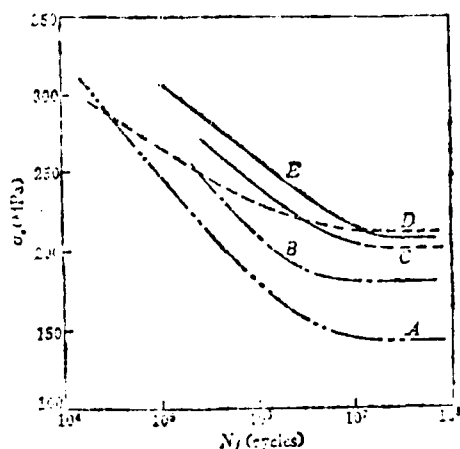


Fig. 3 Rotating bending fatigue S-N curves of five kinds of specimens

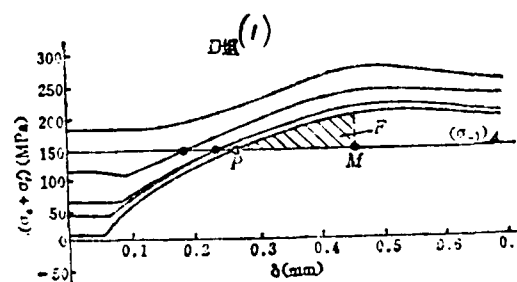


Fig. 4  $(\sigma_1 + \sigma'_1)/\sigma_0$  curves of D specimens

Key: 1) group.



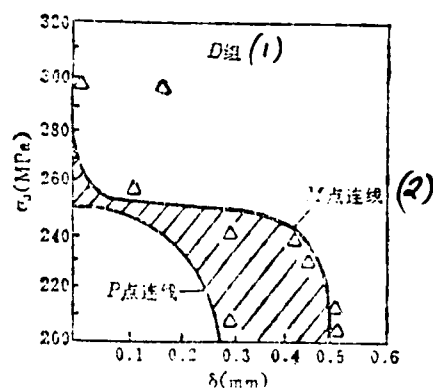


Fig. 5 Relationship between positions of point *P* and *M* and alternating stresses  $\sigma_a$  of *D* specimens

Key: 1) group; 2) point continuous curve.

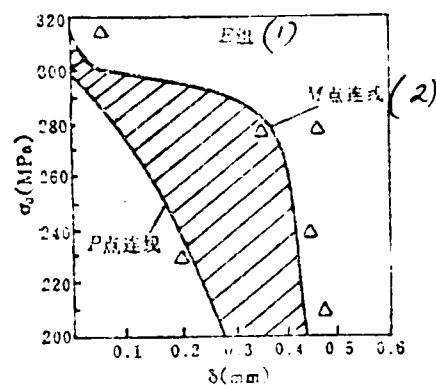


Fig. 6 Relationship between positions of point *P* and *M* and alternating stresses  $\sigma_a$  of *E* specimens

Key: 1) group; 2) point continuous curve.

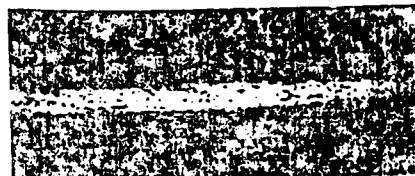
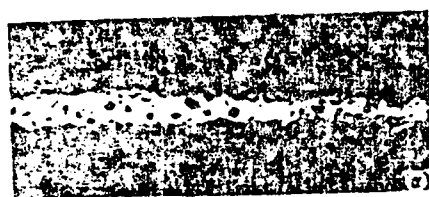


Fig. 7 The surface pitting features of *D*(a) and *E*(b) fatigue specimens 20×

The curves in Figure 4 show, in situations in which the externally applied value  $\sigma_a$  is lower than a certain numerical value or the surface value  $(\sigma_s + \sigma'_s)$  is the compressive stress, the *F* value stands on the secondary surface, and fatigue fractures nucleation takes place on the secondary surface. The restraining force of nucleation on the secondary surface is clearly higher than the restraining force of nucleation on the surface. Therefore, under similar conditions of  $\sigma_a$  specimens with stress strengthening have even higher fatigue strength than the group A specimens without strengthening (Figure 3 D).

## 2. The Influence of Deformation Structures Within Strain Layers on Fatigue Strength

Under the effect of the shot during the shot peening process, the surface layer metal gives rise to cyclic plastic deformation, which lead to large numbers of misplaced implantations. The results

of electron microscope observations indicate that, compared to the original undeformed structures, there have been formed, within strain layers, a high density of dislocated bubble-shaped structures. This high dislocation density surface layer is able to effectively block the crystalline bodies in the lower portion of the surface strain layer from surface slip under the effect of alternating stresses. Metallographic observations of the condition of surface slip during fatigue process in A and D group specimens indicate that A group specimens, under the conditions  $\sigma_a = 200 \text{ MPa}$ ,  $N = 3 \times 10^4$  the surface shows thick slip bands at spacings of approximately  $2.37 \mu\text{m}$ . Moreover, its distribution is extremely uneven (Figure 8(a)). However, shot peening specimens (surface removal layer depth only  $15 \mu\text{m}$ ), under the conditions described above, do not show slip bands. It is only after the alternating stresses have been raised to  $\sigma_a = 250 \text{ MPa}$ , and after going through  $N = 5.8 \times 10^6$  cycles, that one gets the appearance slip bands at spacings of approximately  $1.48 \mu\text{m}$ .

Moreover, they are distributed relatively uniformly over the surface of the specimen (Figure 8(b)). From this we can see that, within the shot peening strain layers, there are deformation structures with a high dislocation density. On the one hand this can cause

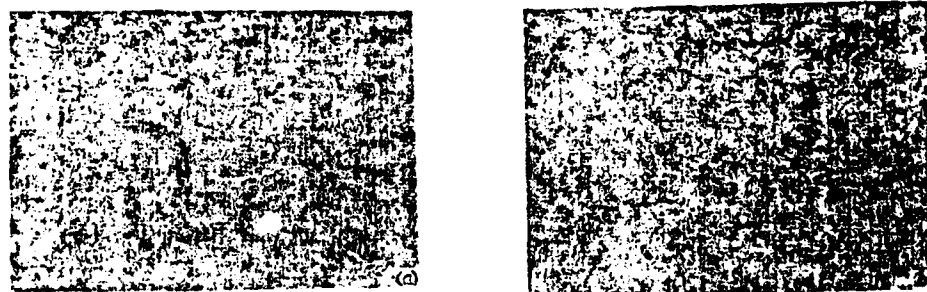


Fig.8 Slip band features formed in the fatigue process. 500X  
(a) A specimen; (b) D specimen

the internal slip to be blocked within the strain layer. On the other hand, it can cause the whole slip to be broken up, which, in turn, causes to be formed on the surface slip bands with a

/254

distribution which is both fine and even. The special features noted above are capable of raising the ability of materials to resist the formation on their surfaces of breaches for the formation of crystalline bodies, of extending fatigue fracture nucleation life, as well as causing the resistance of materials to fatigue fractures to be raised.

Surface grinding and shot peening are similar. Both cause materials to produce surface transformations of organization and residual compressive stresses. From Table 1 one can see that the residual stress layers of group B specimens are extremely thin (approximately  $20\mu\text{m}$ ). In addition to this, the depth of deformation structure is in line with that for group D specimens. Therefore, group B specimens can be seen as being simple specimens which have a single type of organizational strengthening. If we compare the S-N curves for specimens from groups A and B (Figure 3), one can see the results of the influence of the fatigue characteristics of simple organizational strengthening.

### 3. The Influence of Surface Roughness on Fatigue Strength

Let us compare the fatigue limits of specimens from groups C, D, and E as shown in Figure 3, that is,  $(\sigma_{-1})_D \approx (\sigma_{-1})_E > (\sigma_{-1})_C$ . The surface roughness of C specimens is lower than the roughness of D and E specimens. In reality, the surface pits on C specimens are simply a set of small gaps, and the stress concentrations which are formed give the residual compressive stresses on its surface an even greater amplitude of relaxation. This causes the F area to move toward the surface. As a result of this, the movement leads to a lowering of the fatigue limits of C specimens. However, in the high stress area of the S-N curve, although C group specimen surface residual compressive stresses give rise to relaxation, even though the deformation structure of surface layers have the function of strengthening stability, they still act so that their fatigue strength is even greater than that of specimens from group A and group B (only organizational strengthening) and group D (stress strengthening

with partial organizational strengthening). However, the surface roughness of C specimens is far below that of E specimens (only stress strengthening). In the high stress area of the S-N curve, the latter has higher fatigue strength than the former. This illustrates the fact that, when the factors influencing surface strengthening are basically the same, surface roughness contributes in an important way to fatigue strength.

#### 4. A Qualitative Evaluation of the Influence on Fatigue Limits of Organizational Strengthening, Stress Strengthening, and Surface Finish

If one compares the five S-N curves in Figure 3 in terms of their fatigue limits ( $N = 2 \times 10^7$ ), one can see the influences of the various factors.

##### (1) The Contribution of Organizational Strengthening

$$(\Delta\sigma_{-1})_H = (\sigma_{-1})_B - (\sigma_{-1})_A = 180 - 140 = 40 \text{ MPa}$$

##### (2) The Contribution of Stress Strengthening

$$(\Delta\sigma_{-1})_T = (\sigma_{-1})_E - (\sigma_{-1})_A = 210 - 140 = 70 \text{ MPa}$$

##### (3) The Contribution of Combined Organizational and Stress Strengthening

$$(\Delta\sigma_{-1})_H + (\Delta\sigma_{-1})_T = 40 + 70 = 110 \text{ MPa}$$

##### (4) Losses Caused in the Fatigue Limit by Drops in Surface Roughness

$$[(\sigma_{-1})_A + (\Delta\sigma_{-1})_H + (\Delta\sigma_{-1})_T] - (\sigma_{-1})_C = 250 - 200 = 50 \text{ MPa}$$

In the vicinity of the fatigue limits of materials, the contribution of stress strengthening is the largest. The next largest is organizational strengthening. Moreover, shot peening leads to a drop in the surface finish, which in turn lowers the fatigue

limits of materials. Therefore, under conditions when it is appropriate to preserve stress strengthening and organizational strengthening, the use of grinding techniques or other machining techniques raises the surface roughness of shot peening specimens (spare parts).

## 5. Optimum Residual Compressive Stress Fields.

What are called residual compressive stress fields primarily indicate the peak values of residual compressive stresses and their depths of distribution. The general rules for residual stress relaxation indicate (11,12) that, in areas of lowered stress in the vicinity of fatigue limits, it is only when one has the presence of external compressive stresses, that there are formed residual compressive stresses which give rise to static load relaxation. In Figure 9 we see presented the static load and dynamic load relaxations which occur with the application of different alternating stresses on the surface residual compressive stresses of D group specimens. We can see from this figure that, for different values of  $\sigma_a$ , the amount of static load relaxation  $(\Delta\sigma_r/\sigma_r)_{mac}$  and the amount of dynamic load relaxation  $(\Delta\sigma_r/\sigma_r)_{mic}$  are not all the same. When  $\sigma_a$  is high,  $(\Delta\sigma_r/\sigma_r)_{mic} > (\Delta\sigma_r/\sigma_r)_{mac}$ . Moreover, in vicinities close to the fatigue limits, then  $(\Delta\sigma_r/\sigma_r)_{mac} > (\Delta\sigma_r/\sigma_r)_{mic}$ . Static load relaxation is caused by large scale plastic deformation produced in the metal (crystal slip). Therefore, it is a type of loss relaxation, and, necessarily leads to a drop in the fatigue strength of materials. In order to avoid the fatigue losses brought by static load relaxation, the sum of the residual stress of shot peening and externally applied forces should not exceed the bending strength of the materials involved. Under the type of special conditions which exist at fatigue limits, for high strength aluminum alloys, the optimum residual compressive stress values should be:

$$(\sigma_r)_{op} = \sigma_b - \sigma_{-1} = 410 - 210 = 200 \text{ MPa}$$

Normally, going through the control surface shot peening strengths or the industrial process parameters for other surface strengths

in order to obtain the values for the optimum residual compressive stresses as well as the particular depth distributions that go with them is always relatively difficult, and, in the process of industrial production, probably cannot be realized. However, it is possible, through the application of heat treatment after surface strengthening, to cause deformation structures to go through repeated processes such as dislocational cross slips and high climbs under high temperatures. This process causes the residual compressive stress relaxation to reach the hoped-for optimum levels ( $\sigma_r - \sigma_s$ ) (See Figure 10). Because this type of stress relaxation is completed through heat excitation, in order to produce non-failure relaxation, therefore, it is not possible to produce obvious fatigue failures in these materials. The logic of the analysis given above was demonstrated experimentally (13) through the results obtained in fatigue tests which were subsequently conducted on ultra high strength steel GC4. That is to say that the use of heat treatment methods caused the residual compressive stress relaxation in the surface layers of shot peening specimens to reach levels which, later on, did not produce the reappearance of static load stress relaxation. Subsequently, the fatigue strength of these samples showed an even more obvious increase than did the shot peening specimens.

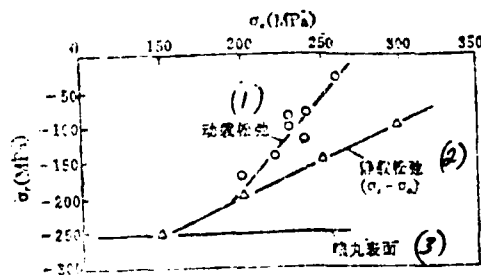


Fig. 9 Micro-and micro-stress relaxation of surface compressive residual stresses under different stress amplitudes of D specimens

Key: 1) Dynamic Load Relaxation; 2) Static Load Relaxation; 3) Shot Peening Surface.

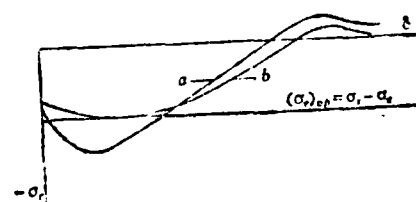


Fig. 10 Schematic diagram of residual stress distribution:  
a—surface strengthening specimen; b—heat-treated specimen after surface strengthening

The discussion above is directed toward the situation in which there is, in the fatigue stress, a compressive stress component (for example, alternating curvature fatigue). Moreover, under conditions in which there is only a tensile-tensile fatigue tensile strength component, due to the fact that residual compressive stress relaxation does not, basically, receive any influence from alternating tensile stresses, therefore, shot peening residual compressive stress fields are not limited by levels of fatigue stress.

Optimum residual compressive stress fields induced by surface strengthening should depend on the factors listed below: (a) form of fatigue loading; (b) bending strength of materials; (c) maximum compressive stress values in fatigue loading.

#### 4. Conclusions

/256

During our research into the stress forms of shot peening stress transformation layers, the influence of organizational transformations and surface light purity on the S-N fatigue curves of LC9 high strength aluminum alloy has led to the following conclusions:

1. Surface shot peening strengthening is not only capable of raising the fatigue strength of the high stress areas of S-N curves, but, at the same time, it is also capable of obviously improving the fatigue characteristics in the vicinity of fatigue limits.

2. Stress strengthening and organizational strengthening are two important strengthening factors relating to the improvement of the fatigue characteristics of materials. Moreover, the reduction in the light purity of shot peening surfaces is a negative factor influencing fatigue strength.

3. Within the high stress areas of S-N curves, organizational strengthening causes the main effects. However, in the low stress areas, it is the stress strengthening which causes the primary effects.

4. When there is a pressure stress component existing in the fatigue loading, within shot peening stress transformation layers, there exists an optimum residual pressure stress field, and the optimum residual stress for this field is:  $(\sigma_r)_o \approx \sigma_c - \sigma_s$ .

## References

- [1] LIU Hwang (WANG Renzhi), "The Fatigue Characteristic of Metallic Materials and the Industrial Technique of Shot Peening Strengthening", National Defense Industrial Publishing Company, 1977.
- [2] Proceedings of First International Conference on Shot Peening (ICSP-1), Paris, September, 1981.
- [3] Proceeding of Second International Conference on Shot Peening (ICSP-2), Chicago, May, 1984.
- [4] Campbell, J. E. Shot Peening for Improved Fatigue Properties and Stress Corrosion Resistance, Metal and Ceramics Information Center, 1971.
- [5] Was, G. S., Pelloux, R. M. and Erabolot, M. C., Effect of Shot Peening Methods on the Fatigue Behavior of Alloy 7075-T6, 445, Proceedings of ICSP-1, Paris, September, 1981.
- [6] Snowman, A. and Schmidt, R. G., The Improvement on Fatigue and Surface Characteristics of Alloy 7075-T6 by Secondary Peening with Glass Beads, 13, Proceedings of ICSP-1, Paris, September, 1981.
- [7] Wang Renzhi (王仁智), Li Xiangbin (李向斌), Tan Yonggui (谭永贵) and Yan Minggao (严鸣高), Investigation on the Microstructure in Shot Peening Surface Straining Layer of Materials, 185, Proceedings of ICSP-1, Paris, September, 1981.
- [8] Wagner, L. and Luetjering, G., Influence of Shot Peening on the Fatigue Behavior of Titanium Alloys, 453, Proceedings of ICSP-1, Paris, September, 1981.
- [9] Hornboge, E., Taumann, M. and Verpoort, C., Influence of Shot Peening on the Fatigue Behavior of a Precipitation Hardenable Austenitic Steel, 381, Proceedings of ICSP-1, Paris, September, 1981.
- [10] WANG RENzhi, "Planned Methods for the Measuring of Stresses Using X-Ray Oscillation Methods", Metallurgy Journal, Vol. 18, No. 4, 1982, 493.
- [11] WANG RENzhi, "The Influence of Shot Peening Residual Stress on the Fatigue Characteristics of 30CrMnSiNi2 High Steel", Aviation Materials, No. 3, 14, 1979.
- [12] James, M. R., The Relaxation of Residual stresses During Fatigue, Residual Stresses and Relaxation, Plenum Press, New York and London, 1982, 297.
- [13] QUI Jing, "Research into the Relationship Between the Fatigue Characteristics and the Shot Peening Stress Transformation Layers of GC-4 Ultra High Strength Steel" (M.A. Graduate Student Dissertation), 1984.



DISTRIBUTION AND EFFECT OF SILICON IN Al-Si COATINGS

/258

CAI Yulin, ZHENG Yunrong, MO Longsheng, YANG Zhonglin

(Beijing Institute of Aeronautical Materials)

**Abstract**

Investigation of distribution and existence mode of silicon in Al-Si coatings has been carried out. It reveals that a Si-rich barrier may be formed between the Si-containing aluminide coating and substrate. The barrier impedes diffusion of Al and Si in the aluminide coating into the substrate, therefore the resistance of the coatings to oxidation at high temperature is improved. Pretreatment enables the Si-rich barrier to be preformed in the Al-Si coatings. Consequently the protective capability of the Al-Si coatings is enhanced.

## SUMMARY

This article represents research into the distribution and forms of existence of Si in Al-Si coatings, and presents for consideration an  $M_6C$  separate layer rich in Si, which blocks the spreading of the Al and Si in the coatings of aluminized objects toward the interior, and because of this raises the ability of coatings to resist high temperature oxidation. Through the utilization of preparatory handling methods, it is possible to cause Al-Si coating layers to form, in advance, separate  $M_6C$  layers which are rich in Si, and this goes another step toward increasing their protective capabilities.

### 1. Forward

In aviation engines, turbine wheel components make widespread use of aluminized products with coatings. A good deal of research indicates that Si, in the improvement of the protective capabilities of aluminized products with coatings, has obvious effects (1-2). However, there is still a shortage of systematic research on the functions and distribution of Si in aluminide objects.

This article compares experimentally the corrosion resistance characteristics of Al and Al-Si coating layers during oxidation and heat corrosion processes, and these tests present information on the distribution and functions of Si.

### 2. Experimental Materials and Methods

The basic material was K3 cast nickel-based high temperature alloy, and the composition of its mother alloy was 0.14C-10.10Cr-4.55Co-5.10W-3.62Mo-5.60Al-2.50Ti-0.08Zr-0.005Ce-68.03Ni (wt. %).

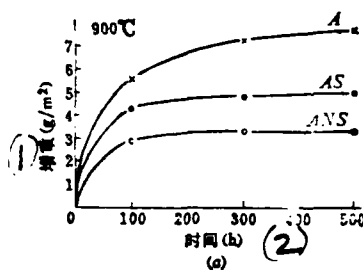
This alloy, in the cast state, underwent penetration coating.

In order to obtain Al-Si coating layers containing different amounts of Si, we employed two differing types of penetration coating industrial techniques (see Table 1).

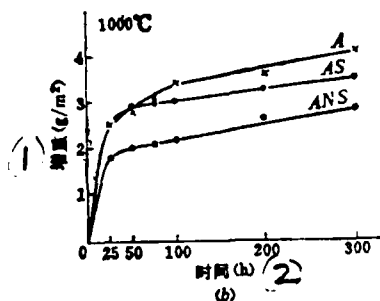
On the specimens after penetration and testing, we used optical microscopes, transmission electron microscopes, scanning of electron microscopes and energy spectra, electron probe, X-Ray diffraction, qualitative metallography and chemical phase to carry out our tests.

### 3. Experimental Results

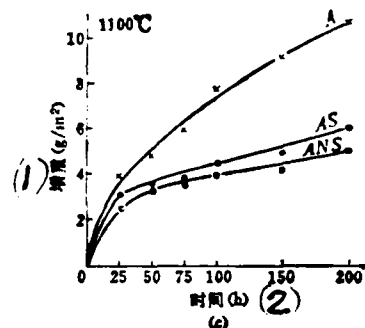
#### 1. High Temperature Static Oxidation Tests



Key: 1) Increase in Weight;  
2) Time.

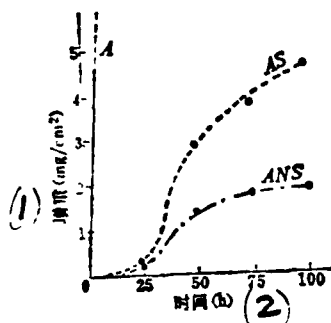


Key: 1) Increase in Weight;  
2) Time.



Key: 1) Increase in Weight;  
2) Time.

Fig.1 Oxidation curves of three coatings at 900, 1000, and 1100°C



Key: 1) Increase in Weight;  
2) Time.

Fig.2 The weight gain-time relationship curves of specimens with three coatings during hot corrosion test with spraying salt

The three types of coatings all had standard base values at 900, 1000, and 1100 degrees Centigrade. ANS penetrating coating showed the smallest increase in oxidation. AS penetration coating was next, and A coating showed the largest increases (See Figure 1).

## 2. Heat Corrosion Tests

The performance of the three types of coating during salt application heat corrosion tests is as shown in Figure 2. The results of experiments in the RFL-1 combustion equipment are as set out in Table 2.

/260

Table 2 Hot corrosion results of gas-spraying salt test for three coatings

(1) 涂层	A			AS			ANS		
(3) 试样号	A-1	A-2	A-3	S-1	S-2	S-3	N-1	N-2	N-3
(4) 失重, kg/m <sup>2</sup>	3.92	2.51	3.27	0.027	0.038	0.518	0.026	0.025	0.026
(5) 平均失重, kg/m <sup>2</sup>	3.23			0.194			0.026		

Key: 1) Increase; 3) Specimen Number; 4) Weight Loss; 5) Average.

From the results presented above, one can see that the heat corrosion capabilities of Al-Si coatings are better than those of Al coatings alone, and, that among them, ANS is the best.

## 3. Penetration Structure

The penetration structures of A coatings and AS coatings are as shown in Figure 3. The penetration structures of these two types of coatings can be divided into interior and exterior areas. The thickness of the A coating exterior layer is 50μ.; that of the interior layer is 10μ. .

The exterior layers of the other two types of coatings are 28 $\mu$ , and their interior layers are 22 $\mu$ . The average Si concentrations in the exterior and interior layers of ANS coatings are 2.53 and 5.75wt%. Moreover, the AS coating breaks down as 1.99 and 2.33wt%. In the phase of the exterior layers of the three types of coatings  $\beta$ -NiAl concentrates the diffused precipitate phase. X-ray diffraction and electron diffraction demonstrate that these diffusion phases are primarily  $\alpha$ -Mo(W),  $\alpha$ -Cr and  $M_6C$ . The exterior layers of Al-Si coatings which are high in Si also have a G phase. Figure 4 is the second phase material point particle and diffraction spectrum of the exterior layer of AS coatings. In the exterior layers, there are still in existence MC carbon compounds which are holdovers from the original alloy. This demonstrates that these two types of coatings belong to the internal dispersion type of coatings.

The interior layers are, for the most part, distributions of  $M_6C$ ,  $M_{23}C_6$ , and  $\sigma$  phase on the basis of NiAl.

Due to the fact that the material point particle of the second phase of coating layers is small and concentrated, as far as the use of electronic probes to accurately measure  $\beta$ -NiAl components is concerned, it is possible to make use of a solution of 10% hydrochloric acid and methyl alcohol to dissolve  $\beta$ -NiAl layers. If one then analyzes the solution and the remnants, he then obtains  $\beta$ -NiAl and minute phase components.

Table 3 shows that  $\beta$ -NiAl includes in its solid contents 0.35% Si; the second phase material point particle only contains 0.19% Si. When the concentration of Si in the penetration agent is increased 9 fold, the Si dissolved in  $\beta$ -NiAl increase from 0.35% to 0.40%; moreover, the second phase material point particle increases its Si content from 0.19% to 0.53%. This clearly shows that different penetration coating methods have very minute influences on the concentrations of Si in the  $\beta$ -NiAl phase; however, they obviously increase the amount of Si contained in the second phase material point particle.

Metallographic observations also clearly show that the material point particle of the second phase exterior layer of Al-Si coating layers is greater than that of coating layers with Al alone; moreover, the second phase material point particle in coating layers with high Si/Al content is even greater.

/261

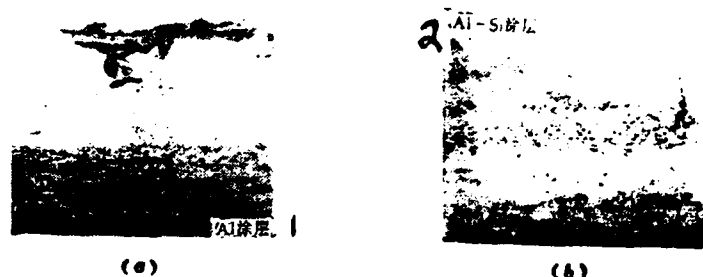


Fig.3 As-coated microstructures of Al and Al-Si coatings 800 ×

Key: (1). Al coating. (2) Al-Si coating.



Fig.4 Replica and electron diffraction pattern of disperse particles in Al-Si coating.  
(a) Replica, 5000 ×; (b)  $\alpha$ -Mo, zone axis[001]; (c)  $MgC(G)$ , zone axis[111].

Table 3 Composition analysis of the external layer for both coatings

(1,2) 涂层代号	(3) 组成相	(5) 化学成分, wt. %							
		Ni	Co	Al	Ti	Cr	Mo	W	Si
A	$\beta$ -NiAl	61.12	2.35	34.18	痕	2.37	痕	痕	—
	$\beta$ -NiAl + (4) 微量相	58.76	2.26	35.50	0.55	2.51	0.46	—	—
AS	$\beta$ -NiAl	63.48	2.16	32.25	—	1.75	—	—	0.35
	$\beta$ -NiAl + (4) 微量相	61.25	2.11	32.87	0.50	2.11	0.41	—	0.54

Key: 1) Coating; 2) Coating Symbol; 3) Composition Phase; 4) Minute Content Phase; 5) Chemical Composition.

#### 4. Coating Organization Changes in the Processe of Static Resistance to Oxidation

After Al-Si coatings undergo long term exposure to 900 degree Centigrade high heat, X-ray diffraction analysis clearly shows that there is no G phase, and the second material point particle of  $\alpha$ -Mo(W),  $\alpha$ -Cr and  $M_6C$ , which is diffusely distributed in the  $\beta$ -NiAl exterior layer, begins to coarsen. There is an obvious lengthening of the second phase of the interior layer and transitional layer. Figure 5 shows the structure of Al-Si coating layers which have undergone 900 degree Centigrade heat exposure for 5000 hours. Electronic probe resuts show that Si is still richly concentrated in the  $M_6C$  material point particle. Looking at the coating layers as a whole, Al shows the peculiar characteristic of being high in the exterior and low in the interior; moreover, Si is the exact opposite. In the interior layer, the amount of Si contained is very high. The material point particle of this layer forms itself from the  $M_6C$ ,  $M_{23}C_6$ , and  $\sigma$  phase, moreover, the Si is principally contained in  $M_6C$ .

During exposure to 1000-1050 degree Centigrade heat, the second phase material point particle is much coarser than the present with 900 degree centigrade heat (Figure 6). Due to the fact that these temperatures are relatively high, there is large scale formation of  $M_6C$  in the interior layer.  $M_{23}C_6$  is gradually destroyed and is replaced to become a large  $\sigma$  phase. It goes without saying that /262 no matter which type of coating it is, during the process of heat exposure, the Al concentration in the  $\beta$ -NiAl phase drops abruptly after which it stabilizes at the 16-19% level. This article clearly demonstrates that the lowest Al concentration permissible in order to maintain the required  $\beta$ -NiAl phase in the coating is 16%; moreover, the lowest permissible Al concentration required to maintain  $\gamma'$  is 6%.

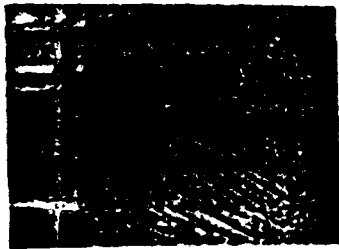


Fig 5 Microstructure of AS coating after 900°C,  
5000 hours. 1000 ×



Fig 6 Microstructure of AS coating after therm-  
al exposure of 1000°C/300 hours. 1000 ×

At 1100 degrees Centigrade, there is a rapid increase in the amount of  $M_6C$  and  $\sigma$  phase in the interior layer of the coating; moreover, one sees the very rapid formation of continuous separate layers. Fig. 7 is, at 1100 degrees Centigrade and varying lengths of time, the results concerning coating layer structure and electronic probing.

From this figure we can see that, after undergoing 25 hours of exposure, one sees the formation, on the boundary between the basic body and the coating layer, of a continuous separate layer along the basic body wall. X-ray diffraction and electronic probe analysis clearly show that this separate layer is primarily formed from from a  $M_6C$  and  $\sigma$  phase which is rich in Si. The distribution curvew of Ni and Si, which



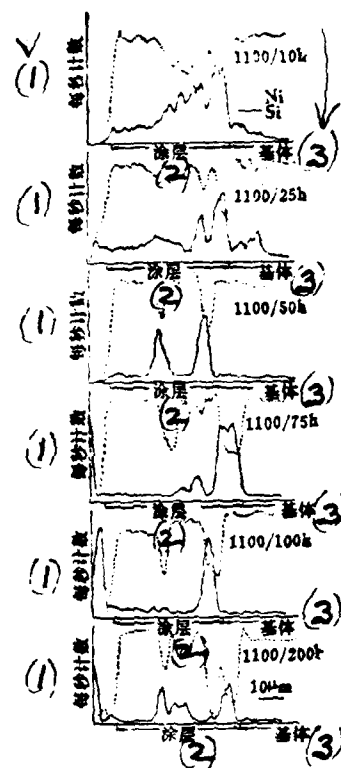
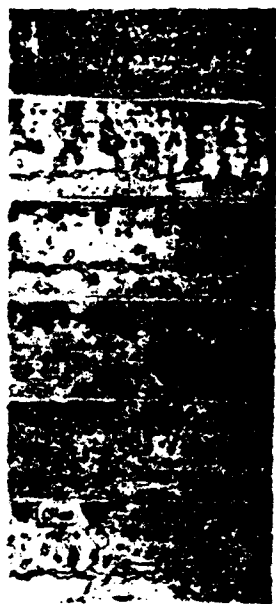


Fig. 7. Microstructure and Ni, Si distribution of AS coating after the thermal exposure of 1100°C/10~200 hours

Key: 1) Recorded Values Per Second; 2) Coating Layer; 3) Basic Body.

cross the coating layer, show that, in the vicinity of the separate layer, one sees the occurrence of peak values for Si and the corresponding low values for Ni. Besides this, on the distribution curves for Ni, there is one type of low value which does not correspond to a peak value for Si. This is a phase rich in Cr. On the constituent distribution chart (Fig. 8) one can see a considerable number of  $\sigma$  phases rich in Cr and of  $M_3C$  phases rich in W, Mo, and Si.

At the high temperature of 1100 degrees Centigrade, the decomposition of the  $\beta$  phase is still very slow. After 100 hours, it still maintains approximately 30% of the  $\beta$  phase. During the exposure process as a whole, the thickness of coating layers remains unchanged, which shows that Al shows no trace of diffusion toward the interior. During the decomposition process in the AS coating layers, it is always true that the interior section is first to turn itself into a  $\gamma$  phase; moreover, a large amount of  $\beta$  phase is preserved in the exterior layers. It is only when one reaches 100 hours that one begins to see the localized appearance of  $\gamma'$  phase.

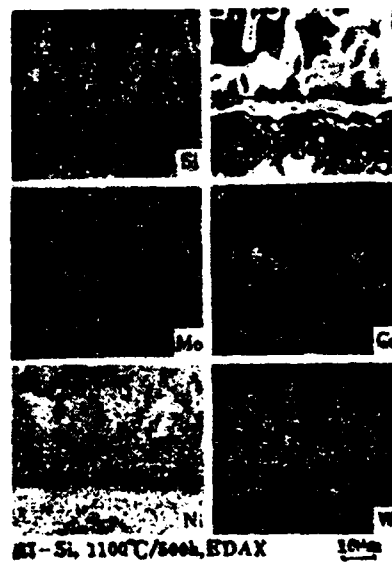


Fig. 8 SEM morphology and element distribution of the barrier rich in Si formed by 1100°C/500 hours

When we made use of quantitative metallographic methods to carry out measurements of the  $M_6C$  percentage volumes of the interior layers in various coating layers, the results were as shown in Table 4.

Table 4. A Comparison of the Percentage Volumes and Thicknesses of  $M_6C$  Layers After Five Types of Coating Layers Underwent 1100 Degree Centigrade Heat for 500 Hours

Table 4  $M_6C$  layer thickness and volume percent of five coatings after 1100°C/500 hours

涂层类型 (1)	S	J	A-C	Al-Si	Al
$M_6C$ 厚度, $\mu m$ (2)	55	45	37	30	22
$M_6C$ 量, vol. % (3)	18	28	25	30	14

Key: 1) Type of Coating Layer; 2) Layer Thickness; 3) Amount.

Note: S, J, A-C and Al-Si are separate types of Al-Si coating layers containing different amounts of Si.

The experimental results presented above clearly show that, not only are the carbon compound concentration areas in coating layers with Al penetration alone very narrow in width, but also, their amounts are very small. Therefore, there is no capability to form separate layers. Several types of Al-Si coating layers, due to the fact that Si promotes the formation of  $M_6C$ , ultimately causes the formation of  $M_6C$  separate layers between the coating layers and the basic body.

##### 5. The Preformation of Separate Layers

/264

In order to raise the capability of ANS to resist oxidation and protect coating layers during exposure to 900-1000 degree Centigrade heat, we made use of pretreatment methods which made it possible to preform separate layers. The structure of these layers is as shown in Figure 9(a). Specimens of ANS coating layers which had undergone pretreatment and specimens which had not, after undergoing 1000 degree Centigrade heat for 100 hours showed microstructures as shown in Figure 9(b) and (c). Coating layers which

had not been pretreated formed large amounts of  $\gamma'$  phase in exterior layers and close to the surface layers; moreover, they formed very wide transitional layers. In cases where the separate layers had been preformed, one saw the formation of a type of exterior layer with  $\gamma'$  phase to which was finely and evenly added  $\beta$  phase. The interior layers were principally formed from  $M_6C$  and  $\sigma$  phases surrounded by  $\gamma'$  phase. Preformed separate layers were still in existence, but, there was no obvious formation of transitional layers. The interior of separate layers all had a normal  $\gamma + \gamma'$  structure.



Fig 9 Microstructure of pretreatment and 1100°C/100 hours thermal exposure ANS coatings.  
(a) pretreatment, 2500 $\times$ , (b) no pretreatment + 1100°C/100 hours, (c) pretreatment + 1100°C/  
100 hours, 1000 $\times$ .

## 6. Coating Layer Structure After Heat Corrosion Testing

After tests using hot air and salt spray, the external appearance of three types of coating layers is compared as seen in Figure 10. After 40 hours of testing A coating layers show an overall appearance of green scarring; after 80 hours this overall appearance turns to one of pustule. AS coating layers, after 60 hours of experimentation, had

one rod which showed the appearance of green spots, but, only after 140 hours did these develop into the pustule type damage mentioned above. However, two of the rods totally maintained their integrity as specimens. ANS coating layer specimen rods all maintained their integrity from beginning to end. This is totally in line with the heat corrosion loss measurements given above.

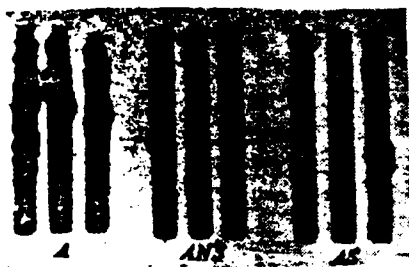


Fig. 10 The appearance of three coatings after gas corrosion test, 0.7×

The metallographic tests which were done on the specimens which went through the experimentation described above clearly showed that ANS coating layers maintained their integrity; however, A coating layers showed total metal consumption in certain localized areas as well as the peculiar characteristics of sulphur corrosion, which appeared clearly in areas of the basic body which were totally exposed.

#### 4. Results and Discussion

/265

There is a relationship between the distribution of Si in Al-Si coating layers and solubility in the various kinds of phases. The

solubility of Si in  $\beta$ -NiAl phase is very low, usually lower than 0.40%; however, its solubility in  $\gamma'$  phase is still higher than 1.0%. The amount of Si contained in most  $M_2C$  in the separate layer was between 6-7%. This is relatively close to the 9% value reported in reference(3). It is precisely because large amounts of Si are contained in  $M_2C$  that some people write  $M_2C$  as  $M_2SiC$  (4). In the high Si coating layer of ANS, one still finds the presence of a G phase. In a penetrated state it is very diffused, and, if one is using an electronic probe for testing it is difficult to identify as a component. In reality, the G phase is the ternary compound  $A_2B_2C$ , in which the C is the atomic Si. The G phase is unstable, and, when it is exposed to heat, due to the fact that surface oxidation losses eliminate Si and form  $M_2C$ , a certain amount of Si is consumed, which causes G phase decomposition. Among specimens which were exposed to 900 degrees Centigrade for 5000 hours, there has, as yet, been no appearance of the G phase.

The formation of separate layers has an obvious function in the blocking of mutual diffusion of alloy elements between coating layers and the basic body of the alloy. On the underside of the separation layers, in close contact, is the  $\gamma + \gamma'$  structure of the basic body of the alloy. This avoids the formation of an  $\sigma$  phase slice in the transition layer. This is doubtless helpful in extending the protective life of coating layers and raising the mechanical capabilities protecting the alloy. In another vein, the results of these experiments show that the existence of separating layers has no obvious reducing or slowing function as far as the decomposition of the  $\beta$  phase is concerned. One reason for this is that Si is a component of the  $\gamma'$  phase, and it is capable of promoting the  $\beta \rightarrow \gamma'$  transformation. Another reason is that the Al concentration in Al-Si coating layers is lower than that in Al coating layers. Further supplementary testing has shown that, in the initial case, the Al concentration in both Al and Al-Si coating layers maintains itself at 19%. After undergoing 1100 degree Centigrade temperatures for 100 hours of oxidation resistance testing, the decomposition of the  $\beta$  phase of Al coating layers is even faster than

that in Al-Si coating layers.

$\gamma'$  phase containing Si possesses excellent oxidation resistance capabilities. After undergoing 1100 degree Centigrade oxidation testing for 200 hours, the  $\beta$  phase completely decomposes to form Al-Si coating layer  $\gamma'$  phase, and still maintains a certain amount of  $\beta$  phase Al coating layer which goes to improve performance in the 1100 degree Centigrade oxidation resistance tests. The results of these show that the oxidation speed of the former is half that of the latter. This clearly demonstrates that  $\gamma'$  phase containing Si has oxidation resistance characteristics which are even better than those of  $\beta$ -NiAl.

## 5. Conclusions

(1) Al-Si coating layers possess even higher oxidation resistance and heat corrosion resistance characteristics than do Al coating layers.

(2) The solubility of Si in  $\beta$ -NiAl phase is extremely low, and, this is primarily due to the formation and existence of a second phase material point particle.

(3) Si has the capability to promote the formation of  $M_2C$  as well as the formation of separation layers between coating layers and the basic body of alloy.

(4) The use of techniques to preform separating layers is capable of forming a Si rich  $M_2C$  separation layer in the coating layers, and of causing the structure of the transition layers to be stable. This preformation technique is also capable of further increasing the oxidation resistance of coating layers.

## References

- (1) Zemskov, G. V. et al., Protective Coatings on Metals, Vol. 4 (1972).
- (2) Moore, V. S., Brentall, W. D., Stetson, A. R., NASA CR-72714 N72-1857.
- (3) Pearcey, B. J., Smashey, R. W., Trans. AIME, 239 (1967), P. 451.
- (4) Preis, G., Lennartz, G., Arch. Eisenhutenwesen, 46 (1975), S. 589.

CORRELATION BETWEEN INTERFACE REACTION AND PROPERTIES  
OF CARBON AND GRAPHITE FIBER REINFORCED ALUMINUM  
COMPOSITES

/267

ZHAO Chang cheng

(Shanghai Jiaotong University)

ABSTRACT

The correlation between temperature and the content of interface reaction product  $Al_4C_3$  in carbon and graphite fibre reinforced aluminium precursors and the relation of the tensile strength of the precursors to the content of  $Al_4C_3$  and temperature are studied. The fractography of every precursor is analysed with SEM. The aluminium matrix of the precursors is dissolved with HCl solution after thermal exposure at various temperatures, the surface of dealuminated fibres is examined and the tensile strength of the fibres is tested.

The temperature at which the strength of precursors drops dramatically is about 75~100°C higher for Gr-Al than for C-Al (about 625 and 550°C respectively). The strengths both of the C-Al and Gr-Al precursors are very low at temperatures over 650°C (30% and 40% of the room-temperature strength respectively).

The SEM analyses and tensile tests demonstrate that the decrease of precursor strength is prior to the surface damage of the fibres and the fibres may not be degraded by the interface reaction product  $Al_4C_3$  up to certain temperature. Only when a lot of  $Al_4C_3$  is formed, the remarkable deterioration of fibres can be observed and the strength of the precursors drops significantly too. Degradation of the fibres is merely one of the reasons why the strength of the precursors decreases. Moreover, it occurs only at higher temperature. Formation of  $Al_4C_3$ , probably, changes the fracture model of the precursors.



## SUMMARY

This article represents a study relating to the amount and temperature of the  $Al_4C_3$  which is produced in reactions on the surface areas of pure aluminum composite wires which have been strengthened by the addition of carbon and graphite filaments. It also investigates the relationship between temperature and the amounts of  $Al_4C_3$  as well as the room temperature tensile strength of composite wires. In the course of this research, we did electron microscope scanning analyses of break surfaces in various types of composite wires, and it was discovered that there are three types of break surface characteristics depending on varying heat exposure temperatures and strengths. After hydrochloric acid was used as a cleaning agent and specimens were exposed to varying degrees of heat, the aluminum base of the composite wires was analysed in terms of the surface form of the exposed aluminum filaments and measurements were made of tensile strengths. From this we obtained the temperature range in which the filaments in the composite wires received heat damage.

### 1. Forward

The factors which influence the strength of carbon-aluminum composite materials are very numerous (1). One of the most important among them is the reactions which occur on the boundary surfaces between the basic body and the filaments. The normal production temperature for carbon-aluminum composite materials is normally close to or higher than the melting point of the basic body, that is to say, between the solid phase line and the liquid phase line of the basic body. At these temperatures, in terms of thermodynamics, the aluminum base body and the carbon filaments will both give rise to chemical reactions. A large number of researchers (2-9) have investigated the mutual interactions of the carbon filaments and the aluminum basic body. These researchers point out that, at certain temperatures, the boundary layers between

these two sections produce  $Al_4C_3$ , and that its amount determines the strength level of composite materials. However, the temperatures at which one gets the clear formation of  $Al_4C_3$ , and the temperatures at which one gets a clear drop in the strength of the composite materials are not the same; moreover, all this research simply pointed out the fact that carbon filaments and aluminum basic bodies, at certain temperatures, are capable of forming  $Al_4C_3$ . It gives no systematic presentation of the relationship between different aluminum bodies and different filament  $Al_4C_3$ , between the amount of  $Al_4C_3$  produced and the strength of the composite materials at various differing temperatures. This article represents an attempt to advance the research into the relationships connecting the vertical tensile strength of composite wires and the amount of  $Al_4C_3$  produced on the boundary layers after composite wires composed of a pure aluminum basic body and two different types of filaments composed of carbon and graphite are exposed to differing temperatures. Moreover, this research carries out an analytical discussion of such questions as the thicknesses of  $Al_4C_3$ , which must be reached before there is a certain level of destruction in composite materials or the relationship between close observations of the status of filament surfaces and break forms and the amounts of  $Al_4C_3$  and filament damage. This research is also aimed at supplying adequate data for selection of optimal industrial process parameters for use in producing carbon aluminum composite materials, and, at the same time, it is aimed, on the theoretical level, at exploring and understanding the laws that govern the reactions which take place on boundary surfaces.

## 2. Experiments

All the specimens used in these experiments are composite carbon-aluminum wires test produced at our school. In their preparation, we used carbon filament produced at a certain factory in our country and graphite filament HM produced in Japan as strengthening agents. In our research, we made systematic comparisons between two types of composite wire with pure aluminum basic bodies or matrices. We also made some

relative comparisons between two types of filament strengthened pure aluminum composite wires which are produced in Japan, that is, T300 and M40.

During the heat exposure testing of composite wires, the vacuum was maintained at  $10^{-4}$ ~ $10^{-5}$ , the temperatures were 400, 500, 550, 575, 600, 650, 700 degrees Centigrade, the time durations were generally one hour, but, in a small number of cases, was four hours. This was done in order to obtain different specimens of composite wire during the reaction processes. The room temperature tensile strength of composite wire before and after heat exposure was measured on the Model XLL 50 experimental apparatus.  $Al_4C_3$  amount contained in specimens was measured using the Model 102G gas phase color spectrometer(10). With the use of electron microscope scanning, detailed observations were made of the various types of break forms. Sections of composite wire were stripped with hydrochloric acid solution down to the aluminum basic body or matrix, and the tensile strength of the stripped aluminum filaments was measured. Observations were also made of the surface forms. /268

### 3. Results and Discussion

#### 1. Changes in the Amount of $Al_4C_3$ in Composite Wire After Exposure to Different Temperatures

After using the Ti-B method to carry out surface pretreatment of carbon filaments, the coating layer of Ti-B which settled out and accumulated on the filaments, although it had the capability to very greatly improve the malleability of the molten metal of the filaments, did, however, following the raising of the exposure temperature, show a gradual weakening of its capability to successfully block the occurrence of mutual reactions between the filaments and the basic body, and this weakening continued to the point where the coating layer itself was also capable of taking part in the surface layer reactions (11). Because of this, following a rise in the temperature, the amounts of products from surface layer reactions in the composite wire continuously increased. The main component of these products was  $Al_4C_3$ . Fig. 1 gives the patterns in the amounts of  $Al_4C_3$  in various types of composite wire following changes in temperature.

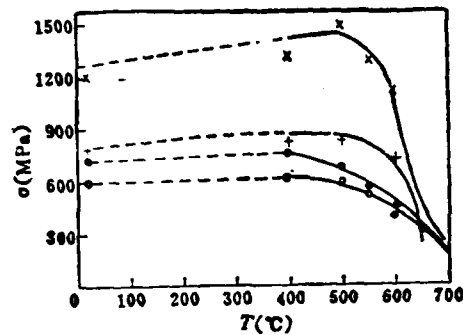


Fig.1 Amount of  $Al_4C_3$  in the precursors VS temperature

From Fig. 1 one can see that, although the amount of  $Al_4C_3$  in the various types of composite wire increase with increases in temperature, however, the rules governing the changes for different types of filaments are different. First of all, in the initial composite wire, which has not undergone heat exposure, the amount of  $Al_4C_3$  contained in carbon aluminum composites is several times higher than the amounts contained in graphite aluminum composites. The values for such composites as the Chinese produced carbon filament, T300, HM, and M40 were, respectively, 9410, 37200, 1040 and 1060 ppm. Consequently, the temperature range for abrupt increases in the amounts of  $Al_4C_3$  in different filaments is obviously different. For carbon filaments, it is about 500 degrees Centigrade, and, for graphite filaments, it is about 600 degrees

Centigrade. Clearly, this is caused by differences in the structures of the filaments. Because of this, the temperatures used with aluminum based composite materials with graphite filaments used as strengthening agents, or under certain other temperature conditions, all make the life of the graphite composites longer than that of the carbon-aluminum composites. It is worth pointing out that, under the highest temperatures, (for example, 650 degrees Centigrade), in the graphite aluminum wires, increases are faster than is the case with carbon-aluminum composite wire. For example, at 650 degrees Centigrade and 700 degrees Centigrade, in the carbon-aluminum composite wire (Chinese produced), the amounts of  $Al_2C_3$  contained were respectively 32000 and 780000 ppm. However, in the graphite aluminum case (HM), the respective values were 60500 and 187000 or more. The reason for this is continuing to be looked into in more detailed research.

## 2. Changes in the Tensile Strength of Composite Wire After Exposure to Different Temperatures

The various types of composite wires, after undergoing relatively low temperature exposure (less than 400-450 degrees Centigrade) all show strengths that increase with differing amplitudes. This is related to improvements in the combining state of the surface layer between filament and main body matrix as well as to the elimination of residual heat stress. However, it seems that the principal thing is the improvement in the combining status of the boundary layer. The results of analysis of breaks also clearly demonstrate this point.

Following the increase of the heat exposure temperature, the strength of each of the various types of composite wire begins to drop; however, for different types of wire, the temperature at which the wire begins to show obvious reductions in strength is different. Generally

speaking, graphite-aluminum composite wire has 75-100 degrees Centigrade higher reduction temperatures than do carbon -aluminum composite wires. Fig. 2 shows that, after the various types of wire are exposed to heat, the tensile strength and temperature are related in the ways shown. One can see from the figure that the strength of carbon-aluminum composite wire already shows obvious reduction at 550 degrees Centigrade. The Chinese produced and T300 type carbon filament strengthened composite wires, at the temperature mentioned, see their strengths go from the room temperature values of 735 and 600 MPa down to 535 and 465 MPa . The strengths of graphite aluminum composite wires do not begin relatively large amplitude drops until the temperature reaches 625 degrees Centigrade. The strengths of the two kinds of graphite fiber strengthened composite wires, M40 and HM, at the same temperature, show drops from their room temperature values of 750 and 1250 MPa down to 400 and 620 MPa.

/269

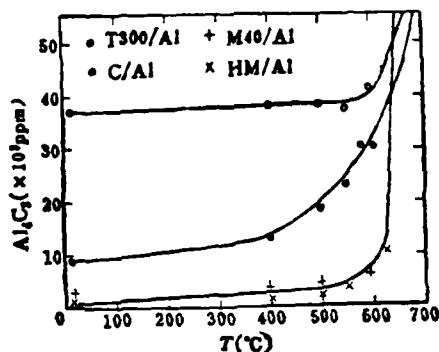


Fig. 2 Strength of the precursors VS temperature

If one takes Fig. 1 and Fig. 2 and compares them, it is not difficult to see that the amount of  $Al_4C_3$  and the strength of the specimens vary in a basically direct way with changes in temperature. Within a certain range of temperatures (below 400-450 degrees Centigrade) there is a slight increase in the amount of  $Al_4C_3$  in response to a rise in temperature. A corresponding rise in the strength of the composite

wire also takes place. This explains the corresponding increase in the amount of  $Al_4C_3$ , and the raising effect it has on the composite strength of boundary surfaces. It is only when there is a rise to a certain temperature value with its corresponding increase in the production of  $Al_4C_3$ , that the strength of the composite wire shows a relatively significant drop. It appears that the thickness of the brittle  $Al_4C_3$  layer is at a boundary value. It is only after the actual thickness of  $Al_4C_3$  in this carbon-aluminum composite material surpasses this boundary value that one gets an effect produced on the strength of the material (12-14).; moreover, following an incremental increase in the temperature, there is an abrupt increase in the amount of  $Al_4C_3$ , and the capabilities of the material drop steeply. If the temperature of heat exposure exceeds 650 degrees Centigrade, the strength of the various types of composite wires all drop to a 300-400 MPa level. However, calculating this critical thickness either from experimental measurements or from theoretical calculations is still proving a difficult matter at present.

### 3. The Relationship Between the Form of Fracture Breaks and Tensile Strength

In composite wires which have not yet undergone heat exposure treatment, due to the fact that boundary surface amalgamation has still not reached an ideal state, the fractures contain large amounts of protruding fibers, and, one can sometimes see the phenomenon of a clear separation between fibers and the matrix body; moreover, one can clearly see a shrinking of the matrix body. Following an increase in the temperature of heat exposure, the boundary surface reactions increase abruptly; composite strength also follows it upward. The fracture breaks on tensile specimens are uneven and jagged with fibers protruding, however, there is less of this than in the former case. The main body

matrix also shows a shrinking phenomenon, and, on protruding fibers, one can sometimes see adhesion to the main body. It is fracture breaks of this type which have the highest composite wire strengths. After the heat exposure temperature has exceeded a certain level, the boundary surface reaction is extremely heavy. The thickness of reaction products increases dramatically. Due to the fact that carbon-aluminum composite material boundary surface combining belongs to the reaction binding type, the simultaneous production of large amounts of brittle reaction products necessarily causes a very large increase in the boundary surface viscous binding strength. The fractures on tensile specimens were even and neat and did not show the occurrence of protruding fibers. These breaks were classic examples of brittle fractures. The strength of composite wires which had this type of fracture was all relatively low (1,15). From the three types of results shown above one can know that when one adds fibers of increased brittleness to a matrix body which is pliable, the compounds which form on the boundary surfaces of this kind of composite material produce a material of outstanding strength, but the cohesion between the fibers and the matrix body is necessarily moderate. This point is also recognized in most of the related references which have been published up to now.

#### 4. Exposed Aluminum Fiber Surfaces and Strength Analysis

In order to analyze the relationship between carbon filament losses and the strength of composite wires, as well such related questions as the causes of the lowering of the strengths of composite wires, we took composite wires which had undergone several sessions of exposure to heat and used hydrochloric acid solution to remove the aluminum matrix body. Using electron microscope scanning, we observed the surface appearance of fibers which had been separated out, and measured their strength. From these experiments we obtained the following information: in the two kinds of composite wires, it was only after filament surfaces had gone through relatively high temperature and long duration heat exposures in a



vacuum, that their surfaces began to show the appearance of pits (Fig. 3). The strength of the fibers was obviously damaged, and the temperature at which carbon fibers showed the appearance of pits was lower than the corresponding temperature for graphite fibers. These two temperatures were, respectively, 650 degrees Centigrade and 700 degrees Centigrade, approximately. These temperatures are approximately 75-100 degrees Centigrade higher than the temperature at which the strength of composite wires abruptly drops. The pits on fiber surfaces are corrosion pits which remain after the boundary surface reaction product  $Al_4C_3$  is cleaned away together with the matrix body using hydrochloric acid. These results show that: (1) boundary surface reaction products do not necessarily cause filament deterioration. It is only after specimens have undergone relatively high temperature treatment and there has been produced large quantities of  $Al_4C_3$ , that fiber strength shows a clear drop. Moreover, this temperature is higher than the temperature at which the strength of composite wires drops abruptly. (2) The strength of composite wires has already dropped before there is fiber damage. Moreover, a large number of references explain that this filament damage is caused by the mutual reaction of matrix body and fibers. Fiber damage is only one of the reasons that composite wires lose their strength under relatively high temperatures. After the amount of  $Al_4C_3$  passes the critical value, the type of damage to the composite wires can exhibit changes. Under the effect of external loading, fractures change from the initial production of cracks in the  $Al_4C_3$  layer, which is lower in this compound than the filaments, to a situation /27 in which these cracks immediately spread out to the fibers themselves, which causes the fibers to fracture. This process continues so that the composite material suffers damage. This matches quite well with the analysis found in references (12-14). The amount of  $Al_4C_3$  which creates fiber damage is clearly much higher than the critical value. Of course, damage to composite fibers may possibly also have other causes.

(1)



Fig.3 Surface morphology of the dealuminated fibres  
(a) Carbon fibre 650°C 4hr (b) Graphite fibre 700°C 4hr.

#### 4. Conclusions

1. In composite wires which have not yet undergone heat exposure treatment, there are definite amounts of  $Al_4C_3$  present. The amount of  $Al_4C_3$  contained in carbon-aluminum composites is higher than the amount of that compound contained in graphite-aluminum composites. Following an increase in temperature, the amount of  $Al_4C_3$  which is contained in the two types of composite wires constantly increases. When the temperatures are low, the changes are smooth and stable. When the temperature is higher than 500 degrees Centigrade or 600 degrees Centigrade respectively, there is a clear increase. When the temperature is higher than 650 degrees Centigrade the upward movement is abrupt.

2. Following the rise in temperature, the strength of the composite wire begins to slightly increase; however, it subsequently begins to drop incessantly. The temperatures at which the strengths of these two types of composite wires show clear decreases are not the same. The graphite-aluminum composite temperature is 75-100 degrees Centigrade higher than the temperature for the carbon-aluminum composite, that is, respectively, 550 and 625 degrees Centigrade. The drop in strength which follows the temperature change as well as the change in the amount of  $Al_4C_3$  clearly vary accordingly. When the temperature is higher than 650 degrees Centigrade, the rates of strength preservation for the two types of composite wires are, respectively, 30% and 40%.

3. There are three types of fracture break forms, and there is a large amount of filament protruding in specimens which have not yet been heat treated. After undergoing heat treatment at a certain temperature (below 400-450 degrees Centigrade), the boundary surface viscosity binding is improved, the fractures are uneven, and there are fiber protruberances. However, these phenomena are not as severe as in the former cases. On several of the fibers which can be pulled out, one can see viscous attachments to the matrix body. After high temperature treatment, the fractures are even and there are no protruding filaments. They are classic brittle fractures.

4. The drop in the strength of composite wire consists first in damage to the fibers. Within a certain temperature range, the boundary surface reaction product  $Al_4C_3$  does not necessarily cause filament damage, however, it is capable of influencing the strength of composite wires. After undergoing high temperature heat treatment, there is a violent increase in the amount of  $Al_4C_3$ . It is only then that one gets fiber damage and a steep decline in the strength of composite wires. Fiber damage is only one of the causes of a steep decline in strength of composite wires. The existence of  $Al_4C_3$  is capable of changing the process of destruction of the composite wires.

WANG Hong hua and CHEN Rong are both comrades who have supplied part of the data for this article.

## References

- [1] ZHANG Guo ding, LI Xian gan, WANG Wen lung, Shanghai Jiaotong University Journal, 1983, No. 2, 89.
- [2] Khen. I. H., Met. Trans., vol. 7A (1976), 1281.
- [3] Baker. S. J., Bonfield. W., J. Mat. Sci., vol. 13 (1978), № 6, 1329, № 8, 1822.
- [4] Jackson. P. W., Met. Eng. Quart., vol. 9 (1969), № 3, 22.
- [5] Amateau. M. F., J. Comp. Mat., vol. 10 (1976), 279.
- [6] Соколовская, Е. М., Гусев, Л. С., Физикохимия Композиционных Материалов, М., Изд-во Моск. Ун-та, 1978.
- [7] Килин, В. С., Дергунова, В. С., Шоршоров, М. Х., Антипов, В. И., Кривцова, В. М., Котелни, А. С., Композиц. Материалы, Изд-во Наука, 1981.
- [8] Шоршоров, М. Х., Волокнистые Композиц. Матер. с Металл. Матрицей, М. Машиностроение, 1981.
- [9] Shojiro OCHIAI, Yotaro MURAKAMI, J. Mat. Sci., vol. 14 (1979), 831.
- [10] AD/A-007057, 1975.
- [11] Marcus, H. L. AD-A110787, 1982.
- [12] S. OCHIAI, S. URAKAWA, KAMEYAMA, Y. MURAKAMI, Met. Trans., vol. 11A (1980), 525.
- [13] S. OCHIAI, Y. MURAKAMI, Met. Trans., vol. 12A (1981), 1155.
- [14] Shorshorov, M. Kh., Ustinov, L. M., Zirlin, A. M., J. Mat. Sci., vol. 14 (1979), 1850.
- [15] ZHANG Guo ding, LI Xian gan, WANG Wen lung, Shanghai Jiaotong University Journal, 1982, 6.

PRECIPITATION CHARACTERISTICS OF METASTABLE  
PHASE IN TITANIUM ALLOY TB2

/272

YAO Jin sheng

(Shanghai Institute of Iron and Steel)

WANG Shi hong

(Beijing Institute of Aeronautics and Astronautics)

ABSTRACT

The purpose of the research is to study the transformation behavior of metastable  $\beta$  phase and to establish relationship between microstructure and parameters of heat treatment in TB2 alloy. Quantitative optical and scanning electron microscopy methods have been used to measure the extent of transformation. The crystal structure and orientation relationship have been identified by electron diffraction analysis. According to the results of experiments, isothermal and aging transformation diagrams are illustrated. The factors exerting effect on transformation kinetics are also discussed. It is found that the  $\alpha$  phase is directly precipitated from the metastable  $\beta$  phase at 400 to 700°C and follows the well known Burgers orientation relationship, i. e.  $\langle 111 \rangle_{\beta} // \langle 11\bar{2}0 \rangle_{\alpha}$ ,  $\langle 110 \rangle_{\beta} // \langle 0001 \rangle_{\alpha}$ , referred to as type 1. At temperature below 400°C,  $\beta$  phase transforms into  $\omega$ , an intermediate precipitate, which is related to  $\beta$  matrix by the orientation relationship  $\langle 0001 \rangle_{\beta} // \langle 111 \rangle_{\omega}$ ,  $\langle 11\bar{2}0 \rangle_{\beta} // \langle 110 \rangle_{\omega}$ . The remarkable influence of the solution-ning temperature, content of oxygen and heating rate of aging on the transformation kinetics of the alloy is confirmed.

## SUMMARY

This article is an attempt to do research into the rules governing transformations in the metastable  $\beta$  phase during the processing of TB2 alloy under conditions of equal temperature and time exposure. The article also attempts to measure the dynamics curves associated with decomposition under equal temperature and time conditions, as well as the relationship between the nature of the various phases broken out during the various stages and their orientations. In addition, it attempts to research such topics as the effects of time on such characteristics as hardness. Moreover, it discovers the constituents of the alloy, and the fact that purity, solid state temperature, as well as such factors as the speed of thermal increases over time all have obvious influences.

### 1. Forward

TB2 belongs to the Ti-Mo-V-Cr-Al series of metastable  $\beta$  phase type alloys. When these alloys are passed through solid state time effects processing, it is possible to achieve high strength levels. In order to preserve the optimum match up between strength, pliability and other mechanical characteristics, heat treatment is one of the keys. Moreover, although there has been work done on the nature of phase changes which are the foundation of this process (1), this work has not been systematic or thorough. This is particularly true of the area of low temperature transformations. This article attempts to fill in the inadequacies in this area.

### 2. Testing Process

The basic materials for testing were 5mm diameter TB2 alloy cold drawn wire and 1.6mm thick plates of the same alloy. The chemical composition of these materials is shown in Table 1.

water cooled. From this data, we measured the dynamics of the phase decomposition as well as the relationship between the nature of the structural characteristics of specific transformation products and their orientations; moreover, these were measured after long term exposure to increases in temperature in order to find out whether or not there was the production of mutually distinguishable transformations. In order to prevent the mutual mixing and dilution of the products of initial decomposition in the  $\beta$  phase and the difficult to melt impurities in the alloy, during the tests, we made use of scanning and transmission electron microscopy in order to fix the points at which isothermal transformations begin. The results were very good, and are shown in Fig. 1. From this, we set up the dynamics curves for the isothermal transformations (Fig. 2), and, from the nature of these, it is possible to define three separate regions: high temperature (450-700 degrees Centigrade), medium temperature (350-400 degrees Centigrade), and low temperature (250-300 degrees Centigrade).



Fig. 1 Microstructure features at initial stages of  $\beta$ -phase decomposition

(a) 500°C, 2 分钟 (b) 500°C, 10 分钟

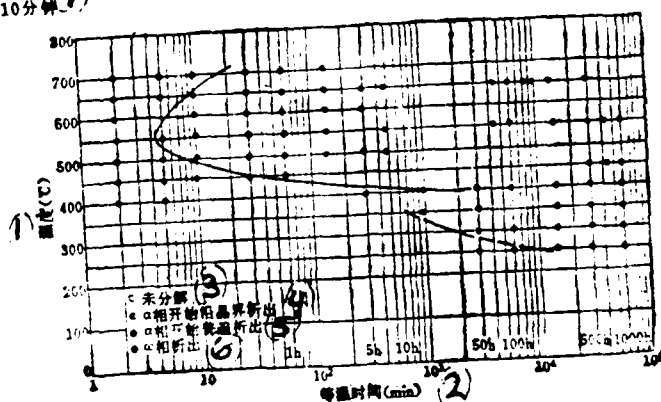


Fig. 2 TTT diagram for TB2 alloy

Key: 1) Temperature; 2) Isothermal Time; 3) Not Yet Decomposed; 4) Phase Begins to Separate out Along Crystal Boundary; 5) Phase Begins to Separate Out Everywhere; 6) Phase Formation; 7) Minute.

High temperature section: during the period of isothermal transformation, the metastable  $\beta$  phase sees the direct separating out of  $\alpha$  phase. Its characteristics are to initially form crystal boundary  $\alpha$ , and, subsequently give rise to the formation of a Widmanstätten  $\alpha$  feature inside the crystal. See Figure 3(a). Following a drop in temperature, the number of crystal gradually decreases and the amount of dispersion of  $\alpha$  in the crystals increases. At the same time, the amount of  $\beta$  phase remaining in the structure also shows reduction (corresponding to the equilibrium structure at various temperatures). Compare Figure 3(b) and 3(c). Speaking in terms of dynamics, the 550 degree centigrade transformation is the fastest, with a "breeding" period of approximately two minutes. On the basis of electron diffraction analysis of selected areas, the  $\alpha$  phase formed in these temperature regions corresponds to the Burgers relation, that is,  $(0001)_\beta // (110)_\alpha$ ,  $[11\bar{2}0]_\beta // [\bar{1}11]_\alpha$ . Because of this, it belongs to I type. In the tested temperature range, there was no appearance of II type. See Figure 4.

In the medium temperature range (350-400 degrees Centigrade), /274 the speed of the decomposition rate of the  $\beta$  phase takes an obvious drop. After 16 hours of isothermal heat treatment at 400 degrees Centigrade, it is still single phase  $\beta$ . It is only after 50 hours that the interior of crystals begin to show clear formation of snow flake form  $\alpha$ . The fine structure of this is very different from a high temperature Widmanstätten. The latter presents a single chip form; moreover, snow flake form is an agglomeration formed from numberless high temperature diffused point form  $\alpha$ . See Figure 5. This is similar to the "raft" form  $\alpha$  which is discussed in reference (5) and clearly shows that the formation structure already shows transformation.





(a) 650°C 1 小时 (b) 650°C 500 小时 (c) 550°C 1000 小时

Fig.3 Optical micrographs of isothermally treated TB2 alloy in the higher temperatures

a = 650°C for 1 hr.                      b = 650°C for 500 hrs.  
c = 550°C for 1000 hrs.

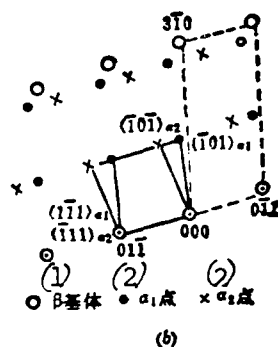


Fig.4 Selected area diffraction pattern corresponding to Fig.3(c), [133] zone

Key: 1 - cell      2 - point

In the low temperature region (250-300 degrees Centigrade) the phase which separates out shows a uniform distribution of point forms. Through the use of electron diffraction on selected areas, it is possible to determine that the products which separate out have a six-sided form and are of the  $\omega$  phase; their orientation is related by the expression  $(2110)_\omega // (110)_\alpha$ ,  $(0001)_\omega // [111]_\alpha$ . See Fig. 6.

After 50 hours of isothermal treatment at 300 degrees Centigrade, there is already the appearance of a  $\omega$  phase. When the temperature is 250 degrees Centigrade, the formation speed of the  $\omega$  phase is slowed down. It is only after 100 hours that one sees the formation of a  $\omega$  phase.



400°C 50 hrs. 5000x

Fig.5 Contrast of internal  $\alpha$  morphologies precipitated at medial and high temperatures

Fig. 7 shows the curves for transformations in hardness after isothermal treatment of TB2 alloy wire stock. This graph figure shows that the hardness values of the alloy vary with the transformations in the structure. In the low temperature section, the rate of hardening is very low. After 100 hours at 250 degrees Centigrade, the hardness begins to show changes. After 250 hours, the increase is abrupt. This is when there is a large scale appearance of the  $\alpha$  phase. When the temperature is relatively high, the rate of speed of the hardening increases over time. However, it still requires more than 100 hours, and, it is only then that it is possible to reach the peak values of hardness or enter into a stable phase. This requires a much longer duration of time effects than is actually employed in production.

Another question worthy of consideration is whether or not, since the alloy contains chromium, it will give rise to general separation transformations during long exposures to additional heat, that is,  $\beta \rightarrow \alpha + \text{TiCr}_2$ ; moreover will this lead to making materials brittle? Within the range of these tests, structural analysis has not yet shown the appearance of a  $\text{TiCr}_2$  phase, which shows that TB2 alloy has excellent heat stability characteristics.

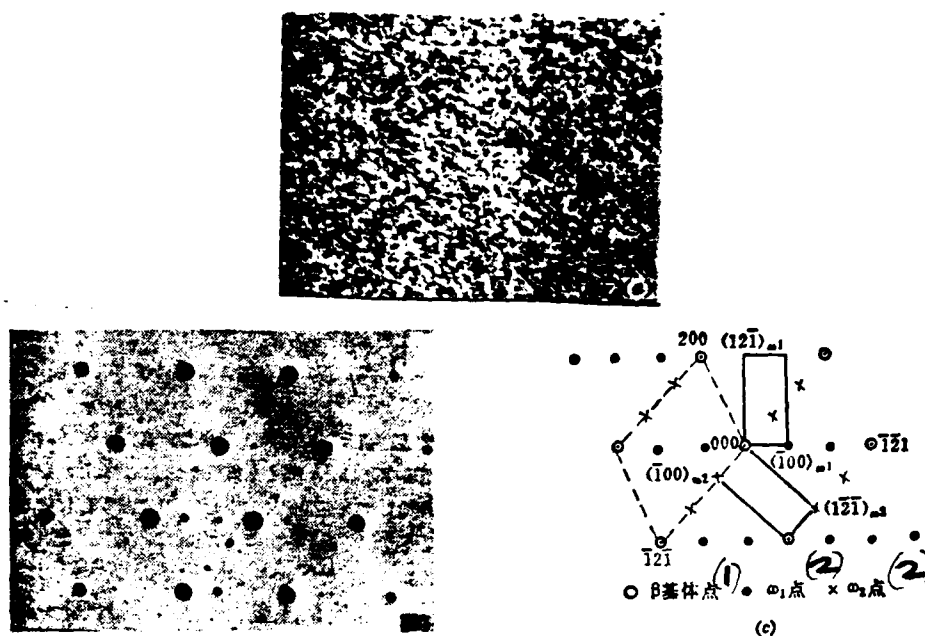


Fig.6 Light field TEM micrograph and electron diffraction pattern of isothermally treated TB2 at 250°C for 1000 hrs, [012] zone

Key: 1) Basic Body Point; 2) Point.

1. Basic Body Point 2. Point

## 2. Time Effect Treatment

After TB2 alloy wire stock goes through 30 minutes of 800 degree Centigrade heat treatment with water quenching, and time effect treatment is carried out at temperatures 250-650 degrees Centigrade, the longest treatment period reached 500 hours. During the time effect process, the decomposition characteristics of the  $\beta$  phase and the isothermic changes in the basic body were the same. The product of high temperature time effect transformation is  $\alpha$  phase. At low temperature (300 degrees Centigrade and below), it is  $\omega$  phase. The rate of speed of decomposition increases. All C curves are displaced to the left. See

Fig. 8. There are also increases in the degree of diffusion of phases which appear. These types of phenomena also appear in other types of phase alloys. It can be inferred that there is a relationship between increases in the concentration of the quenching and the occurrence of early precipitation of the  $\beta$  solid solution during time effect heat increases.

During the time effect process, the changes in hardness were exactly the same as the times of the isothermic transformations. Among these, the rate of hardening during time effect processing at 550 degrees Centigrade was the fastest. After 8 hours of time effects, the hardness had already approached a peak value. The time effects on the alloy at 650 degrees Centigrade lie in the over time effected state; moreover, time effects below 500 degrees Centigrade had rates of hardening which were relatively low. At 100 hours, the hardening had still not reached a peak value. In current industrial practice, workers employ values in the range of 8 hours of time effects at 500 degrees Centigrade. From the point of view of structure and hardness both, these products have still not entered into a stable phase, and this problem is worthy of more research.

/276

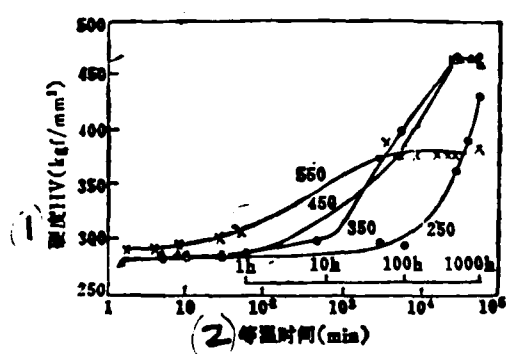


Fig. 7 Relationship among hardness isothermally treated temperatures and times

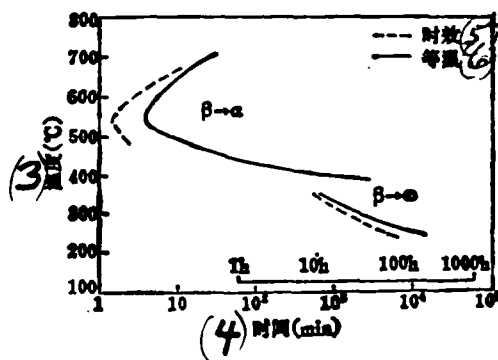


Fig. 8 Curves of isothermal and aging transformation kinetics in TB2 alloy

Key: 1) Degree of Hardness; 2) Isothermic Period;  
3) Temperature; 4) Duration; 5) Time Effects; 6) Isothermic.

### 3. The Influence of Solid Solution Temperature and Cooling Speed on Time Effect Structure

In the tests, we respectively chose 900 degrees Centigrade, 800 degrees Centigrade and 730 degrees Centigrade to carry out solid solution treatment. Subsequently, we applied 25-100 hours of time effects at 550 degrees Centigrade in order to make a comparison of the differences in time effect values. Among these, at 730 degrees Centigrade, in the two phase areas  $\alpha + \beta$ , Fig. 9 shows the phase hardness curves, and, from these we can see that the rate of time effect hardening for solid solution treatment at 730 degrees Centigrade was relatively high. However, the ultimate hardening effects were not comparable to those from solid solution treatment of  $\beta$  areas. Structurally speaking, the quenching structure of two phase areas, due to the fact that there exist small amounts of initially produced  $\alpha$  phase, the phase boundary surfaces are priority nucleation sites, which favors the subsequent formation of  $\alpha$  phase. Therefore, time effect hardening is relatively fast. However, the overall amount of  $\beta$  phase decomposition drops, which leads to peak hardening values being relatively low. By the same token, these tests prove that dropping the quenching speed, for example, by using air cooling, will also weaken the time effect hardening reaction.

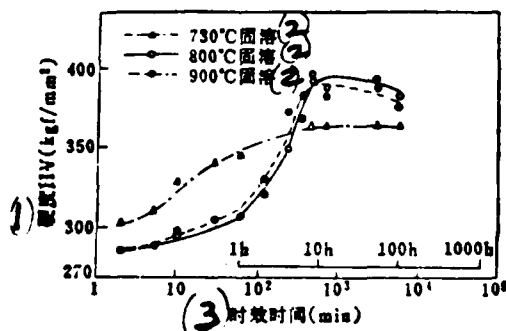


Fig. 9 Effect of solution-treatment temperatures on aging hardness

Key: 1) Hardness; 2) Solid Solution  
3) Time Effect Duration.

#### 4. Other Influencing Factors

The different raw materials in furnaces, due to differences in the actual chemical constituents and industrial processing techniques, has obvious effects on the dynamics of time effects. For example, in the case of a furnace of TB2 plate stock (containing 0.13% oxygen), the speed of decomposition of its  $\beta$  phase is much lower than the same alloy but in wire stock (same furnace but containing 0.18% oxygen). Oxygen belongs to the factors which contribute to stabilization. If there is a lowering of the stability of the  $\beta$  phase, this promotes the appearance of  $\alpha$  phase, but has an unclear influence on the range of standard components in the  $\alpha$ - $\beta$  type alloy. However, one cannot overlook its effects on  $\beta$  type alloy either. Besides this, the influence of the speed of time phase heat increases must also be considered. If one slowly increases the speed, due to the early precipitation of the  $\beta$  phase solid solution, this leads to the ultimate speeding up of the process of time effect separation of phases. This also raises the diffusion and uniformity of subsequently produced  $\alpha$  phase. All this means that the great sensitivity of industrial processes to the time effect structure of high strength  $\beta$  phase alloy is worth further, deeper research.

#### 4. Conclusions

1. We specified the initial positions of the isothermal transformation curves for TB2 alloy stock. Between 400 and 700 degrees Centigrade, this alloy has a metastable  $\beta$  phase which gives direct rise to an  $\alpha$  phase. The orientation relationship between the two phases is, and corresponds with the  $(11\bar{2}0)_\beta // (111)_\alpha$ ,  $(0001)_\beta // (110)_\alpha$ .  
Burgers relationship. Within the range of these tests, TB2 alloy, after

/277

long duration, high temperature isothermal exposures, has yet to give rise to any finely distributed transformation products.

TB2 alloy, during long duration isothermal exposure at 250-300 degrees Centigrade, gives rise to the transformation  $\beta \rightarrow \alpha$ . Its orientation relationship is  $(0001)_\alpha // (111)_\beta$ ,  $(2110)_\alpha // (110)_\beta$ .

2. We determined the time effect transformation curves for TB2 alloy wire stock, and, when compared with isothermic transformations, these curves are shifted to the left.

3. Increases in quenching temperature or quenching speed seem to be beneficial to the  $\beta$  phase decomposition during the time effect process.

4. Variations in the actual chemical composition of the alloy as well as the speed of time effect temperature increases have a clear influence on the decomposition rate of metastable  $\beta$  phase, and are important factors in the control of time effect structure.

Others who have participated in this research are XIE Xi-wen, LIANG You-ming, and Comrade LI Chun-zhi.

Besides this, the raw materials were donated by Laboratory 202 of Non-ferrous Metals General Research Institute; moreover, in these tests, we have gotten the spirited help of the engineers, CHEN Hai-shan and ZHANG Zhu from this same institute, and we desire to express our heartfelt gratitude.

#### REFERENCES

- [1] Non-Ferrous Metals Research Institute. "Introduction to Two New Temperature Parameters and Rare Metals in the  $\beta$  Phase Titanium Alloy", TB2, (1979), Vol. 1.1.
- [2] Naik, Uma M., Omega and alpha precipitation in Ti-15Mo alloy, proceedings of the Fourth Inter. conf on titanium, (1980), 1335.
- [3] Toran, J. R., Biederman R. R., Phase Transformation Study of Ti-10V-2Fe-3Al, *ibid*, 1571.
- [4] de Fontaine, D., *Acta Met.*, (1970), 18, 275.
- [5] Williams, J. C., *Critical Review in Titanium Science and Technology*, (1973), V.3, 1433.
- [6] Rhodes, C. G., and Paton, N. E., The Influence of Microstructure on Mechanical Properties in Beta C Met. Trans., 8A, (1977), 1749.

EFFECT OF REFINING ELEMENTS ON DENDRITE  
ARM SPACING OF Al-5.0Cu-0.8Mn ALLOYS

/279

CHU Yanhe and XU Cailu.

(Beijing Institute of Aeronautical Materials)

ABSTRACT

The effects of the cooling rate and the added elements Ti, B, V, Zr on the dendrite arm spacing and grain size of the Al-5.0Cu-0.8Mn alloy are investigated. The results show that the enhancement of the cooling rate decreases the dendrite arm spacings of the alloy, and at the same cooling rate the addition of the refining elements such as Ti, B, V, Zr narrows the solute-rich band in the solid-liquid interface because the elements restrain the growth of the dendrite. In result, the dendrite arm spacing and grain size are refined significantly, and the sensitivity of the dendrite arm spacing to the cooling rate is reduced.



## SUMMARY

This article researches the influence of cooling speed and the presence of the elements titanium, boron, vanadium and zirconium on the crystal grain dimensions of Al-5.0Cu-0.8Mn alloy and subsequent dendrite arm spacing. The raising of cooling temperature speeds reduces the spacing between secondary dendrites. In cases where the cooling conditions are held constant, after the addition of refining elements such as titanium, boron, vanadium, zirconium and others, because of the restraining effect on the formation of dendrites, there is a contracting effect on the solute rich areas along the front of the solid-liquid boundary surface, and there is a clear refining effect on the dimensions of crystal grains and the spacing of secondary dendrite arms. Moreover, there is a lowering of the sensitivity of secondary dendrite spacing to cooling speed.

### 1. Preface

There is a clear relationship between secondary dendrite spacing in cast alloys and their mechanical characteristics. The main elements influencing the spacing of secondary dendrites are the speed of cooling and the concentration of the solute (1). In hypocrystalline aluminum-copper binary alloy, an increase in the amount of contained solute causes a reduction in the spacing of secondary dendrites. An increase in the speed of cooling also causes a reduction in the spacing of secondary dendrites. Moreover, changes in the amounts of solute contained do not change the effects of cooling speed (2-4).

This article explores the influence of the presence of the trace elements titanium, boron, vanadium, and zirconium on the spacing of secondary dendrites in cast alloys and on the speed of cooling.

## 2. Testing Methods

The alloy constituents used in these tests are as set out in Table 1. We made use of high purity aluminum in the construction of the alloy casting test plate. On a 210x160x20 mm test plate, at one end was put a 170x90x50 mm piece of graphite cold steel, and, on the other end was set up a vent. At a 710 degrees Centigrade casting temperature, one is able to attain the normal ingot formation cooling speed (10 degrees Centigrade/minute to 200 degrees Centigrade/minute). On the basis of cooling curves obtained from thermoelectric dipole measurements of the test plate surface, it was possible to calculate the cooling speeds of particular points. Using the straight line cutting method (5,6), we measured the spacing of secondary dendrites and the dimensions of crystal grains. Every point measured was an average value of measured numerical data taken from a minimum of four cutting curves.

Table 1 The composition of experimental alloys

(1) Alloy	(2) Cu, wt. %	(3) Mn, wt. %	(4) Ti, wt. %	(5) B, wt. %	(6) V, wt. %	(7) Zr, wt. %
Nb 1	4.50	—	—	—	—	—
Nb 2	4.85	0.84	—	—	—	—
Nb 3	4.96	0.78	0.20	—	—	—
Nb 4	4.71	0.80	0.13	0.03	0.13	0.095

Key: 1) Alloy; 2) Copper; 3) Manganese; 4) Titanium; 5) Boron; 6) Vanadium, 7) Zirconium.

On the JCYA-733 Model electron probe X-ray microanalyzer, we made measurements of the amounts of copper contained within the crystal dendrites and on the forward edge. These efforts were assisted by metallographic and manual microoptical measurements of the length and width of primary and secondary dendrites.

### 3. Test Results

We carried out regressive analysis of the measured amounts obtained for the cooling speed  $V_c$  and the secondary dendrite spacing (DAS), and we obtained DAS and  $V_c$  relationships for different components as shown in Fig. 1.

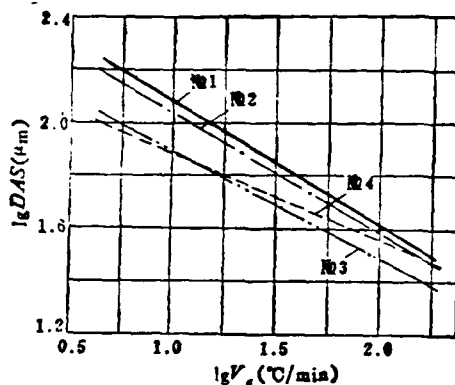


Fig. 1 Relationship between dendrite arm spacings and cooling rate of some aluminium alloys

No. 1  $\lg DAS = 2.5457 - 0.4655 \lg V_c$   $\gamma = -0.9994$

No. 2  $\lg DAS = 2.4853 - 0.4497 \lg V_c$   $\gamma = -0.9685$

No. 3  $\lg DAS = 2.3768 - 0.4370 \lg V_c$   $\gamma = -0.9936$

No. 4  $\lg DAS = 2.2122 - 0.3246 \lg V_c$   $\gamma = -0.9967$

$\gamma$  为相关系数 (1)

Key: 1) is the phase relationship coefficient.

Table 2 sets out the various alloys' secondary dendrite spacing (DAS) and their crystal grain dimensions (GS) given different cooling speeds.

From Fig. 1 one can see that the addition of manganese, titanium, boron, vanadium, zirconium and other such alloy components causes the secondary dendrite spacing of aluminum-copper alloy to be clearly reduced. At the same time, the influence of the rate of slope of the curve describing the relationship between the presence of manganese and the speed of cooling as well as the spacing of secondary dendrites is not

large. Moreover, the clear reducing influence which the presence of boron, vanadium, zirconium and other such trace elements have on the cooling speeds and on the spacing of secondary dendrites as well as the similar influence which they have on the dimensions of crystal grains are both obvious.

Table 2 DAS and grain size of alloys at various cooling rates

Vc, °C/min	140.29		105.15		84.10		66.29		31.25		24.28		16.24	
合金	GS	DAS	GS	DAS	GS	DAS	GS	DAS	GS	DAS	GS	DAS	GS	DAS
	mm	μm	mm	μm	mm	μm	mm	μm	mm	μm	mm	μm	mm	μm
№1	0.704	35.0	0.715	40.0	—	45.0	0.795	50.0	—	70.0	1.132	79.0	0.734	98.0
№2	0.838	32.5	0.914	35.0	0.911	38.0	0.994	42.0	1.069	74.0	0.902	78.0	0.863	84.0
№3	0.448	28.0	0.531	30.0	0.433	32.0	0.542	36.0	0.419	54.5	—	60.0	0.453	71.5
№4	0.146	32.0	0.231	35.0	0.228	39.0	0.211	42.0	0.281	55.0	0.297	58.0	0.256	65.0

Key: 1) Alloy; 2) Numerical Data.

In order to do a more in-depth analysis of the influence which constituent elements such as manganese, titanium, boron, vanadium, zirconium, and so on, have on the formation of dendrites under different cooling speed conditions, we measured the various characteristic dimensions of dendrites under various conditions. The results are shown in Fig. 2-5. Manganese does not influence the expansion in the direction of primary crystals. Titanium, boron, vanadium, and zirconium have a clear restraining effect on the growth of primary crystals. They also have a restraining effect on the formation of secondary dendrites. However, this influence is not as large as that on primary crystals.

AD-A179 673

ACTA AERONAUTICA ET ASTRONAUTICA SINICA(U) FOREIGN  
TECHNOLOGY DIV WRIGHT-PATTERSON AFB OH 07 APR 87  
FTD-ID(AS)T-1246-85

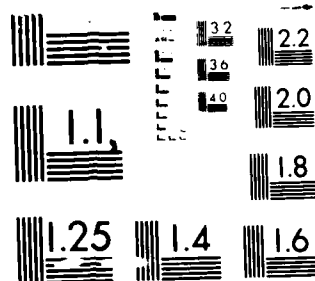
3/3

UNCLASSIFIED

F/G 13/8

NL

END  
DATE  
FILMED  
5-87  
DTIC



MICROCOPY RESOLUTION TEST CHART  
NATIONAL BUREAU OF STANDARDS-1963-A

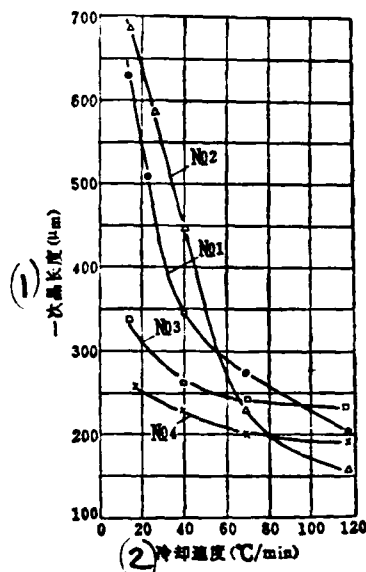


Fig. 2 Effect of added elements and cooling rate on the length of the primary dendrite

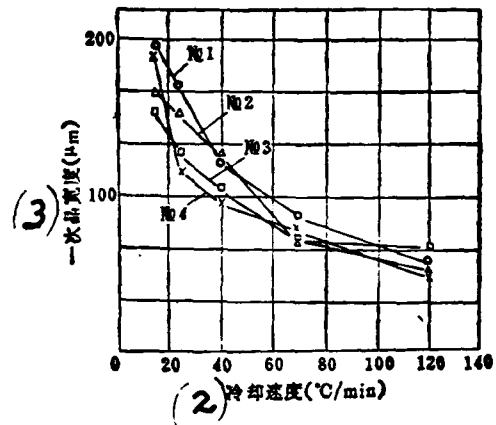


Fig. 3 Effect of added elements and cooling rate on the width of the primary dendrite

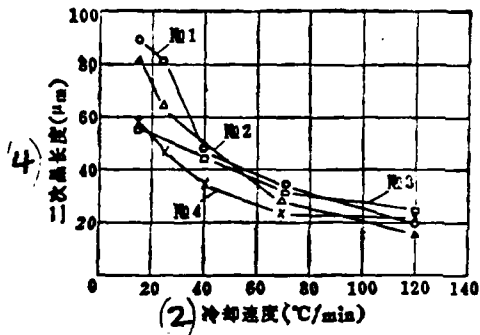


Fig. 4 Effect of added elements and cooling rate on the length of the secondary dendrite

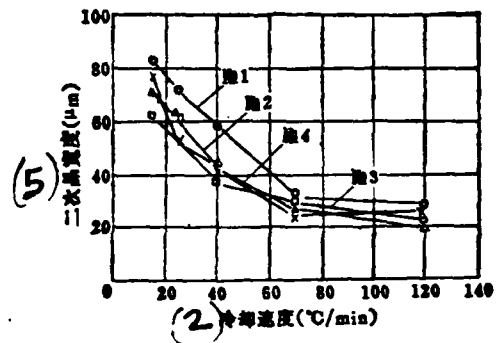


Fig. 5 Effect of added elements and cooling rate on the width of the secondary dendrite

Key: 1) Primary Crystal Length; 2) Cooling Speed; 3) Primary Crystal Width; 4) Secondary Crystal Length; 5) Secondary Crystal Width.

Fig. 3 sets out the results of measurements of the amounts of copper contained at various positions in crystal dendrites as obtained through the use of electron probe analysis. Fig. 6 is a display chart of the measurement test points of the probes. From this chart we can see that there are obvious changes in the amounts of contained copper from one position to another. We also did analyses of the amounts of titanium, manganese, vanadium, and zirconium, but, we observed no clear changes in their levels.

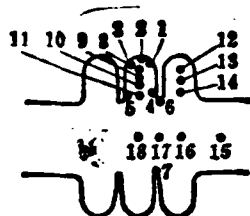


Fig. 6 The schematic diagram for electron-probe measuring points

Table 3 The copper content at the center and on the side of secondary and primary dendrite by electron probe x ray microanalyzer

(1) 冷 却 速 度		二次枝晶間距		合金號數		宏觀銅含量		(5) 探針分析銅含量, wt. %																	
°C/min		mm		(3) 號 號		(4) %		(6) 枝 晶 前 緣							(7) 二 次 晶 中 間							一 次 晶 中 間 (8)			
								1	2	3	4	5	6	7	8	9	10	11	12	13	14	15	16	17	18
15	98	№ 1	5.14	4.41	4.46	4.59	4.02	4.23	4.50	3.35								1.77				1.04	1.19	1.06	1.07
	84	№ 2	5.30	4.80	4.64	5.09	4.44	4.75	4.73									1.71						2.24	
	71.5	№ 3	5.10	4.95	4.73	4.26									3.59	2.57	2.28	2.12	4.65	2.59	1.79	1.38	1.31	1.56	1.66
120	38	№ 1	5.19	3.07	3.58	4.89	2.98	3.25	3.26	3.58								1.67				2.10	1.55		
	34	№ 2	5.14	4.20		5.08	3.24	2.96	3.93									3.73				2.69	2.26	3.15	2.01
	30	№ 3	5.24		4.56	4.19		3.55	4.12					4.74	4.34	3.78			3.58			2.29	2.06	2.18	
	34	№ 4	5.04	3.95	3.70	3.26			3.43					4.39	4.46	4.21		4.33	4.42	4.39	1.37	1.57	1.43	1.44	

Key: 1) Cooling Speed; 2) Secondary Dendrite Spacing; 3) Alloy Number; 4) Overall Copper Content; 5) Probe Analysis Copper Content; 6) Dendrite Forward Edge; 7) In Secondary Crystals; 8) In Primary Crystals.



#### 4. Analysis and Discussion of Test Results

During the process of alloy congealing, at the same time the primary rod is being created, the secondary rod is also being formed. Because of this, these formations are cyclical (7). Formation of the secondary branch rod causes the inducing of a rich concentration of solute in the vicinity ( $K_0 < 1$ ). This must necessarily influence the surrounding branch rods in their formation.

After a secondary branch is formed on a primary one, the area of rich solute concentration along the liquid-solid boundary surface is as shown in Fig. 7. When the speed of cooling is increased, the area of rich solute concentration along the forward edge of the boundary surface declines sharply in size. The  $\delta$  value in Fig. 7 will drop, because of the fact that a secondary branch rod in the vicinity is formed at the nearest position outside the  $\delta$  area. Therefore, if we take an extremely small value of  $\delta$ , then, after congealing, secondary dendrite spacing will be extremely small.

The results of testing show (Fig. 2-5) that, under the same conditions of congealing, after alloy elements such as titanium, boron, vanadium, zirconium, and so on are added to aluminum-copper alloy, not only are the length and width of primary crystals reduced, but so are the length and width of secondary crystals as well. This goes to show that, at the same speeds of cooling, the formation of dendrites has been restrained. The amount of copper atoms removed from the liquid-solid boundary surface is reduced, as is the rich solute concentration area along the front boundary surface, that is,  $\delta$ . (Fig. 7) is reduced. Because of this, there is a refining of secondary dendrites.

The results of electron probe measurements show (Fig. 3) that, after the addition of titanium, boron, vanadium, and zirconium, the amount of copper contained in the interior of secondary dendrites was clearly reduced. That is to say that, during congealing, the amount of copper atoms removed from the boundary surface is small. The  $\delta$  value in Fig. 7 is clearly reduced. Besides this, due to the fact that the area of rich solute concentration on the forward boundary surface is small, the

change of  $\delta$  which is caused by changes in cooling speed is also small, that is, the sensitivity of secondary dendrite spacing to cooling speed is small. /283

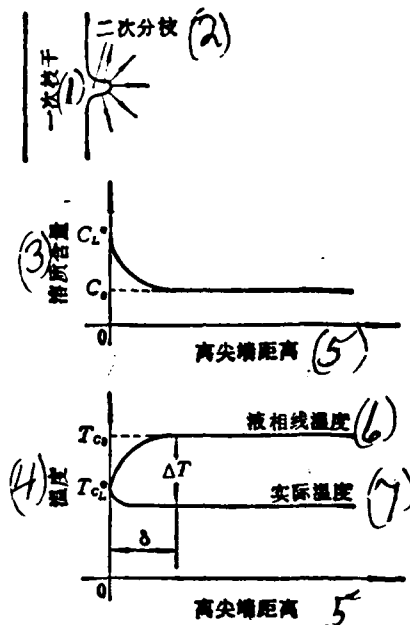


Fig.7 Solute-rich band causing the change of the liquidus and supercooling

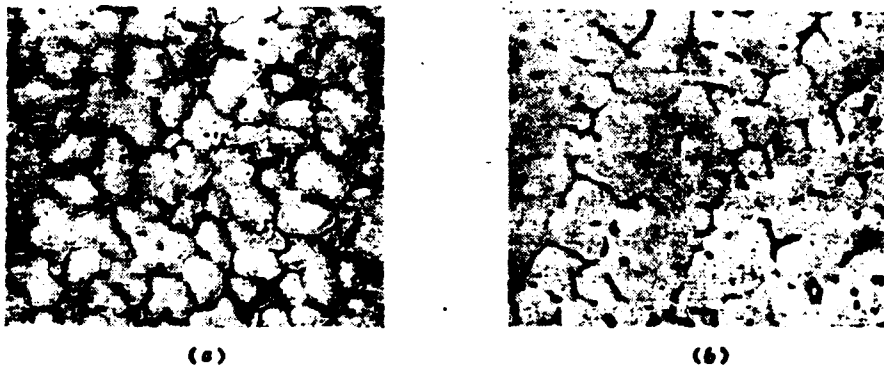


Fig.8 The effect of added elements on structure  
(a) Al-4.5Cu; (b) Al-4.5Cu-0.8Mn-BVZr.

Key: 1) Primary Branch; 2) Secondary Branch; 3) Amount of Solute Contained; 4) Temperature; 5) Distance from the Sharp End; 6) Liquid Phase Line Temperature; 7) Actual Temperature.

When the refining effects from the addition of refining elements are sufficiently strong, and, under conditions of rapid cooling, the production of secondary (or higher order) dendrites is halted, it causes crystal grains to tend toward a globular shape as shown in Fig. 8.

## 5. Conclusions

1. The addition of titanium, boron, vanadium, zirconium, and other such elements to Al-5.0Cu-0.8Mn alloy not only has a refining effect on the spacing of secondary dendrites, but, it also lowers the sensitivity of secondary dendrite spacing to the speed of cooling.

2. After the addition of refining elements to aluminum-copper binary alloy, the spacing of secondary dendrites and the speed of cooling are still in a very good direct relationship.

3. The addition of refining elements to alloys restrains the formation of primary and secondary crystals, which makes the original long rod-shaped crystals of the aluminum-copper alloy tend toward a ball shape.

## REFERENCES

- [1] Horwath, J. A., Mondolfo, L. F., Dendritic Growth, *Acta Metallurgica*, vol. 10, Nov., (1962), pp1037-1042.
- [2] Dann, P. C., Eady, J. A., Hogan, L. M., Dendrite Arm Spacings in Aluminum-Rich Alloys, *J. of the Australia Institute of Metals*, vol. 19, No.2-June(1974), pp140.
- [3] AN Ge ying, TANG Duo gwang; LI Qing chun. "Dendrite Structure of AL-Cu Alloy Under Directional Solidification Conditions", *Modern Casting*, No. 2, 1982, p. 24.
- [4] Alexander, B. H., Rhines, F. N., *Trans. AIME*, vol. 188, (1950), pp1267-1273.
- [5] Oswalt, K. J., Misra, M. S., Dendrite Arm Spacing (DAS), A Nondestructive Test to Evaluate Tensile Properties of Premium Quality Aluminum Alloy (Al-Si-Mg) Castings, *AFS, Trans.*, vol. 88, (1980), pp845-859.
- [6] Radharishna, K., Seshan, S., Seshadri, M. R., Dendrite Arm Spacings in Aluminum Alloy Castings, *AFS, Trans.*, vol. 88, (1980), pp695-702.
- [7] Chalmers, B., *Principles of Solidification*, (1964).

AN INVESTIGATION OF ION IMPLANTATION IN COPPER ALLOYS  
FOR IMPROVING THEIR WEAR RESISTANCE

/285

WANG Yi hua, WEN Meng quan, WANG Zheng xiang, JIANG Ji feng

(Beijing Institute of Aeronautics and Astronautics)

ABSTRACT

This paper deals with the ion implantation in ZQSn10-2-3 copper alloy and describes how the wear resistance of the alloy is thus improved.  $N_2^+$  and  $Ag+N_2^+$  ions are implanted in silver-plated and non-silver-plated copper alloys, respectively. The ion-implanted surface layers are analyzed with a backscattering device, an ion probe and a scanning electron microscope.

The results show that the friction factor of the silverplated copper alloy decreases about 40% and the abrasion value reduces by a factor of 2 at a 700m sliding distance after the  $N_2^+$  implantation. For the non-silver-plated samples, a new alloy is formed at the ion-implanted surface. Its microhardness increases about 56% and its abrasion value decreases by a factor of 37.5 at a 700m sliding distance. It is also testified that the finish of the sample surface is not affected in the process of ion implantation.

## SUMMARY

This article deals with the surface form of the tin-bronze compound ZQSn10-2-3, in specimens of both the silver-plated and non-silver-plated form. It was decided to separately make use of  $N_2^+$  ions and  $(Ag+N_2^+)$  ions for implantation using the beam mixing technique, in order to make improvements in the surface, specifically, to raise its resistance to abrasion. Moreover, use was made of backscattering radiation equipment, ion probes and scanning electromicroscopy to carry out measurements and analyses of the implantation layer. The results of these tests show that specimens with the ion implantation and ion beam mixing significantly raised their capability to resist abrasion losses.

### 1. Test Methods (1-7)

#### 1. Preparation of Specimens

The material of the specimens was ZQSn10-2-3 tin-bronze in two varieties, silver-plated ( thickness approximately  $15\mu m$  ) and non-silver-plated. The dimensions of the specimens were 40x5 mm diameter, with a surface luminosity of  $\nabla 11$  , and a surface unevenness of  $\leq 0.005 mm$ .

#### 2. Ion Implantation Conditions

(1) Silver-plated specimens: implantation  $N_2^+$  ; amount of power 150keV; amount of agent  $2 \times 10^{17} N_2^+ / cm^2$ .

(2) Non-silver-plated specimens: use made of the ion beam mixing technique. This involved the initial use of evaporation and accumulation of the settled material in a vacuum, which was approximately 500 A silver membrane. After this, we made use of 140keV,  $5 \times 10^{16} N_2^+ / cm^2$  nitrogen ions and bombarded the specimens. In order to strengthen the effects of the ion beam mixing, we repeated the process described above. Moreover, we took the energy level of the  $N_2^+$  and raised it to 150keV. We then carried out double ion beam mixing.

### 3. Measurement and Analysis Methods

Friction and abrasion testing were carried out on a needle plate -type abrasion test instrument. The material of the grinding needles was 2 mm diameter GCr15 steel, and the tips of the needles were of a rounded arc shape. The samples for these tests were round grinding plates. At room temperature, with no lubrication factor, we measured the amount of abrasion loss and the coefficient of friction for the samples. Moreover, we also made use of a microhardness meter and a microinterferometer to measure, respectively, the microhardness and surface luminosity of the samples. We also made use of scanning electron microscopy to observe the form of the abrasion injured surfaces. In addition, we used backscattering radiation equipment and ion probes to carry out ion implantation layer constituent and depth analyses.

### 2. Results of Capability Measurements

In the case of both ion implanted and ion non-implanted specimens, the average measurement results of amounts of abrasion loss and luminosity, under varying abrasion testing conditions, are as shown in Table 1. The scanning electron microscopy photographs of the abrasion injured surface forms are shown in Fig. 1.

/286

One can see from the test results above that the average abrasion loss amounts for the two types of ion implant specimens, both show different degrees of decline. When the test speed is 12.67 m/min and the sliding distance is 700m, the average amount of abrasion loss for samples implanted with  $N_2^+$  is 0.10mg. When we compare this to the specimens without ion implantation, we see that the average values for amounts of abrasion loss are reduced by 1/3. Under the same abrasion conditions, the samples which had undergone  $(Ag+N_2^+)$  ion beam mixing had an average value for amount of abrasion loss of 0.2 mg. When we compare this with the specimens which had not undergone the ion beam mixing, the average amount of abrasion loss was reduced to 2/77. When the testing speed was raised to 16.29m/min, and the sliding distance was

increased to 1000m, the corresponding average values for amount of abrasion loss were reduced, respectively, to  $2/5$  and  $2/3$ . This is due to the fact that, when the abrasion channel is increased in depth, the concentration of implanted ions is lowered.

When we compare the size of average abrasion losses in various types of specimens under differing test conditions, it is possible to see that, when the surface formation is from a specimen which has been silver-plated and implanted with nitrogen, the average amount of abrasion loss is smaller than that for specimens which have undergone ion beam mixing. This is due to the fact that the abrasion resistance of the silver-plated, nitrogen ion implanted specimens is better.

From the scanning electron microscopy photographs, it is possible to see that, after abrasion testing of specimens which had not undergone ion implantation, the abrasion channels were deep and coarse. The abrasion losses were uneven and variable in depth. Localized gouging was severe. In the case of specimens which had been ion implanted, the appearance of the abrasion channels was relatively smooth and even, and abrasion damage was fine and shallow. This demonstrates that, under similar test conditions, the capabilities of ion implanted materials to resist abrasion losses is relatively better.

The results of measurements of luminosity clearly show that the industrial technique of ion implantation will not lower the surface luminosity of products. It is possible to use this process as the final procedure in the surface processing of products. This is particularly advantageous in the strengthening treatment of aviation precision friction secondary surfaces.

/287

The abrasion resistance of metal materials and the coefficients of friction of the materials as well as their hardnesses are all related. Generally speaking, it is possible to make use of a lowered coefficient of friction and an increased hardness as a method to raise abrasion resistance. In these tests, when we made use of ion implantation techniques to alter the coefficients of friction and the hardnesses of material surfaces, we obtained results as presented below

(1) When silver-plated tin bronze specimens have not yet undergone ion implantation, we measure the coefficient of friction to be 0.46; however, after implantation with  $N_2$ , the coefficient of friction drops to 0.27, a drop of 40%.

(2) When tin bronze-specimens have not yet undergone ion beam mixing, we measure a microhardness of  $HM_s = 1990 \sim 2180 \text{ MPa}$ . After  $(Ag+N_2)$  ion beam mixing, that value is  $HM_s = 3150 \sim 3390 \text{ MPa}$ , an approximate increase of 56%.



Table 1 The measured results of wearing test and finish

(1) 样 品	ZQSn10-2-3 锡青铜 (2) 表 面 被 镀				ZQSn10-2-3 锡青铜 (5) 表 面 未 被 镀			
	(3) 注入 $N_2^+$	(4) 未 注 入	(6) $(Ag + N_2^+)$ 离子束混合		(7) 未离子束混合			
(8) 载荷 (g)	81	81	81		81			
(9) 试验速度 (m/min)	12.67	16.29	12.67	16.29	12.67	16.29	12.67	16.29
(10) 磨损时间 (min)	55	62	55	62	55	62	55	62
(11) 磨程 (m)	700	1000	700	1000	700	1000	700	1000
(12) 平均磨损量 (mg)	0.10	0.18	0.30	0.44	0.20	7.30	7.70	11.03
(13) 表面不平度平均高度 ( $\mu m$ )	0.23		0.24		0.17		0.28	
(14) 光 洁 度	$\nabla 11$		$\nabla 11$		$\nabla 12$		$\nabla 11$	

Key: 1) Specimen; 2) Tin Bronze, Surface Silver-plated;  
 3) Implant; 4) Not Implanted; 5) Tin Bronze, Surface Not Silver-plated;  
 6) Ion Beam Mixing; 7) No Ion Beam Mixing; 8) Loading;  
 9) Test Speed; 10) Abrasion Loss Time; 11) Slide Distance;  
 12) Average Amount of Abrasion Loss; 13) Surface Unevenness and Average Height;  
 14) Luminosity.



Fig 1 SEM photograph of the topography of the wearing tracks of samples  
 (load, 81 g, speed, 12.67 m/min., sliding distance, 700 m)  
 (a)  $N_2^+$  implanted sample 500 $\times$ , (b)  $N_2^+$  unimplanted sample 500 $\times$ .

### 3, Physical Measurements and Analysis of Ion Implantation Layers

The fact that ion implantation raises the abrasion resistance of materials is closely related to the effects of the products which ion implantation produces in the surface layers of materials. In order to understand the special characteristics of ion implantation layers, we made use of ion probes and backscattering radiation energy spectrographic techniques to carry out on the surface layers of specimens measurements and analysis of the atomic composition, amounts of materials contained, and ion implantation depth.

#### 1. Composition and Depth Analysis of the Surface Layer of Ion Beam Mixing Specimens ( $\text{Ag}+\text{Ni}$ )

First of all, we made use of the LT-1A Model ion probe to measure the secondary ion mass spectrogram of specimens (SIMS). The primary ion source was  $\text{O}_2^+$ . The flow strength  $I=1\mu\text{A}$ . Accelerated electron pressure  $V=16\text{kV}$ . The degree of system vacuum was  $8 \times 10^{-7}\text{Torr}$ .

The secondary ion spectrograms which were obtained during the measurements in these experiments are as shown in Fig. 2. This chart outlines the relative strengths of the constituent elements and the various constituent ions of the surface layer after ion beam mixing ( $\text{Ag}+\text{Ni}$ ) is done on tin bronze specimens. These ions include  $\text{Ni}^+$ ,  $\text{Ni}^2+$ ,  $\text{Cu}^+$ ,  $\text{Ag}^+$ ,  $\text{Sn}^+$  and others of a similar kind. When there is a  $\text{Ni}^+$  bombardment of Ag membrane at an energy of 150ke, it produces violent flashes of radiation. On the main section of the 500  $\text{\AA}$  thick Ag membrane, the radiation strikes but is not absorbed. Only a small part strikes and enters the interior of the specimen body. It is because of this that, in the SIMS analysis, the  $\text{Ag}^+$  spectrum lines appear. Moreover, the results of backscattering analysis below demonstrate that there has been atomic

level mixing produced in the tin bronze body and the silver atoms. The surface has formed a new type of alloy, and, it is because of this that abrasion resistance of the material is raised. In the mass spectrogram, the appearance of the  $N_i$  spectrum lines as well as the vertical distribution of  $N_i$  concentration which was obtained from the ion probe (Fig.3) can be explained as the  $N_i$  "bomb" entering the surface layers of the specimen. Moreover, it has a definite distribution, and, in the strengthening of the surface, it has a definite effect.

/288

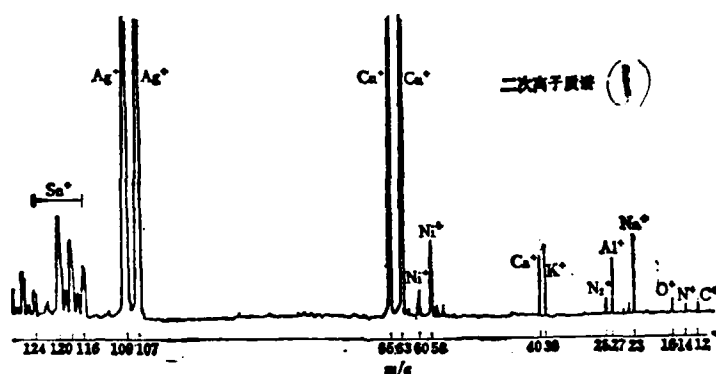


Fig.2 SIMS of the sample by ion beam mixing

Key: 1) Secondary Ion Mass Spectrogram.

In order to measure the depth distribution of silver atoms in the ion beam mixture specimen and its surface density (i.e., the number of silver atoms per unit area in the injection layer) we carried out a back-scatter energy spectral analysis (RBS).

The experimental conditions for the backscattering radiation analysis were as follows: the backscattering ion was  $He^{++}$ ; the radiation entry energy was  $E_0 = 2.4 \text{ MeV}$ ; stream mixing was  $T = 50 \text{ mA}$ ; beam spot was  $\phi = 1 \text{ mm}$ ; radiation entrance angle  $\theta_0 = 0^\circ$ ; scattering angle  $\theta = 165^\circ$ . The degree of system vacuum was  $10^{-5} \sim 10^{-6} \text{ Torr}$ . The path width of the multiple path analyzer was  $\delta E = 2.56 \text{ keV/ch}$ .

$M \approx 106 \text{ AMU}$ , . The backscattering energy spectragram which was obtained through these tests is as seen in Fig. 4. Except for the energy spectragram of the body of the tin bronze, at the high energy end, there appears a peak form spectragram. This is created by the backscattering which occurs when the  $^4\text{He}$  particles hit the heavier atoms of the specimen's main body. If one makes use of the backscattering spectragram in Fig. 4. it is possible to obtain the mass of the target atoms  $M \approx 106 \text{ AMU}$ . This numerical value is basically the same as that for the mass of the silver atoms ( $M_{\text{Ag}} = 107.868 \text{ AMU}$ ) . From this one can make the following analysis. The peak spectragram form in Fig. 4 is nothing else except the backscattering spectragram of the silver atoms in the ion beam mixing sample ( $\text{Ag} + \text{N}_2^+$ ) . In reality, it is formed from the superposition of two sharp peak spectragrams. These two sharp peak spectragrams correspond respectively to the two bombardment energies of  $\text{N}_2^+$ . According to the energy spectrum of the silver atoms, it is possible to calculate the depth of the vertical distribution of silver atoms in the surface layers of the specimens, that is, approximately  $2.7 \times 10^3 \text{ \AA}$ . Moreover, we also calculated the surface layer silver atom area density (it was consistent with a silver atom implantation reagent amount of  $1.7 \times 10^{18} \text{ Ag/cm}^2$  ).

Analysis of the backscattering calculations shows that, because of the ( $\text{Ag} + \text{N}_2^+$ ) ion beam mixing of two bombardments at differing energy levels, which were carried out on the samples of tin bronze, the depth distribution of the silver atoms was caused to reach  $2.7 \times 10^3 \text{ \AA}$ . . This is far greater than the thickness ( $500 \text{ \AA}$ ); of the Ag silver membrane. Moreover, the numerical value level of the silver atom surface density in the surface layers of the specimens reached  $10^{18}$ , . This caused high agent amount silver ion implantation effects. These two points caused a decisive effect in the increasing of the abrasion resistance of the copper alloy.

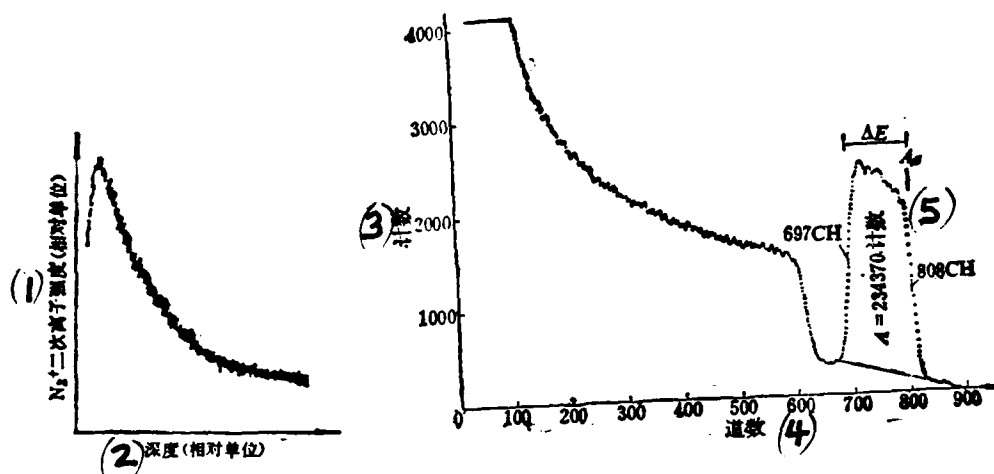


Fig.3 The depth distribution of  $N_2^+$  in the sample by ion beam mixing

Fig.4 RBS of the sample by ion beam mixing

Key: 1) Secondary Ion Strength (Corresponding Units);  
 2) Depth (Corresponding Units); 3) Numerical Calculations;  
 4) Path Number 5) A-234370 Numerical Calculation.

## 2. Secondary Ion Mass Spectrogram and Depth Analysis of Nitrogen Implanted Specimens

The surface structure of these specimens before ion implantation was an electroplated silver layer  $15\mu m$  thick. The objective of the SIMS analysis is to make a comparison of the degree to which the corresponding strengths of the various elements in the nitrogen implanted specimens follows changes in depth. In order to do this, we took, at the same sampling point in the specimens, surface and interior samples, and carried out four sampling analyses at differing depths. The secondary ion mass spectragrams which were obtained were as shown in Fig. 5(a)-(d) and reflect the fact that the corresponding strengths of various elements in the samples follow changes in depth. If one takes the spectragram lines in the Fig. and reduces them to 1/10 their size, then, it is possible to see that the corresponding strength of  $N_2$  ion implantation follows

increases and reductions in depth. The forms for these changes are roughly shown in the curves of Fig. 6(a). And, these patterns are the same as those obtained from the continuous depth analyses carried out using ion probe on the specific ion  $N_i$  as shown in Fig. 6 (b). The implantation of nitrogen ions had a special effect in causing an increase of the abrasion resistance of samples. /289

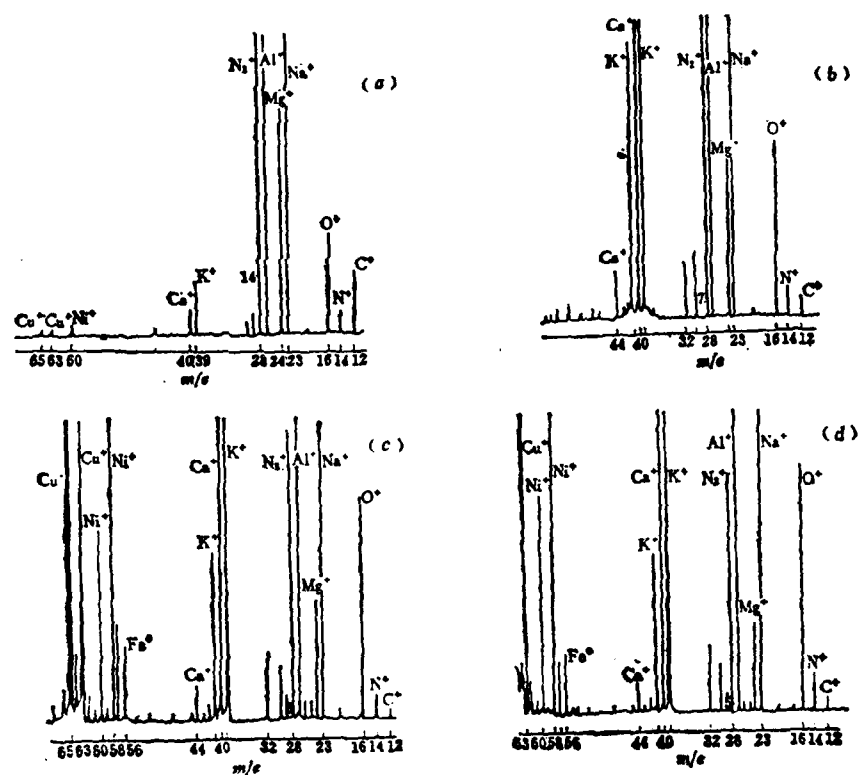


Fig.5 SIMS of nitrogen implantation sample(The comparison of depth distribution of different elements)

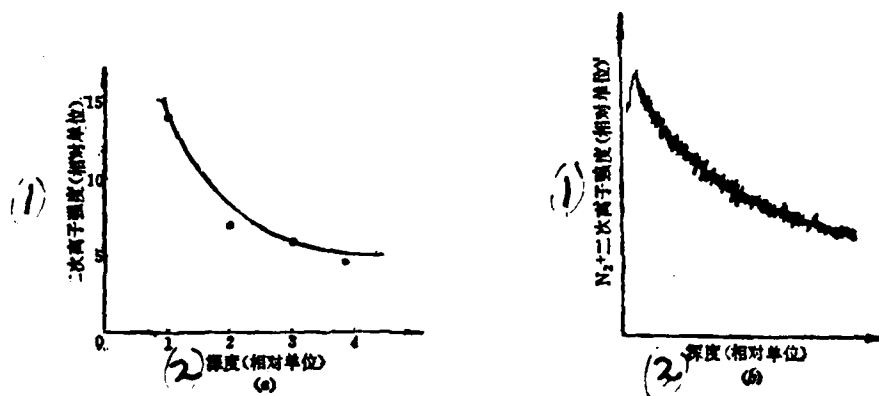


Fig. 6 The depth distribution of  $N_2^+$  in the nitrogen implantation sample

Key: 1) Secondary Ion Strength (Corresponding Units);  
2) Depth (Corresponding Units).

#### 4. Several Conclusions

1. After the ZQSn10-2-3 tin bronze sample undergoes double ( $Ag+N_i$ ) ion beam mixing, the area density of silver atoms in the surface layers is very high. This gives rise to the effects of high agent amount silver ion implantation. Moreover, the depth of distribution of silver atoms is far greater than its thickness, which demonstrates the fact that there has been produced mixing at the atomic level in relatively deep ranges between the silver atoms and the atoms of the basic body. This results in the formation of a new alloy, which causes an increase in surface microhardness and a raising of abrasion resistance. /290

2. After the implantation of  $N_i$  in silver-plated tin bronze specimen ZQSn10-2-3, there was a special effect produced in the surface layers, causing the surface coefficient of friction to go down and the abrasion resistance to be raised.

3. The ion implantation industrial process will not lower the surface luminosity of products.

Comrades ZENG Xian nan and HU Yun zhan of the Wen Zhou Ion Implantation Technology Research Center assisted us in ion implantation, and comrades such as TU Ming-hui of Bei Jing Center 621 assisted with the friction and abrasion tests. We wish to express our special thanks to them.

## REFERENCES

- [1] Dearnaley, G., Practical Applications of Ion Implantation. Presented at the Materials Research Society Annual Meeting, Cambridge, Mass. November (1979).
- [2] Cui Fu-Zhai, Li Heng-De and Zhang Xiao-Zhong, Modification of Tribological Characteristics of Metals After Nitrogen Implantation, Nuclear Instruments and Methods, 209/210(1983), 881.
- [3] YOU You mo, QIAO Yong, et al., Mechanical Engineering Materials, 2(1980), 30.
- [4] ZOU Shi chang, LIN Cheng du, TIAN Wei; WU Han Metallurgy, 3 (1981), 3.
- [5] ZHANG Guo liang, Zerbini, L., and others Mechanical Engineering Materials, 2 (1982), 35.
- [6] ZHANG Yong en, XIA Ri yuan, Physics, 2 (1983), 95.
- [7] Massoldi, P., ZHANG Guo liang, et. al, Mechanical Engineering Materials, 2 (1982), 41.
- [8] LIANG YA Tan, AN CHENG Yan xiong. Surface Analysis, Science Publishing House, (1980).
- [9] Chu Wei-Kan, Backscattering Spectrometry, (1978).
- [10] Zeigler, F., New Uses of Ion Accelerators, (1978).
- [11] WU Ying lun, Bei Jing Aviation Institute Journal, 4 (1981), 149.



YU Kun, XU Hong qing, SUN Chang yi, YAO Zhi ping, DAI Nan rong

(Beijing Institute of Aeronautical Materials)

#### ABSTRACT

The Con Clad Process of forming unidirectionally-reinforced boron/aluminium composite shapes is studied. B/Al tape is made of drum-winding boron-carbide-coated boron filament (140 micron in diameter) and plasma-spraying aluminium powder. The pack of plasma-sprayed B/Al tapes with mild steel sheet on both outer surfaces is bonded together by hot diffusion in air and consolidated into a steel-cladded unidirectional B/Al plate. Experiments demonstrate that good quality of bonding can be achieved by hot pressing in air. Therefore, the steel-cladded B/Al plate is bended along the lines parallel to the filaments in a forming die at room temperature and formed into a shape of desirable section configuration with bend radius equal to threefold B/Al sheet thickness. After forming, the steel is etched away with 40% nitric acid. Provided the suitable thickness of the cladding steel is chosen, B/Al sheet can be bended without cracking. This process is applicable to fabrication of B/Al shapes with various sections including angles, channels, zeos and hats.

## SUMMARY

This article attempts to research the technology of forming bent shapes out of unidirectional strengthened boron/aluminum composite materials. Using the atmospheric pressure, low heat pressure bonding method, one takes a two-sided shape of steel plate material pressure-formed into its configuration with a folded piece of boron-aluminum, then, at room temperature, one takes a boron-aluminum steel plate and bends it into the desired shape. Subsequently, one uses nitric acid to corrode away the steel plate. Using this method, it is possible to manufacture various types of boron/aluminum shaped configurations. This includes relatively complicated configurations such as hat-shaped materials. This lays a foundation for the practical use of boron/aluminum composite materials.

### 1. Forward

Boron/aluminum composite materials were developed early and are an industrial technology which is relatively familiar and well-known as an important type of filament strengthened, metal based composite material. It possesses a very high relative strength and specific modulus, and, in the realm of aviation and astronautics, it has important applied value. Outside China, and particularly in the United States, large amounts of test production and practical testing has been done (1,2) on boron/aluminum composite materials. These boron/aluminum composite materials, other than the plate materials which have small-scale applications, are mostly necessary for the manufacture of various types of spare parts, first among which are formed materials for different load surfaces. Because of this fact, the forming technology of boron/aluminum has even more important significance. We have already gone through the test production process involved in the manufacture of boron/aluminum form materials with dimensions specified as 1 meter in length and 80 centimeters in width. The form material load surfaces include various types of common configurations, such as, angles, troughs, Z forms and so on. It also includes the relatively complicated hat-shaped load

surfaces. These load surfaces can make full use or partial use of boron filaments running along the length of form materials providing unidirectional strengthening, satisfying differing design requirements.

## 2. The Fixing of the Test Production Industrial Process

The manufacture of boron/aluminum form materials can have many types of industrial process associated with it (2,3). We decided to make use of an atmospheric condition lowered heat pressure forming method to make flat aluminum/boron plates, then, we made use of clad plate bending techniques to bend and form them (2,4). The actual process was as follows. We took a 140 micron diameter boron filament with a pulled carbonized boron spray layer wound on a spindle wrapped in an aluminum sheet. We made use of plasma spray aluminum powder to add stability. We then cut out and took strips to be filament-aluminum sheets. After this, depending on the dimensions of the product, we carried out cutting and folding operations. We, then, made use of low carbon steel plates to cover two sides of the boron/aluminum folding layer, and added preparatory pressure to the mould. At 500-600 degrees Centigrade and 30-70 MPa pressure, we got low heat pressure diffusion bonding. After the heat and pressure were applied, the boron/aluminum plate wrapped in steel was cut to the required width. On the basis of the configuration of the formed material, we made use of different types of bending molds, and, at room temperature, bent the materials into shape. After this, we put the mold apparatus into 40% nitric acid to corrode off the wrapping steel plate, which, when done, revealed the formed material product. Its special characteristics were:

(1) The use of atmospheric pressure and heat was a relatively long /292 process for the pressure formation of parts. Moreover, it was difficult to realize the vacuum, temperature and pressure. At the same time, not using the vacuum was an advantage in that it raised the efficiency of production, lowered production costs, and made production easier.

(2) The use of the heat and pressure method of direct forming not

only involved the use of a very complicated mold, but, moreover, for the material of complicated load surfaces, in certain positions, because the pressure was applied in a parallel or nearly parallel manner (for example, the two side walls of the hat-shaped formed material), it was difficult to achieve adequate pressure, and it was not easy to obtain a tightly bonded material. The pressure production of flat plates posed no such problems; moreover, a set of heat pressure molds were also able to be used on the various types of materials.

(3) Due to the fact that the aluminum receives the restraining influence of the boron filaments, the plasticity of the boron and aluminum is very different. At room temperature, unidirectional strengthened boron/aluminum plate material is bent parallel to the filaments, and the bending radius must be at least ten times as large or more as the thickness of the plate, and this method is not suited to the making of small load surface materials. When heat bending is involved, although it is possible to obtain a bending radius which is three times the thickness of the plate (2); however, the mold must be heated, and this is difficult to control. When we make use of the cladding plate bending industrial technique, we avoid these problems, and, by the same token, are able to reach bending with a radius which is equal to three times the thickness of the plate.

In order to measure the mechanical characteristics of atmospheric pressure boron/aluminum plate materials, we made use of a plate material characteristic sample pressure manufactured using the same pressure and temperature ranges. We did not add the cladding steel plate to this characteristic sample. After the addition of heat, on a linear cutting tool, we cut a straight sided tensile strength sample. The length of this tensile strength sample was 200 cm and the width was 12.5 cm. The standard interval was 100 cm, and the thickness was approximately 1.5 cm. We made measurements of the tensile strength and modulus.

### 3. Test Results and Discussion

#### 1. Atmospheric Heat and Pressure Diffusion Bonding

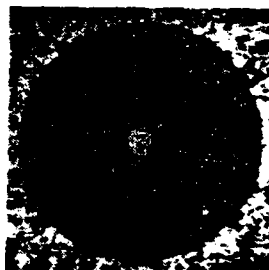
When one utilizes temperature and pressure, the aluminum sheet and aluminum powder diffusion bonding adheres very tightly to the boron filaments, coming together to form a very tightly organized composite plate material. Metallographic observations clearly show that there is no layering or gaps in the interior of boron/aluminum plate materials (Fig. 1(a)), and there are no gaps between filaments and the basic body (Fig. 1(b)). The boron/aluminum also bonds very well with the external layer of the cladding steel plate. This, therefore, guarantees that, in the process of bending and forming the boron/aluminum plate clad in steel, there is no layer separation in the interior of the boron/aluminum, and there is no detaching from the steel plate. The fracture surface of the plate material tensile sample is relatively neat and even, and there is no obvious pulling out of the filaments. From scanning electromicroscopy photographs of the fracture, one can see that, after the specimen sustains a tensile fracture, although there are a series of cracks produced in the body, there is, however, still no breaking of the boundary surface between the filaments and the aluminum (Fig. 2(a)). Fig. 2 (b) shows that, on the break surface of the filaments, there is still aluminum remaining. This is a decisive demonstration of the fact that atmospheric heat pressure diffusion bonding is successful.

Tensile strength test results on atmospheric heat pressure bonded boron/aluminum plate materials clearly show that the vertical tensile strength of filament plate material containing 36.7% (volume) was 610MPa, and that its elastic modulus is 165GPa. The modulus of atmospheric heat and pressure has no obvious influence on boron/aluminum plate material, and it shows the same results as those for vacuum heat and pressure products. However, the strength is obviously lower than the values obtained for the vacuum heat and pressure case.

## 2. Cladding Plate Bending



(a) 140x



(b) 500x

Fig.1 Micrographs of hot diffusion bonded B/Al sheet (plasma sprayed tapes hot pressed in air)

/293

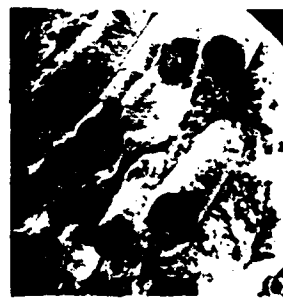
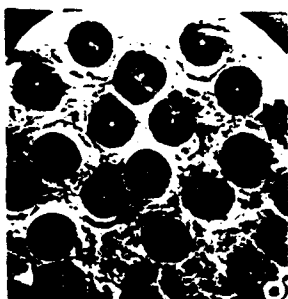


Fig.2 Scanning electron micrographs of tensile fracture surface

If the bonding of the cladding steel and the boron/aluminum is good, then it is only necessary to arrange them appropriately, the bending radius not smaller than three times the thickness of the boron/aluminum, and it is easily possible for the cladding steel and boron/aluminum, at room temperature, to make a 90 degree bend parallel to the filaments.

As far as the bending of angle shape material and trough shape materials are concerned, the molds involved are relatively simple, and the forming of the bends is not difficult. In the case of hat-shaped materials with a wall thickness of 1.5 cm, if one considers the low plasticity of the material and the peculiarities of the production of these items, it is best to produce them in specially designed molds. One first uses a ram to pressure the cladding steel and boron/aluminum plates into a concave mold, ramming out the top section and the two corner bends of the hat-shaped material. After this, one can cut open the two side walls, opening them up and, with even pressure, forming the hat-shaped stock.



Fig. 3 Some samples of cracking after bending



Fig. 4 Selectively reinforced hat section formed by bending



Fig. 5 Some samples of B/Al sections formed by bending

In situations in which the steel cladding plate fits improperly, when the bending is done, the hat-shaped material will produce cracks. The most serious situation is the one in which the outside layer of the steel cladding develops cracks, for this will lead to the development of cracks in the boron-aluminum as well (Fig. 3(a)). This is due to the fact that the steel clad boron/aluminum is too thick. The outside layer

steel plate changes and becomes excessively large. In many situations, the steel cladding plate does not develop cracks, but, after the steel plate is corroded away, it is discovered that the boron/aluminum bending sections have cracks (Fig. 3(b)). Sometimes, in the top section, between the sides, there is a vertical crack (Fig. 3(c)). When the thickness of the steel cladding plate is set up appropriately, it is not easy to produce cracking. In the case where all is properly set up, it is possible to bend to the necessary length the hat-shaped materials required. Photographs of their load surfaces can be seen in Fig. 4. From Fig. 4 one can see that, in the hat-shaped material, the top section uses boron filaments for strengthening, and the bottom section is aluminum.

/294

Fig. 5 shows various types of materials manufactured using industrial process employing clad bending. The load surfaces of these types of materials, depending on the requirements, can employ full or partial filament strengthening. The boron/aluminum partial filament volume ratio is approximately 30%.

#### 4. Conclusions

(1) As far as the manufacture of boron/aluminum materials is concerned, it is possible to first use heat and pressure to form flat plates, and then, after that, at room temperature, to carry out a two step bending process to do the forming. The use of this method is appropriate to the strengths involved, is simple and easy to control, and is easy to grasp.

(2) With the use of atmospheric pressure and heat, it is possible to take plasma and spray the boron/aluminum folding strips as well as the cladding plates, together, to form a single whole. As far as the heat and pressure are concerned, the temperature was 500-600 degrees Centigrade, and the pressure was 30-70MPa. The boron/aluminum plate material structure is extremely tight, and bonding with the cladding steel plate is excellent.



(3) In the use of cladding plate bending industrial techniques, it is possible to take unidirectional strengthened boron/aluminum plates containing 30% filament (volume), and, at room temperature, taking a radius three times the thickness of the plate, bend the stock 90 degrees in a direction parallel to the direction of the filaments and not cause cracks. This method can be used in the bending manufacture of various types of boron/aluminum material load surfaces.

Comrade JIN Cheng shan also participated in this work.

#### REFERENCES

- [1] Rubin, L., Applications of Metal-Matrix Composites, the Emerging Structural Materials, SAMPE, Vol. 24(1979), 1236~1249.
- [2] Renton, W. J., Hybrid and Select Metal-Matrix Composites, AIAA(1977), New York, 99~153.
- [3] Kreider, K. G., Metallic Matrix Composites, Academic Press(1974), New York and London, 422~428.
- [4] U. S. Patent, № 3793700.

AN APPROXIMATE ANALYSIS OF NET SECTION NORMAL STRESS  
IN A LAMINATE STRIP WITH A CIRCULAR HOLE

/295

ZHAO Jian hua and LIU Run tong

(University of Science and Technology of China)

ABSTRACT

This paper treats the analysis of a laminate strip with a circular hole. Useful approximate expressions (7), (12) and (14) for the distributions of net section normal stress and the stress concentration factor are derived by means of an approximate approach. The expressions are applied to the computation of laminate strips with a circular hole. The numerical computations performed are compared with the available test data and the finite element calculations. It is verified that the expressions are satisfactory.

## SUMMARY

This article makes use of approximation analysis methods to derive formulas for the approximate calculation of the normal stress distribution on surfaces with conflicting loads in laminate strips containing circular holes as well as for the factors causing stress concentrations on the edges of the holes. We made comparisons of the results of these formulas and the experiments described in related references as well as with the finite calculations made in this article and the results of our experiments. We found that the approximation formulas were adequate.

### 1. Approximate Analysis

If one considers the normal stress  $\sigma$ , for surfaces with conflicting loads on plate strips containing circular holes of finite width, as shown in Fig. 1, it is possible to express these values as

$$\frac{\sigma_i}{\sigma_0} = A + B\xi^{-1} + C\xi^{-2} \quad (1)$$

In this equation  $\xi = x/R$ ,  $A, B, C$  is a function of  $\lambda (=R/W)$ . It is possible, on the basis of data from reference (1), to use, at a minimum, a second order equation to make a precise calculation of these parameters for fixed values of  $\gamma$ , as shown in Fig. 1. For plates of non-limited width,  $A=1$ ,  $B=1/2$ ,  $C=3/2$ .

Table 1 Values of parameters  $A, B, C$  in Eq. (1) for some  $\lambda$

$\lambda$	0.125	0.200	0.250	0.300
$A$	1.00	0.99	0.93	0.81
$B$	0.62	0.71	0.98	1.45
$C$	1.44	1.44	1.33	1.09

If one takes the normal stresses for surfaces with conflicting loads on laminated strips containing holes, and one adds to the basic equation (1) the correction information shown as (2)

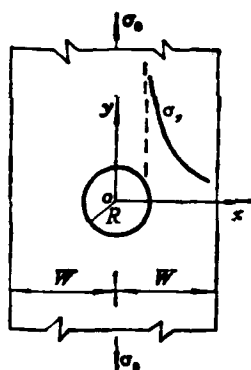
$$\frac{\sigma_y}{\sigma_0} = A + B\xi^{-2} + C\xi^{-4} + b_1\xi^{-4} + b_2\xi^{-6} \quad (2)$$

and one adopts the equilibrium conditions for the combined force resolves from the normal stresses on surfaces under conflicting loads, as shown below,

$$\int_R^w (A + B\xi^{-2} + C\xi^{-4}) dx = \int_R^w (A + B\xi^{-2} + C\xi^{-4} + b_1\xi^{-4} + b_2\xi^{-6}) dx$$

one arrives at

$$\int_R^w (b_1\xi^{-4} + b_2\xi^{-6}) dx = 0 \quad (3)$$



/296

Fig.1 Strip containing a circular hole

If we integrate equation (3), ignoring  $\lambda^0, \lambda^0$ , we then have

$$5b_1 + 3b_2 = 0 \quad (4)$$

Besides this, on the side of the hole  $x = R (\xi = 1)$

$$K_{II}^0 = A + B + C + b_1 + b_2 = K_{II}^0 + b_1 + b_2 \quad (5)$$

In this case,  $K_{II}^*$ ,  $K_{II}^*$  are, respectively, expressions of the factors causing stress concentrations on the edges of holes, for round holes in plate strips and in laminated plate strips containing holes. If we make use of equation (4) and equation (5) to solve for  $b_1$ ,  $b_2$ , we then can substitute in equation (2) and arrive at an approximate calculation formula, which is,

$$\frac{\sigma_y^*}{\sigma_0} = A + B\xi^{-1} + C\xi^{-4} - \frac{1}{2}(K_{II}^* - K_{II}^*)(3\xi^{-4} - 5\xi^{-8}) \quad (6)$$

We carry out a Taylor expansion of equation (6) in order to calculate the unknown  $K_{II}^*$ .

$$\frac{\sigma_y^*}{\sigma_0} - \frac{\sigma_y}{\sigma_0} = f(\xi, \lambda) = f(\xi, 0) + f'_1(\xi, 0)\lambda + \dots \quad (7)$$

From the mechanical meaning of the function  $f(\xi, \lambda)$ , it is possible to make the approximate hypothesis

$$f'_1(\xi, 0) = H\xi^{-1} \quad \text{and} \quad f(\xi, 0) = \frac{\sigma_{ym}^*}{\sigma_0} - \frac{\sigma_{ym}}{\sigma_0}$$

In this case,  $\sigma_{ym}^*$ ,  $\sigma_{ym}$ , are, respectively, the normal stresses for surfaces under conflicting loads on laminated plates containing holes of unlimited width and plates of a pandirectional nature.

If we take equation (7) and compare it to equation (2), we can deduce

$$\frac{\sigma_{ym}^*}{\sigma_0} - \frac{\sigma_{ym}}{\sigma_0} = -\frac{1}{2}(K_{II}^* - K_{II}^*)(3\xi^{-4} - 5\xi^{-8}) \quad (8)$$

In this case  $K_{II}^*$ ,  $K_{II}^*$  are, respectively, expressions for factors causing stress concentrations on the edges of holes on plates of a pandirectional nature and on laminated plates containing holes of unlimited width.

When  $\xi \rightarrow \frac{W}{R} = \lambda^{-1}$ , it is possible to recognize the approximate values

$$\frac{\sigma_y}{\sigma_0} - \frac{\sigma_y^*}{\sigma_0} = 0$$

From equation (7) and equation (8), one can arrive at

$$\frac{1}{2}(K_{T\infty}^* - K_{T0}^*)(3\lambda^4 - 5\lambda^2) = H\lambda^4$$

If we eliminate the quantity  $\lambda^4$ , one can resolve this into

$$H = \frac{3}{2}(K_{T\infty}^* - K_{T0}^*)$$

/297

Substituting in equation (7), and ignoring the high value quantity  $\lambda$ , one can arrive at

$$\frac{\sigma_i^*}{\sigma_0} - \frac{\sigma_i}{\sigma_0} = \frac{\sigma_{i\infty}^*}{\sigma_0} - \frac{\sigma_{i\infty}}{\sigma_0} + \frac{3}{2}(K_{T\infty}^* - K_{T0}^*)\xi^2\lambda \quad (9)$$

When  $\xi = 1$ ,  $K_{T\infty}^* = 3$  hours, equation (9) can be rewritten as

$$K_{Ti}^* = K_{T\infty}^* + K_{Ti}^* - 3 + 3(K_{T\infty}^* - 3)\lambda/2 \quad (10)$$

And, on the basis of reference (3)

$$K_{T\infty}^* = 1 + \sqrt{2(\sqrt{E_L/E_T} - \gamma_{LT}) + E_L/G_{LT}} \quad (11)$$

In this case  $E_L$ ,  $E_T$  respectively represent the modulus of elasticity of the material along the direction of tensile loading and in the perpendicular direction.  $G_{LT}$ ,  $\gamma_{LT}$  respectively represent the modulus of shearing and the relaxation ratio.

## 2. Comparison of Results

Reference (3) makes use of the Moire technique to determine  $(90^\circ/0^\circ/90^\circ/0^\circ)$ , which contain holes. In the case of seven-layer glass filament strengthened polyethylene laminated plates, the associated constants of elasticity are  $E_L = 19.2 \text{ GN/m}^2$ ,  $E_T = 22.0 \text{ GN/m}^2$ ,  $\gamma_{LT} = 0.07$ ,  $G_{LT} = 3.53 \text{ GN/m}^2$ . If we make use of equation (11) to calculate  $K_{T\infty}^* = 3.66$ , a comparison of the calculations using equation (10) and test results is entered in Table 2.

Table 2 Predicted values of Eq. (10) and measured values of  $k_{T,1}$  (3)

$\lambda$	0.125	0.188	0.250	0.400	备 注 (5)
$K_{T,1}$	3.06	3.13	3.25	3.74	按文献[1]中表15查出 4.60为文献[3]中曲线(4) 查得
$K_{T,1}$ 文献[3]的测定值(1)	3.80	3.90	4.05	4.60	
$K_{T,1}$ 本文公式(10)的 估算值(2)	3.84	3.98	4.16	4.80	
相对误差, % (3)	1.1	2.1	2.7	4.3	

Key: 1) Measured Value from Reference (3); 2) Calculated Value Using Equation (10) from this Article; 3) Relative Error; 4) The Finding of the Value 4.60 in Table 15 of Reference (1) is Based on a Check of the Curves in Reference (3); 5) Preparation Notes.

If we use finite variable methods to divide a symmetrical 1/4 portion of a plate containing a hole into 600 triangles undergoing a single variable constant stress (678 degrees of freedom), we first calculated the factors in the concentration of stresses ( $\lambda=0.05$ ) on laminated plates containing holes of non-limited width, and compared them to the results from equation (11). Subsequently, we calculated the factors in stress concentration on pandirectional plates containing holes, and compared them to the results from equation (1) when  $\xi=1$ . We demonstrated that, within the framework of limits that we chose, accuracies were all within 3%.

Results from the comparison of finite variable methods as applied to glass filament reinforced polyethylene composite plates containing holes, where  $\lambda=0.125$  and  $\lambda=0.250$ , and the calculated results from equation (6) are set out in Table 2.

We also made measurement of the normal stresses on surface subject to conflicting loads in polyresin laminated plates structurally strengthened with fiberglass with a latitudinal fiber bundle ratio of 4:1. The pasting and the applying of pressure in the manufacture of these materials was done by hand, and the hardening of the form was done at room temperature. The specific gravity of the fibers was 0.5.

The elasticity constants for different directional constants were  $E_L=23.1\text{GN/m}^2$ . Figure 4 shows a  $E_T=8.53\text{GN/m}^2$ ,  $\gamma_{LT}=0.19$ ,  $G_{LT}=3.13\text{GN/m}^2$  comparison of the calculated results from equation (6) and the elasticity constants for differing directional orientations and  $\sigma_x/\sigma_y$  as well as the calculated  $\epsilon_x$ ,  $\epsilon_y$ ,  $\epsilon_{xy}$ . From the specimens shown in Figure 3, which make use of  $1 \times 1\text{mm}^2$  then barrier electrical resistance strain wafers, we measured  $\epsilon_x$ ,  $\epsilon_y$  and  $\epsilon_{xy}$ .

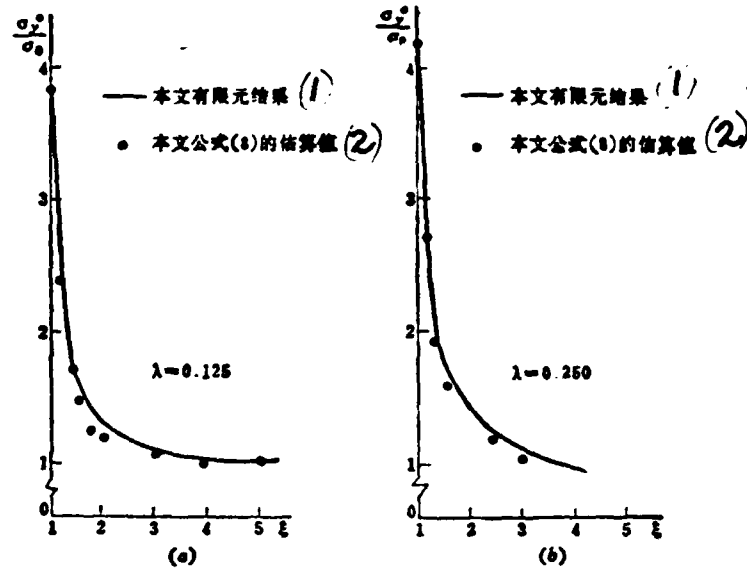


Fig.2 Comparison of present Eq. (6) and finite element Calculations

Key: 1) This Article's Finite Variable Results;  
2) The Calculated Results from Equation (8) in this Article.

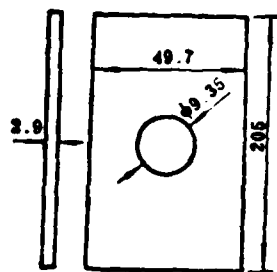


Fig 3 Strip specimen containing a hole

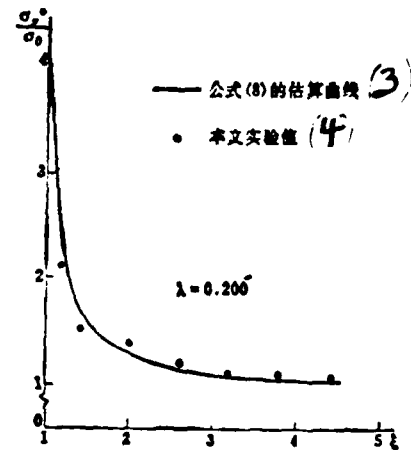


Fig.4 Comparisons of present Eq. (6) and strain measures

Key: 3) Curve of the Calculated Results from Equation (8);  
4) Experimental Values from this Article.



### 3. Results and Conclusions

1. When one makes use of equation (6) and equation (10) in order to calculate the factors in stress concentrations, and  $\lambda \leq 0.4$ , then, the relative error is within 5% (See Table 3 below). If one considers the case in which the error in the finite variable analysis is approximately 3%, it is possible to recognize that the accuracy of the results obtained from equation (10) is approximately 10%. Fig. 2 explains the fact that the normal stress distribution from equation (6), in the vast majority of areas, is lower than the results from finite variable calculations. These results correspond even better with the areas adjacent to the edges of holes.

2. When  $\lambda < 0.2$  hours, and we ignore the  $\lambda$  term in equation (10), then,

$$K_{T,1}^* = K_{T,2}^* + K_{T,1}^* - 3 \quad (12)$$

It is possible to obtain relatively good results such as those shown in Fig. 3; moreover, when  $\lambda > 0.2$ , then, it is better to make use of equation (10).

Table 3 Comparisons of Eq. (10) and Eq. (12) with finite element calculation

$\lambda$			0.125	0.188	0.250
$K_{T,1}^*$	有限元法计算值 (3)		3.66	3.84	4.19
	(4) 公式 (10)	估算值 (5)	3.84	3.98	4.16
		相对误差, % (5)	4.9	3.6	-0.7
	(4) 公式 (12)	估算值 (5)	3.72	3.79	—
		相对误差, % (6)	1.6	-1.3	—

Key: 3) Finite Element Calculation Value; 4) Equation; 5) Calculated Value; 6) Relative Error.

XI Chung and LI Huan qi participated in this testing work.

#### REFERENCES

- [1] SA Wen, r.H., "Stress Concentrations in the Vicinity of Holes", Scientific Publishing Company (1958), 108.
- [2] Konish, H J. et al, J. Composite Materials, 9, (1975), 157.
- [3] Daniel, I. M. et al, J. Composite Materials, 5, (1971), 250.

**DISTRIBUTION LIST**  
**DISTRIBUTION DIRECT TO RECIPIENT**

<u>ORGANIZATION</u>	<u>MICROFICHE</u>
A205 DMANTC	1
A210 DMAAC	1
B344 DIA/RTS-2C	1
C043 USAMIA	9
C500 TRADOC	1
C509 BALLISTIC RES LAB	1
C510 R&T LABS/AVRADCOM	1
C513 ARADCOM	1
C535 AVRADCOM/TSARCOM	1
C539 TRASANA	1
C591 FSTC	1
C619 NIA REDSTONE	4
D008 NISC	1
E053 HQ USAF/INET	1
E404 AEDC/DOF	1
E408 AFWL	1
E410 AD/IND	1
E429 SD/IND	1
P005 DOE/ISA/DOI	1
P050 CIA/OCR/ADD/SD	1
AFIT/LDE	2
FTD	1
CCN	
NIA/PHS	1
LLNL/Code L-389	1
NASA/NST-44	1
NSA/1213/TDL	1
ASD/FTD/1QIA	2
	1

DATE  
FILMED  
5-18